2018

Optical investigation of a hybrid system of plasmonic structures and semiconductor quantum dots

Matthew B. Seaton
University of South Carolina

Optical investigation of a hybrid system of plasmonic structures and semiconductor quantum dots

by

Matthew B. Seaton

Bachelor of Science
University of South Carolina 2009

Submitted in Partial Fulfillment of the Requirements

for the Degree of Doctor of Philosophy in

Physics

College of Arts and Sciences

University of South Carolina

2018

Accepted by:

Yanwen Wu, Professor

Thomas Crawford, Committee Member

Scott Crittenden, Committee Member

Andrew Greytak, Committee Member

Cheryl L Addy, Vice Provost and Dean of the Graduate School

Abstract

Next generation integrated nanophotonic devices must fabricate large numbers of nanoscaled light coupling structures onto a single wafer: emitters such as quantum dots, resonators such as nanocavities and plasmonic nanoparticles, photonic crystal and nano-plasmonic waveguides, among others. Before precision planning and engineering will be possible a thorough understanding of the interaction between these structures must be documented. We present in this work an investigation of the interaction between quantum dots and plasmonic structures in the weak coupling regime. We found that surface plasmon supporting silver structures placed about 100nm from InGaAs quantum dots enabled an all optical polarization dependent switching mechanism between different exciton charge states when exciting above the band gap energy of the encapsulating GaAs. Furthermore, when exciting below the band gap of GaAs, we found a reduction in the photoluminescence intensity due to the launching of surface plasmon polaritons (SPPs) on the silver surfaces.

Table of Contents

List of Figures

Chapter 1

Introduction

In this chapter, I will attempt to provide to the reader some motivation for interest in nanophotonics in general and especially the research topics presented in this work, as the potential for technological innovation is staggering. I will begin in the first section by talking about the current state of information processing technologies, and the limits imposed upon them by nature. This is a particularly relevant topic, as computers are entrenched in everyday life, and most people should be able to relate to the discussion. In the second section, we will discuss some of the proposed solutions to getting around these limits to push this kind of technology forward into a new age and bypass the imminent stagnation. Finally, I will attempt to provide further motivation for nanophotonics in general by talking about other applications of the technology. It is not limited to the information processing technologies discussed in the first two sections, and exciting exotic devices have been proposed and prototypes built. Hopefully after this chapter, you will have an interest in this field of research and an appreciation for the possibilities it offers for future technologies. At the end of the chapter, I have written a summary of the structure of this document.

1.1 Pushing the limits of current technology

The digital age followed the invention of the microcomputer. Information, in place of material products, has formed an entirely new class of commodity. The explosive growth rate of information processing and harvesting technologies has been powered by advancements in nanofabrication techniques. Currently these devices are powered

almost universally by silicon which is cheap, abundant, safe, and now has an entire manufacturing base established around it. This massive growth was described in 1965 by Intel co-founder Gordon Moore [1]. Moore's Law describes the exponential growth rate of transistor density in integrated circuits over time. As is typical with technological market innovations, the price of these devices has also fallen precipitously, especially when accounting for hedonic adjustments. This boom in computing power combined with the collapse in price made the power of digital computation ubiquitous, transforming society, for better and worse, in many respects.

Fast forward 53 years, and prognostications for the end of Moore's law abound [2, 3, 4, 5, 6, 7]. Some of the common reasons given are thermal noise, switching unreliability, untenable crosstalk at high frequencies, and increased manufacturing complexity. While silicon engineering firms are not giving up easily, it is becoming increasingly clear that the end is near. As many people are looking forward to the end of the era of traditional silicon devices, the search is on for new technologies to power the next generation of information processing devices.

The fundamental building block for electrical logic devices is the metal-oxide-semiconductor field effect transistor (MOSFET). This is formed by deposition of a metallic gate onto silicon, which has formed an oxide layer under controlled conditions. The oxide provides a potential barrier which limits electrical conductivity. However, the application of an electric potential can increase the conductivity. An external voltage, even a relatively small one, can control the flow of even a large current. Thus, there is a switching action and gain. From this many different kinds of devices can be constructed, such as integrated logic circuits and solid state amplifiers.

Thermal noise is a problem in MOS switches as it is competing against the oxide barrier energy, which must be large by comparison to maintain reliable switching and low current leakage. There are two headwinds against maintaining this relationship for proper device functionality. First, all else being equal, cramming more switches

into a single device raises the requirement of heat dissipation due to the basic laws of thermodynamics. One strategy to lower the heat production per transistor is to thin the oxide barrier, using smaller currents and weaker fields. However, this strategy has reached its limits [8]. For the standard CPU microprocessor, operating frequencies have also begun to level off as generated heat increases superlinearly with them. The CPU industry has adopted the paradigm of multiple integrated circuits (ICs) or cores in a single chip to scale around this problem, however this raises other issues as software must then be designed to run in parallel.

Crosstalk results from mutual inductance and capacitance in the conductive structures carrying the currents. Signals flow through an IC along conductive traces. One trace can feel the influence of the signal running through a nearby trace, disrupting the signal and potentially leading to data loss. For example, a current through one trace emanates a magnetic field which disrupts a current flowing nearby due to the Hall effect. This problem is exacerbated at higher frequencies also.

Engineering ingenuity has allowed Moore's law to march on, despite a number of technical challenges in the mass production of these devices. However there are signs this is slowing also. An increased manufacturing cost can help drive innovation in other competing technologies which were previously constrained by the economics of scale of the entrenched silicon MOS manufacturing infrastructure. For example, gallium arsenide (GaAs) has no native oxide, but does produce a Schottky barrier at the interface with certain metals. Metal-semiconductor field effect transistors (MESFETs) which use Schottky barriers on GaAs, instead of the oxide barriers used in silicon MOS devices, have lower power consumption and less noise while operating at higher frequencies than silicon MOSFETs. In the late 1980s, Seymour Cray switched the design of the CPU for his Cray 3 supercomputer from Si to GaAs for these reasons.

GaAs (and many other III-V semiconductors) has a number of advantages over silicon. It has a higher electron mobility, leading to low power, low noise, and high

switching speed operation. Unlike silicon, it is also a direct bandgap semiconductor, allowing efficient coupling into photonic modes for optoelectronics applications. However it also has some disadvantages as well. Gallium is more rare than gold, and expensive. Arsenic is also highly toxic, but GaN is also gaining a lot of research interest. Also the fabrication infrastructure is not as advanced as the silicon industry, but it is possible this may change as the limits of silicon based devices are reached.

While such devices may be faster, GaAs electronics devices will have their own limits as well, as these limits are inherent in the nature of electron transport, not the semiconductor material itself. This is a limit imposed by nature on the nonlinear behavior of electrons. GaAs technology though can do some things silicon cannot. It can provide a better pivot from electrons to photons as carriers of information, whose linear behavior dramatically increases the possibility for data throughput.

None of this should be construed as a claim that the traditional silicon processor will die or even that it will not continue to improve, but the rate of improvement is expected to decline. Further improvements may focus on aspects other than raw computational power such as: lower power consumption, lower price, a move towards application specific hardware rather than generalized computation, and better integration of independent devices. However, now that it is a mature technology with a rate of improvement that appears to be saturating, research should start to focus more earnestly on alternatives which may be able to surpass its limitations.

For the physicist the end of Moore's Law is intuitive, since quantum mechanics is assumed to be the ultimate law of nature at the fundamental level while CMOS transistors can be described as essentially classical devices. Either current is flowing or it isn't. There is no need for consideration of quantum effects like superposition or coherence. As the components of integrated circuits shrink to a certain point however, quantum effects can no longer be ignored and will eventually come to dominate. An electron in a single atom simply cannot be described classically.

1.2 Information processing devices for the new era

As this paradigm shift nears, a significant effort has been put into research efforts to find the ideal candidates for future information processing devices. A number of possible solutions have been put forth, each with their own pros and cons, and it is likely different devices will be produced for different use cases. In this section I will quickly review some of these device candidates and talk about some of their strengths and weaknesses.

1.2.1 Massive parallelization

The first response against the decline in the rate of improvement of information processing devices is decentralization of the computational process via massive parallelization. This is indeed one of the main approaches the industry has taken and has been successful to some extent, but this approach comes with several complications. Processors each access and modify their own memory stores, and these separate data structures must maintain a shared state when modified by one of the processing units. This complicates the structure of algorithms, sometimes significantly. While this can work well for running several separate tasks at once, or single tasks where the work can be easily split into smaller chunks and distributed, some algorithms are just not amenable to parallelization at all.

1.2.2 Superconducting computing

Superconductors provide a possibility for bypassing thermal limits to improved performance. By dropping the electrical resistance to essentially zero, heat generation is no longer a problem. Josephson junctions could take the place of CMOS switches, and very high frequency operation may be possible. However, the main drawback is that most of the superconductive materials discovered do not exhibit the phenomenon above cryogenic temperatures. The cost therefore quickly scales well past

a level of affordability for mass production. However, there is much research on high temperature superconducting materials, so this may be a viable path one day.

1.2.3 Quantum computing

One solution to the problem of nondeterministic, probabilistic switching is to simply embrace it. A quantum computer is an information processor which operates fully on the principles of quantum mechanics, itself a probabilistic theory, at least in the standard interpretation. Quantum bits, or qubits, are no longer digital binary constructs, 1s and 0s, but can exist in linear superposition of these on and off states like Schrödinger's cat.

These states exhibit the full $SU(2)$ symmetry, which opens up an entirely new world of computing. Logic gates which operate on classical bits also output classical bits, 1 or 0. Quantum gate operations can be represented by some unitary matrix operator. The states are now represented by a 2-dimensional basis of eigenstates, $|0\rangle$ and $|1\rangle$. An input of, e.g., $|1\rangle$ may output anything in the 2-D Hilbert space, perhaps neither $|0\rangle$ nor $|1\rangle$ but some combination like $\frac{1}{\sqrt{2}}(|0\rangle + |1\rangle)$.

It has been shown that such a computer, using quantum algorithms appropriate for the hardware, can reduce the complexity class of certain algorithms compared to their known classical counterparts. The prototypical example is the factorization of large prime numbers which takes exponential time on a classical computer, but was shown to take polynomial time with Shor's algorithm [9]. This has implications in fields such as cryptography, where some security algorithms rely on the infeasibility of factoring large prime numbers to secure data.

While quantum gates have been constructed, no quantum computer has yet performed a task faster than a classical computer. The main obstacle to overcome is the dephasing of the quantum system which results in irreversible data loss. Any algorithm therefore must run quickly on this timescale, which is often very short,

especially if the system is not operating at cryogenic temperatures.

The quantum computer is only fully realized with specialized quantum algorithms. In fact, it has been shown that the set of classical algorithms which can gain a speed increase with a quantum computer has measure zero [10]. Thus, while it may be useful as a specialized device which can perform a certain class of specialized functions very well, the quantum computer is unlikely to replace traditional computers until considerable computational theory has been developed to take advantage of the new hardware paradigm. Generalized quantum computing may therefore be a long way off into the future.

1.2.4 Photonics

Another information technology strategy, which is already widely employed, is photonics. Photonic devices use light rather than charge currents to transmit information. When not coupled to matter, the electromagnetic field is highly linear, up to the Schwinger limit which is enormous. This allows photons to be stacked on top of each other without interactions, enabling signal processing techniques like multiplexing which significantly increase the data throughput available in a waveguide compared to the signals running through interconnects on integrated circuits, which are essentially a series of current pulses. This can be done with modulated AC currents also which can then be converted back into a digital signal, but fiber optic cables tend to perform slightly better still. Large scale networks like the internet are built on such fiber optic networks.

It is not just data transmission however. Rates of data processing also have potential to be much higher than electronic devices. The lack of Joule heating when moving photons around allows extremely high frequencies at suitable temperatures. Furthermore, the linear nature of photon transmission avoids the crosstalk problem. To this end, the idea was proposed back in the 1970s to build all optical switch using

nonlinear optical components, in analog to the transistor [11]. Such devices have since been built [12, 13, 14, 15]. All optical logic gates [16, 17, 18] have also been constructed using photonic crystals.

Integration with existing electronic devices through optoelectronic conversion will hamper some of the possible performance gains. However the largest obstacle to an all optical computer is the large footprint of optical devices. While electronics are still in the process of approaching their size limit, traditional optics are limited by diffraction to a much larger size, a barrier which was hit long ago. Thus this strategy does not scale well with the trend toward smaller device footprints, and gains in component speed are offset by losses in component density.

1.2.5 Nanophotonics

This technique is a sort of hybridization of photonics and electronics which involves heavy light-matter interaction. Nanophotonics exploits the near field effect in systems of light coupled to charge carriers. Near field modes produces evanescent electromagnetic waves, i.e. they do not radiate into a far field pattern like traditional antennae which are meant to function at large distances. The non-radiative nature of this type of emission means that these fields are no longer transform limited, but can produce very large electromagnetic fields and field gradients in very small spaces. This then allows the possibility of using photons as information carriers, while maintaining the smaller footprint of electronic devices.

This of course comes with some sacrifices inherent in the light-matter coupling. As a result of this coupling, this mode of transmission is inherently lossy. However if this limitation can be overcome, perhaps through the implementation of some kind of gain, the possibility exists for integrated circuits with the operating performance at or near traditional photonic devices, but the footprint of traditional electronic devices. This thesis will focus on this type of device.

We have studied the phenomenon of the surface plasmon polariton (SPP), an evanescent electromagnetic wave occurring at the surface of a metal, strongly coupled to oscillations in its charge density, and confined to the interface between the metal and a dielectric. We fabricated structures to sustain such waves and placed them near self assembled quantum dot (QD) structures. The latter serve as single photon sources which may one day provide the gain necessary to overcome the lossy nature of SPP propagation. Before such exotic devices can be considered however, the interaction between the two systems must first be well understood. The goal of this research is to make some progress in that direction.

1.3 Nanophotonics and its applications

The first paper published demonstrating the effects of surface plasmons was at the beginning of the 20th century, all the way back in 1902. Robert wood observed an anomalous drop in the intensity of light scattered off of metal-backed diffraction gratings when illuminated at particular angles [19]. The phenomenon known as Wood's anomalies spurred theoretical interest which eventually led to the theory of surface plasmons. Although this has been known for some time, it wasn't until the advent of modern fabrication techniques allowed the deliberate control of such waves that new optical devices were designed to exploit them.

The potential for nanophotonic technology is by no means limited to computational or information processing devices either. Already prototypes using plasmonic resonators have demonstrated various other functionalities including: metamaterials [20, 21, 22, 23], nanoscaled sensors [24, 25, 26, 27], sub-diffraction optical components and imaging [28, 29, 30], improved solar cells and light harvesting [31, 32, 33, 34, 35, 36, 37, 38], biomedical applications and disease treatment [39, 40, 41, 42], This technology will be useful in these and any other applications where guiding and manipulation of light at the nanometer scale is desired.

While plasmonic structures have been effectively used for guiding light at this scale, quantum dots (QDs) provide excellent narrow band single photon sources at the nanoscale. The discreteness of the luminescent emission from QDs is a feature of the total confinement of their charge carriers, electrons, holes, and especially electron-hole pairs (excitons) which emit light when they combine with each other. Semiconductor QDs in particular are stable and robust and offer repeatable on demand generation of indistinguishable photons in the visible and near-infrared range [43, 44, 45, 46, 47]. It is also possible for coherent manipulations within the dot, making them candidates for implementation of qubits for quantum computing [48, 49, 50, 51, 52, 53, 54, 55]. They also offer an excellent tunability of their optical resonance during fabrication due to the quantum size effect. Decreasing the size of the dot decreases the separation of the wavefunctions of the electron and hole, increasing their binding energy and ultimately the energy, and therefore color, of the emitted photon.

The QDs used in this research self-assemble in the core-shell structure, small nanocrystals of a smaller bandgap material are fully encapsulated by a material with a larger bandgap. However, such dots, once fabricated and thus encapsulated inside a wafer, offer little potential for altering the potential landscape thereafter. The degree of active control available to the end user is thus somewhat limited. One idea around this is to use a different strategy to define the QD. Gate-defined dots can be formed on from single material wafers using external electrical contacts whose fields form electrostatic traps that confine charge carriers [56, 57, 58]. Such gate-defined QDs offer additional flexibility but are still limited by the speed of the electronics and more complex fabrication, among other issues.

A possibility for additional control over our self-assembled QDs is to use external electric or magnetic fields to alter the internal dynamics of the dot. The samples studied in this thesis are fabricated in the Schottky diode structure, providing an electrical gate for this purpose. The dots are not defined by the gate, but band

bending effects can alter their luminescent emission. Again though, under active control by this method, device performance would be ultimately constrained by the electronic switching speed.

It is also possible to alter the behavior of the photoluminescence of QDs with the introduction of nearby plasmonic structures. The SPP modes supported on such structures provide large local electric fields and electric field gradients, arising entirely from optical excitation. Moreover the change in the local optical density of states can change the exciton relaxation pathways of the QDs, leading to some control over QD photoluminescence: an enhanced rate of radiative exciton recombination [59, 60, 61, 62], a suppression of radiative recombination [62, 63, 64], and alteration of the spatial emission profile [65, 66, 67]. The interaction between these two systems must be well understood before engineering of complex integrated devices will be possible.

It would be highly desirable to obtain a method for an entirely optical tunability of QD emission. We have fabricated a sample implanting plasmonic structures into a semiconductor QD wafer to get a better understanding of their interaction. The work presented in this thesis demonstrates an extra mode of control the SPPs can exert over QD emission which can switch the emission state of the dot and is all optical. This is achieved by polarization dependent launching of SPPs in the neighborhood of the dots, under excitation by light with energy above the band gap of the encapsulating GaAs. Such a method may allow ultrafast optical switching of QD emission. We have also discovered a polarization dependent suppression of QD emission under excitation by light with energy below the GaAs band gap. This effect is also attributed to the local launching of SPP waves. Although we have not fully determined its mechanism, a proposed explanation is put forth.

1.4 Thesis outline

This chapter hopefully succeeded in motivating the reader for an interest in the research performed and presented in this thesis. It began with a brief overview of the current state of information processing and some of the problems it is facing moving forward into the future. We also discussed some possible alternative directions, with a special emphasis on nanophotonics and its applications.

The next chapter contains a review of the theoretical background necessary to understand the research presented in the rest of the paper. It begins with a brief review of classical electrodynamics, followed by some of the models appropriate to understand the behavior of electrons in solid materials. We then discuss the solutions to a plane wave scattering at a planar interface. This problem is then modified and generalized to the case of a surface guided wave at a planar interface. This wave is called a surface plasmon polariton (SPP). Then we discuss some of the properties and requirements for such a wave to occur. After this is a brief overview of the theory of crystalline materials, then a review of the topics of quantum confinement and excitons, with an emphasis on the quantum dot (QD) structure. The SPP and QD are the essential topics of study in this work.

Chapter 3 describes the steps I took to set up the experiments. It begins with a detailed description of the process of fabricating and implanting the SPP supporting structures into the QD substrate and completing the Schottky diode structure. Then I describe the setup and layout of the confocal micro photoluminescence (PL) experiment and how the data were collected.

Chapter 4 details the results of the excitation of the InGaAs dots when the energy of the incident photons is above the band gap of the encapsulating GaAs. We discuss the difference in the PL signal that is caused by the presence of the silver structures, especially the polarization difference arising from the launching of SPP waves, which only occur in one particular polarization. PL data were collected as a function of

applied bias and incident power, and we discovered a switching mechanism between different exciton charge states which is all optical. This effect is due to the SPP induced screening caused by an excess of carriers injected into the GaAs around the dots.

Chapter 5 discussed the below band excitation, when there is no such injection of carriers. The results show again a clear polarization dependence on the PL spectrum when exciting on the plasmonic structures. We attribute this difference again to the launching of SPPs along the silver structures and discuss a possible mechanism. More work needs to be done in the future to verify this picture.

Chapter 6 gives a brief wrap up, summarizing the results in this thesis, and laying a roadmap for future studies along this direction. At the very end is a brief discussion of the future of nanophotonics.

Chapter 2

Background theory

This chapter starts with a brief review of the foundations of classical electrodynamics. We will pay special attention to a particular solution to Maxwell's equations describing a 2-dimensional longitudinal wave at the interface between two materials which satisfies certain conditions. This wave is known as a surface plasmon polariton (SPP).

The second part of this chapter concerns the theory and characterization of semiconductor quantum dots. After some background theory for crystal materials, we will discuss the specific materials and structures studied in this work. The research presented here will focus on the interaction between these two systems.

For the purposes of this thesis it is appropriate to use the semi-classical approximation, wherein the electromagnetic fields are treated as classical fields interacting with the quantized system of charge carriers. Quantization of the electromagnetic field is a complex subject and will not be discussed in this work, as it is beyond the scope necessary to understand this research. The permeability and permittivity, μ and ϵ respectively, of materials will always be taken to be dimensionless. Therefore they will always be relative to the vacuum permeability and permittivity, μ_0 and ϵ_0. Furthermore the systems of interest will exhibit negligible effects from magnetic coupling. Thus the permeability will always be assumed to be unity, $\mu = 1$. Also, all fields will always be assumed to be well-behaved and amenable to Fourier analysis, under the prescription $\frac{\partial}{\partial t} \to -i\omega$ and $\nabla \to i\vec{k}$. All equations are in S.I. units.

Maxwell's equations (2.1) together with the Lorentz force law (2.2), when supplied with appropriate boundary conditions, are sufficient to describe the whole of classical electrodynamics, i.e. all known electromagnetic phenomena to the extent that effects due to the quantum nature of reality can be ignored.

$$\begin{aligned} \nabla \cdot \vec{E} &= \frac{\rho}{\epsilon_0} & \nabla \times \vec{E} &= -\frac{\partial \vec{B}}{\partial t} \\ \nabla \cdot \vec{B} &= 0 & \nabla \times \vec{B} &= \mu_0(\epsilon_0 \frac{\partial \vec{E}}{\partial t} + \vec{J}) \end{aligned} \tag{2.1}$$

Here $\vec{E}$ and $\vec{B}$ are the electric field and magnetic induction (sometimes called magnetic field), ϵ_0 and μ_0 are the electric permittivity and the magnetic permeability which reflect the associated electric and magnetic polarizability of the vacuum, respectively. J and ρ are the current density and charge density respectively.

The $\vec{E}$ and $\vec{B}$ fields couple to a charged particle's total charge q and velocity $\vec{v}$ to produce a force on the particle according to (2.2).

$$\vec{F} = q(\vec{E} + \vec{v} \times \vec{B}) \tag{2.2}$$

When considering fields inside matter it is important to note that since atoms comprise charged particles. Equation (2.2) implies that the applied fields induce a response in the material, and this will manifest in ρ and J, altering the sources of (2.1) once again. In other words, the fields produce a response on charge carriers, currents or polarizations for example, which then produces new fields again. Thus we are led to coupled, non-linear partial differential equations which must be solved self-consistently. This is not trivial to do except for a few special cases.

To simplify analysis of the solutions inside matter it is convenient to introduce auxiliary fields to isolate from $\vec{E}$ and $\vec{B}$ two separate parts, fields external to the system of interest and polarization fields due to the response of the charges in the material comprising the system of interest. Maxwell's Equations can then be rewritten

into a form where the sources can be split into two parts, sometimes called free and bound, or internal and external. In these equations only the free charges and currents couple to the new fields, simplifying the analysis as polarization related sources can be ignored. Although this does not come without a cost. The total solution to the problem now involves four vector fields instead of two.

$$\begin{aligned} \nabla \cdot \vec{D} &= \rho_f & \nabla \times \vec{E} &= -\frac{\partial \vec{B}}{\partial t} \\ \nabla \cdot \vec{B} &= 0 & \nabla \times \vec{H} &= \frac{\partial \vec{D}}{\partial t} + \vec{J}_f \end{aligned} \tag{2.3}$$

The same letters, $\vec{E}$ and $\vec{B}$, are redefined to mean only the externally applied fields, and the fields $\vec{D}$ and $\vec{H}$, called displacement field and magnetizing field ($\vec{H}$ is also sometimes called magnetic field) are defined to include both the external fields and the polarization fields induced by the material. These fields are sometimes called macroscopic fields, since they involve averaging over regions small enough to allow derivatives that describe continuous fields, but still large on the atomic scale, so they can ignore the discrete nature of particles. Equations (2.3) are also called the macroscopic Maxwell's equations. The displacement and magnetizing fields are *defined* as follows,

$$\vec{D}(\vec{r},t) = \epsilon_0 \vec{E}(\vec{r},t) + \vec{P}(\vec{r},t) \qquad \vec{H}(\vec{r},t) = \frac{\vec{B}(\vec{r},t)}{\mu_0} + \vec{M}(\vec{r},t) \tag{2.4}$$

where $\vec{P}(\vec{r},t)$ and $\vec{M}(\vec{r},t)$ are the polarization fields due to the response of charges bound inside the material. The displacement and magnetizing fields take into account the screening of the vacuum fields due to the response of the charges in the material and more accurately reflect the average net force on a charge carrier inside the material, which is modified by its interactions with the extra fields present. However, because calculation of the macroscopic fields is difficult, when writing a semi-classical equation of motion, it is more common to keep the external $\vec{E}$ and $\vec{B}$ fields in (2.2) and employ a mass renormalization technique instead, see section 2.3.2.

While all of the equations presented thus far have a universal domain of applicability, to the extent that quantum effects can be ignored at least, practical exact calculations are only possible for very simple systems and geometries. Most systems of interest in modern scientific research involve materials of macroscopic size and nontrivial geometry, so it is beneficial to use equation (2.3), but at the same time $\vec{P}$ and $\vec{M}$ are too complex to enable useful calculations without making some approximations. The first such approximations are typically an expansion of the auxiliary fields in terms of the external fields, the first term of which is the *linear* displacement field and magnetizing field for electromagnetic fields inside matter. This is done by absorbing the polarization response, which may be out of phase with the applied field, into complex permittivity and permeability functions describing the material. Understanding the linear optical properties of matter is then reduced to calculation or measurement of these two functions. The calculation of polarization as a response to applied electric fields is nontrivial since the response is not instantaneous. In general it involves a convolution over the past light cone of the polarizability with the external fields. However the convolution theorem tells us that in the frequency domain these relations become simple products and we can write for the linear response of materials,

$$\vec{D}(\omega,\vec{k}) = \epsilon_0\epsilon(\omega,\vec{k})\vec{E}(\omega,\vec{k}) \qquad \vec{H}(\omega,\vec{k}) = \frac{\vec{B}(\omega,\vec{k})}{\mu_0\mu(\omega,\vec{k})} \tag{2.5}$$

In general the permittivity ϵ and permeability μ are complex valued second rank tensors describing material anisotropy, functions of frequency, temperature, and other variables, and may have nonlinear terms which couple to higher orders of the applied fields. These nonlinear terms are typically small and involve the production of new frequencies given by addition and subtraction of combinations of the other frequency components present. For example, a commonly exploited second order effect is the frequency doubling effect known as second harmonic generation (SHG). For most materials these nonlinear contributions are small, but can be responsible for interesting

optical effects. These terms can be measured through clever experimental design, which allows for the isolation of particular nonlinear terms of interest.

Taking the curl of the curl equations in (2.1) in vacuum, a region without charges or currents classically speaking, and substituting the divergence equations leads to the wave equations for the fields propagating at a constant speed $c = (\epsilon_0\mu_0)^{-\frac{1}{2}}$ equal to the speed of light.

$$\begin{aligned} \nabla^2\vec{E} &= \frac{1}{c^2}\frac{\partial^2\vec{E}}{\partial t^2} \\ \nabla^2\vec{B} &= \frac{1}{c^2}\frac{\partial^2\vec{B}}{\partial t^2} \end{aligned} \tag{2.6}$$

This discovery led Maxwell to conclude that light is in fact an electromagnetic wave. These wave equations however exhibit a constant phase velocity if the permittivity and permeability of vacuum are taken to be constant. No consideration is made as to the frame of reference, even those moving with respect ot each other. Originally, theorists proposed a luminiferous ether, a medium for the propagation of light, which imbued the permittivity and permeability with an anisotropy based on the motion of the ether relative to the observer. When experiments failed to demonstrate the existence of such an ether, the theory of relativity eventually emerged.

The propagation of electromagnetic waves is altered by the optical response of any media present. Going into the frequency domain with the substitution $\frac{\partial}{\partial t} \rightarrow -i\omega$, leads to the Helmholtz form of the wave equations.

$$\nabla \times \nabla \times \vec{E}(\vec{r},\omega) = \epsilon(\vec{r},\omega)\frac{\omega^2}{c^2}\vec{E}(\vec{r},\omega) \tag{2.7}$$

In the following, we will make use of the vector identity, $\nabla\times(\nabla\times\vec{A}) = \nabla(\nabla\cdot\vec{A}) - \nabla^2\vec{A}$. Consider an environment without free sources, $\nabla\cdot\vec{D} = \nabla\cdot(\epsilon\vec{E}) = 0$. This implies that $\nabla\cdot\vec{E} = \frac{1}{\epsilon}\vec{E}\cdot\nabla\epsilon$. To the extent that $\frac{\nabla\epsilon}{\epsilon}$ is small compared to the wavelength of the light involved, this term can be ignored and the Helmholtz form reduces to the more familiar

$$
\begin{aligned}
(\nabla^2 + \vec{k}^2)\vec{E} &= 0 \\
\text{where } k^2 &= \epsilon\frac{\omega^2}{c^2}
\end{aligned}
\tag{2.8}
$$

This leads to the familiar result relating the index of refraction to the phase velocity of electromagnetic waves,

$$
n = \sqrt{\epsilon} = ck/\omega = c/v_p \tag{2.9}
$$

One of the main benefits of using the macroscopic Maxwell's equations (2.3) is that they imply a set of constraints on the four fields $\vec{E}, \vec{D}, \vec{B}$, and $\vec{H}$ at the interface between two materials with different ϵ and μ.

$$
\begin{aligned}
\Delta\vec{E}_{\parallel} &= 0 & \Delta\vec{D}_{\perp} &= \rho_{f,s} \\
\Delta\vec{B}_{\perp} &= 0 & \Delta\vec{H}_{\parallel} &= J_{f,s}
\end{aligned}
\tag{2.10}
$$

The component of $\vec{E}$ parallel to the interface and the component of $\vec{B}$ along the direction normal to the interface do not change across the interface between the materials. Furthermore the normal component of $\vec{D}$ and the parallel component of $\vec{H}$ change by the amount of unbound charge density and unbound current density, respectively, at the surface of the interface. This greatly simplifies the solutions of these fields.

2.1.1 Lorentz oscillator model

The optical response of real materials can be approximated by means of a heuristic differential equation, constructed with some convenient and reasonable approximations. Consider a classical scalar field representing an electron cloud's charge density ρ with total charge $-e$ surrounding a nucleus and bound by its potential energy. A bound electron responds to perturbations in the background electric fields by displacing its charge density ρ from its equilibrium configuration, i.e. it's form when there is no external field, by some average amount $\langle\vec{r}\rangle$ around the atom's location, $\vec{r_0}$. To first order, the electron is attracted back in the direction of the nucleus by a

spring-like force proportional to $\langle\vec{r}\rangle$ and to the square of the resonant frequency of the oscillator, ω_0. This leads to a differential equation for the atom's electric dipole moment, defined as $\vec{p} = -e\langle\vec{r}\rangle$.

$$m\frac{d^2\langle\vec{r}\rangle}{dt^2} + m\gamma\frac{d\langle\vec{r}\rangle}{dt} + m\omega_0^2\langle\vec{r}\rangle = -e\vec{E}(\vec{r},t) \tag{2.11}$$

where γ is a phenomenological damping constant. In general $\vec{E}$ will depend on position (or wavelength) as well as time (or frequency). However if $\langle\vec{r}\rangle$ is much smaller than the wavelength of the light involved this spatial dependence can be safely ignored. This is called the discrete dipole approximation, as the atoms are considered to be point dipoles affected by a stationary oscillating electromagnetic field. The solution can be easily seen by going into the frequency domain using the frequency convention $\partial_t \to -i\omega$. The polarization field, or dipole moment density, is then

$$\vec{P}(\omega) = -ne\langle\vec{r}(\omega)\rangle = \frac{ne^2\vec{E}(\vec{r}_0,\omega)/m}{\omega_0^2 - \omega^2 - i\omega\gamma} \tag{2.12}$$

where n is the density of the oscillating electrons.

The spectral lineshape of the dipole moment is a Lorentzian of a complex variable. Therefore the polarization response is out of phase with the applied field. Comparing (2.12) with (2.4) suggests a model for terms in the dielectric function describing electrons bound to atoms or molecules,

$$\epsilon(\omega) = 1 + \sum_k \frac{f_k}{\omega_k^2 - \omega^2 - i\gamma_k\omega} \tag{2.13}$$

where we sum together the contributions from some number of individual electron resonances. The f_k are experimentally determined weights for the resonance at ω_k. This model is completely linear and ignores contributions from higher order effects such as electron-electron interactions, spin-orbit coupling, etc., but works well as a first approximation.

2.1.2 Drude electron gas model

Metals however exhibit effects which cannot be explained by the presence of only bound electrons, e.g. large electrical conductivities. One of the earliest successful attempts to explain these properties was the Drude model. In this model the structure of the metal is imagined to be a set of inert positively charged ions in fixed positions within a gas of nearly free electrons which collide with the ions with a constant probability density over time, $1/\tau$. These collisions scatter the electrons in random directions isotropically resulting in no average momentum just after impact. Although there is an average squared momentum, and therefore kinetic energy, dependent on the temperature of the gas. Between collisions the electrons are assumed to obey the Lorentz force law (2.2), which only contains the externally applied fields. In order to account for interactions with the internal material polarization fields in this approach, the masses must be renormalized to an effective mass, m^*. The electron is now said to be *dressed*. The differential equation describing the average dynamics of the electrons is

$$\frac{d\vec{p}}{dt} + \frac{\vec{p}}{\tau} = -e\vec{E} \tag{2.14}$$

The solution can be easily seen by going into the frequency domain using the frequency convention $\partial_t \to -i\omega$.

$$\vec{p}(\omega) = \frac{-e\vec{E}(\omega)}{1/\tau - i\omega} \tag{2.15}$$

On average the electrons travel for a time τ before colliding, during which time they will have built up an average momentum of $-e\vec{E}\tau$ in the case of an externally applied field $\vec{E}$. This leads to a similar equation for polarization as in the Lorentz model without a restoring force term, ω_0.

$$\vec{P}(\omega) = -ne\vec{r}(\omega) = \frac{-ne^2\vec{E}(\omega)}{\omega(\omega - i/\tau)} \tag{2.16}$$

In other words the valence electrons in metals form a quasi-free plasma. The dipole approximation will be valid again to the extent that the mean free path of the electrons

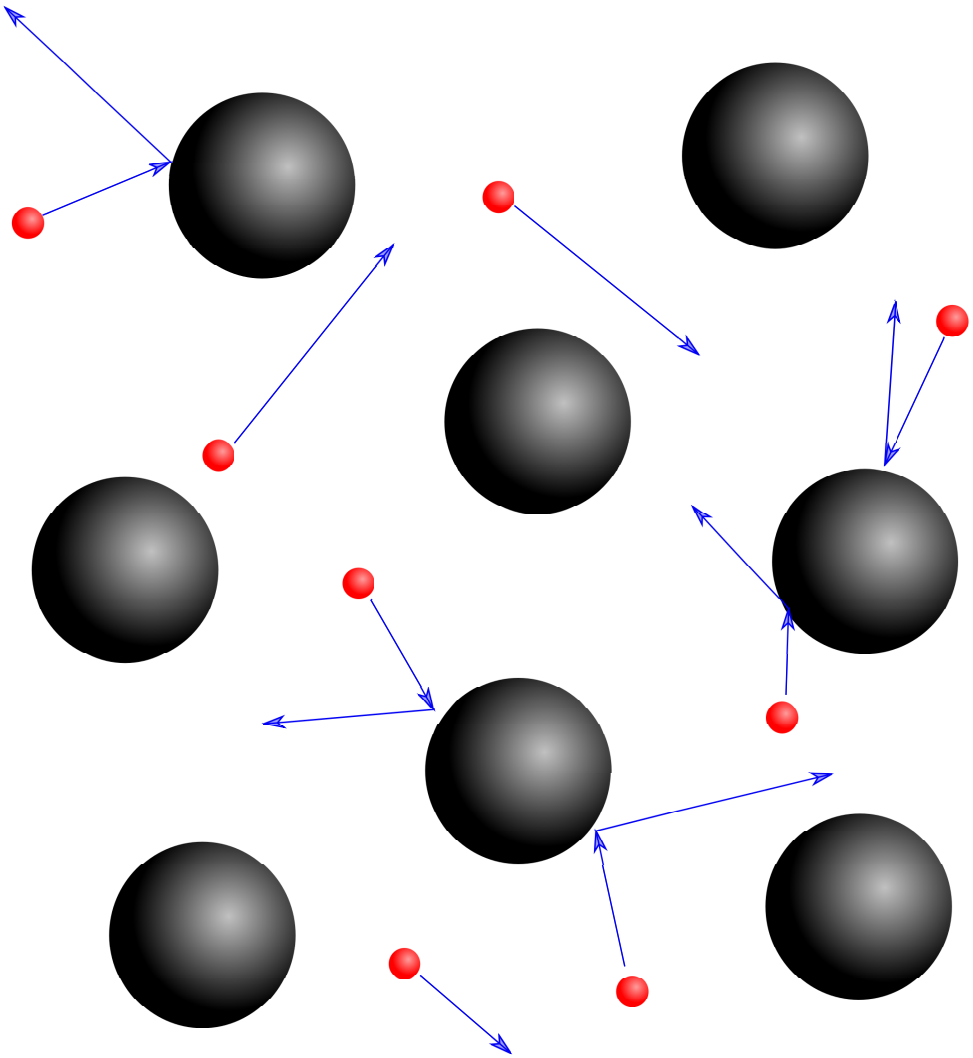

Figure 2.1 The Drude metallic electron plasma is imagined to be a set of quasi free mobile electrons colliding randomly with fixed inert ions.

is small compared to the optical wavelength. The dielectric function can be obtained by combining (2.4) and (2.5).

$$\epsilon = 1 + \frac{\vec{P}}{\epsilon_0 \vec{E}} \tag{2.17}$$

Combining this with (2.16) yields the contribution to ϵ arising from the Drude plasma.

$$\epsilon(\omega) = 1 - \frac{{\omega_p}^2}{\omega(\omega - i/\tau)} \tag{2.18}$$

where ω_p is called the plasma frequency and is given by $\omega_p = ne^2/m^*\epsilon_0$, which for many metals is much larger than τ^{-1}. To the extent that this damping can be ignored, (2.18) simplifies to

$$\epsilon(\omega) = 1 - \frac{{\omega_p}^2}{\omega^2} \tag{2.19}$$

Thus, although the electrons are not bound to individual atoms, the Drude plasma still carries a natural dipole resonance, producing a wave of oscillating charge density at the plasma frequency due the plasma's self interaction, i.e. electron-electron interactions and interactions with the background lattice of ions. This resonance corresponds to zeroes of the dielectric function. It can be seen from (2.7) by making the substitution $\nabla \to i\vec{k}$, that $|\vec{k}|^2\vec{E} + \vec{k}(\vec{k} \cdot \vec{E}) = 0$. The plasma resonance is therefore a longitudinal wave, as expected for an oscillation of charge density since electric field lines point from positive to negative charges. This type of plasma oscillation is called bulk plasmon since its effect is to induce a polarization across a 3-dimensional material. This is in contrast to a surface plasmon which only occurs at the interface of a metal. This is a special type of wave and will be discussed in section 2.2.2.

The characteristic reflectivity of metals is due to their negative permittivity at frequencies lower than ω_p. In this regime the fields are driven out of the metals as charges on the surface oscillate in response to the external field, attenuating any response inside the metal and ultimately emitting their own fields back outward. This is the cause of specular reflection. The plasma frequency itself is typically in the ultraviolet spectrum, so lower frequency visible light tends to be reflected, although

individual resonances can color the reflected light. Above ω_p the dielectric function becomes positive and metals behave like dielectrics. At very large frequencies it approaches unity, as the electrons do not respond to the applied fields fast enough to screen them out. This is sometimes called the ultraviolet transparency of metals, although band transitions still play an important role in the absorption of photons. We will discuss band theory in section 2.3.1.

2.2 Theory of surface plasmon polaritons

In this section I will derive and discuss a particular solution to Maxwell's equations known as the surface plasmon polariton, a name reflecting the strong coupling between light and the polarization response induced in the electron plasma at a metal's surface. We arrive at this solution by generalizing the problem of scattering of light off of the planar interface between two different materials. This is followed by a discussion of the possibility of wave guiding at the interface, leading ultimately to the derivation of the SPP. The section is concluded with a discussion of some of the properties of such a wave, its dispersion relation compared to bulk plasmons, and how these modes can be coupled to asymptotic free space modes.

2.2.1 Scattering of light at a plane interface

Consider a monochromatic plane wave travelling in the x-y plane toward the interface between two materials separated by the plane $y = 0$ as depicted in figure 2.2. The materials are described by two dielectric functions ϵ_1 and ϵ_2 with wavenumbers k_1 and k_2 in the two materials, according to the relation $k = \frac{\omega\sqrt{\epsilon}}{c}$. The incident wave is moving towards the interface from the upper half-plane. A convenient basis for the vector space of possible polarizations of the incident wave includes two basis vectors, s-polarized transverse electric fields (TE) fields and p-polarized transverse magnetic fields (TM). This can be described with just the transverse field component, from

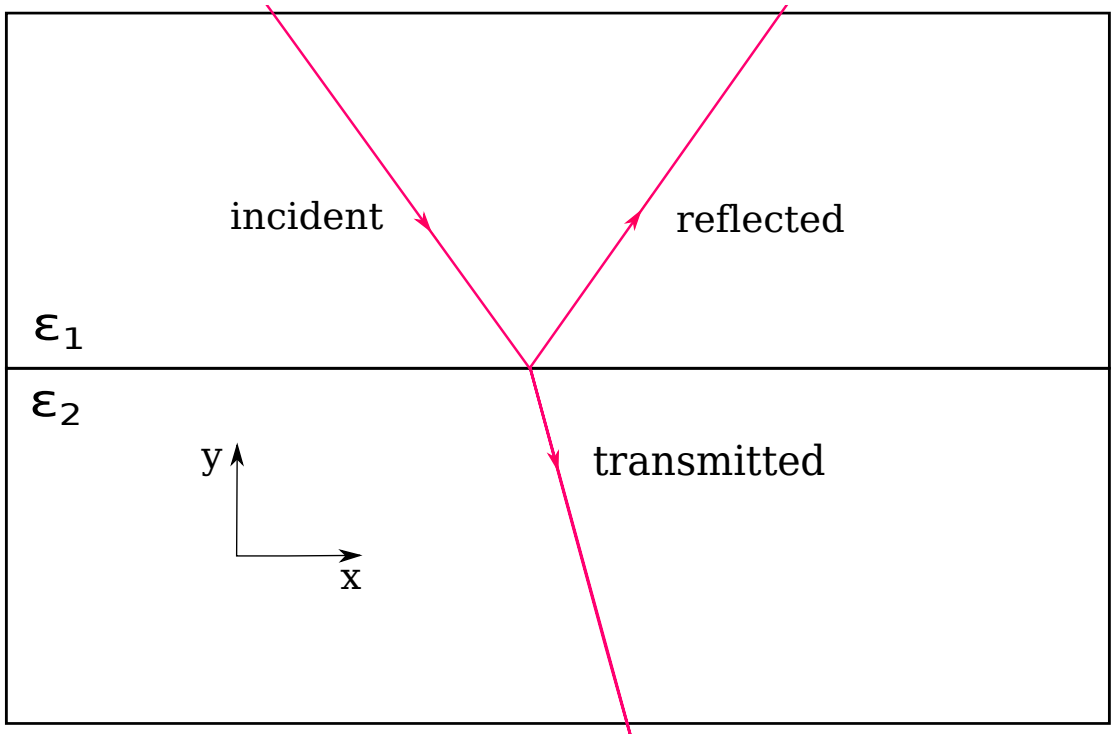

Figure 2.2 A plane wave scatters at the interface between two different dielectric media described by two different dielectric constants, ϵ_1 and ϵ_2. Incident light strikes the surface between the media, part of which is reflected back upward, and part of which is transmitted into the material. The wave vectors of the different components are shown by the red rays.

which the other components of the fields can be derived if the angle of incidence is known.

$$\vec{F_i}(x,y) = F_i \hat{z} e^{i\vec{k}\cdot\vec{r}} = F_i \hat{z} e^{ik(\alpha x - \beta y)} \tag{2.20}$$

where F_i is the amplitude of whichever incident field is transverse to the plane for the particular polarization under consideration, E_z for TE waves and B_z for TM. If n_1 is real, then α and β are simply the cosines from the projections of $\vec{k}$ onto the coordinate axes, x and y. The signs have been chosen so that they will be positive. This implies that $\alpha^2 + \beta^2 = 1$, which also follows from the Helmholtz equation 2.8. For a perfectly flat interface, the reflected field will obey the law of specular reflection.

$$\vec{F_r}(x,y) = F_r \hat{z} e^{ik(\alpha x + \beta y)} = r F_i \hat{z} e^{ik(\alpha x + \beta y)} \tag{2.21}$$

Note the change in sign in front of β. For the transmitted field, the y-component of the field changes with the change in the refractive index $n = \sqrt{\epsilon}$ of the materials, while the x-component stays constant. This behavior is encoded in Snell's law. Any change in the wavevector as the wave passes into a material with a different index of refraction only occurs in the direction normal to the interface (in this case, y), while the parallel component (x) stays constant. It follows as a result of (2.10).

$$\begin{aligned} \vec{F_t}(x,y) = F_t \hat{z} e^{ik(\alpha x - \gamma y)} &= t F_i \hat{z} e^{ik(\alpha x - \gamma y)} \\ \gamma &= \sqrt{\left(\frac{n_2}{n_1}\right)^2 - \alpha^2} \end{aligned} \tag{2.22}$$

Note that there is an ambiguity in the definition of γ. To avoid nonphysical behavior, the signs of the real and imaginary parts must be chosen to satisfy the Sommerfeld radiation condition so that waves either propagate or attenuate in any direction away from the interface. The interface boundary conditions (2.10) lead to a set of equations relating the reflected and transmitted amplitudes for each polarization. They

are given by the following:

$$\begin{array}{cc} TE & TM \\ 1+r=t & 1+r=t \\ \beta(1-r)=\gamma t & \frac{\beta}{\epsilon_1}(1-r)=\frac{\gamma}{\epsilon_2}t \end{array} \tag{2.23}$$

Here r and t are defined by, $F_r = rF_i$ and $F_t = tF_i$. It may appear that equations 2.23 violate energy conservation, as the transmitted field seems larger than the sum of the incident and reflected field. Clearly this cannot be true. It must be remembered that these are actually complex amplitudes, containing any phase shifts in the scattered wave components, and the reflected wave comes with a π phase shift, i.e. a factor of -1, and energy is conserved, as it must be. With some algebra, these equations can be inverted to solve for the complex scattered amplitudes in terms of the propagation constants.

$$\begin{array}{cc} TE & TM \\ r=\frac{\beta-\gamma}{\beta+\gamma} & r=\frac{\beta/\epsilon_1-\gamma/\epsilon_2}{\beta/\epsilon_1+\gamma/\epsilon_2} \\ t=\frac{2\beta}{\beta+\gamma} & t=\frac{2\beta/\epsilon_1}{\beta/\epsilon_1+\gamma/\epsilon_2} \end{array} \tag{2.24}$$

This completes the problem of scattering from a planar interface. The results are general and may be applied to a variety of materials with complex dielectric functions or indices of refraction, provided that γ is chosen with the appropriate signs to obey the Sommerfeld radiation conditions.

2.2.2 INTERFACE GUIDED ELECTROMAGNETIC WAVE - THE SPP

The surface plasmon is a wave comprising strongly coupled electromagnetic and charge oscillations at the interface between two different materials. It is both a longitudinal EM wave and a wave of oscillation in the 2-D plasma at the surface of a metal. To understand the characteristics of such a wave let's reconsider the problem from the last section, scattering of a wave at the interface between two different non-magnetic materials.

Assume that there is already some energy existing in such a surface guided mode. Then we can use the results of the last section with a slight modification. Equation 2.23 derives from the boundary conditions, equations 2.10, and can still be used to describe the shape of a surface wave, if the 1 is replaced by 0. Since the 1 is describing the incident field intensity, and in this case we are assuming the wave is just travelling along the interface with no energy feeding into it, then the new amplitude of the incident wave is 0. The other terms, r and t, will still describe the form of the wave on each side of the interface satisfying the interface boundary conditions and Maxwell's equations. Equations (2.23) simplifies to

$$\begin{array}{cc} TE & TM \\ r = t & r = t \\ -\beta r = \gamma t & -r\frac{\beta}{\epsilon_1} = t\frac{\gamma}{\epsilon_2} \\ \downarrow & \downarrow \\ \beta = -\gamma & -\frac{\beta}{\epsilon_1} = \frac{\gamma}{\epsilon_2} \end{array} \tag{2.25}$$

The conditions are the poles of equation (2.24). There are multiple choices to handle complex phases needed to describe attenuating waves. Taking the convention that $\vec{k}$ and ω are real and β, γ are complex, the signs must be chosen to satisfy the radiation conditions, i.e. the component of the wave travelling away from the interface must propagate away from the interface if the propagation constants have real parts, $Re(\gamma) \geq 0$ and $Re(\beta) \geq 0$ and must attenuate as $y \to \pm\infty$, i.e. $Im(\gamma) < 0, Im(\beta) < 0$. Clearly β and γ cannot be real, or we would be describing waves propagating out to infinity with no source. The solutions must attenuate to have a finite energy, and to dissipate the energy which we assumed was already fed into the surface mode, so β and γ must be complex.

First, consider the case of TE polarization. Already all of these conditions just discussed are inconsistent with the TE requirements in (2.25), leading to $\beta = \gamma = 0$

and there is no surface wave. Moreover, even though they are no longer simply the projection cosines as they were in the case of a real ϵ, still α and β must satisfy the same condition, $\alpha^2 + \beta^2 = 1$, above the interface. This follows from the Helmholtz equation (2.8). Using this fact with equation (2.25) and the definition of γ given in (2.22), we are led to $(\frac{n_2}{n_1})^2 = 1$ which implies one of two possibilities, either $n_1 = n_2$ and there is no interface at all, or $n_1 = -n_2$ which is unphysical, at least for non-magnetic materials. We must conclude that an interface guided propagating wave cannot occur in the TE mode at a planar interface with non-magnetic materials.

The existence of metamaterials with large negative permeabilities does indeed allow a TE polariton solution [68, 69]. Also it has been shown it is possible to launch such a TE surface wave in heterostructures with multiple thin layers of dielectrics [70]. However, for the simpler case of a single metal-dielectric interface such as that studied in this research, no TE solutions are available.

For the TM configuration this is not the case, and there are no such contradictions eliminating the possibility of the existence of the surface guided wave in this polarization. Combining the definition of the index of refraction $n = \sqrt{\epsilon}$, the relations between α, β, and γ, and the TM constraints on a surface guided wave given in equation (2.25), we can solve for the components of the wavevector of the wave in terms of the dielectric functions of the materials involved. The propagation constant is defined as $k_x = \alpha k = \alpha\sqrt{\epsilon_1}k_0$ where k_0 is the wavenumber of the wave in free space. The result after some algebra is:

$$k_x = \pm k_0 \sqrt{\frac{\epsilon_1 \epsilon_2}{\epsilon_1 + \epsilon_2}} \tag{2.26}$$

The surface wave propagation constant and wavelength are modified relative to its free space value. Recall that the component of the electric field's wavevector parallel to the interface is constant across the interface, so the notion of a wave with a well-defined wavenumber along the interface is consistent. The sign of the propagation constant determines the propagation direction of the wave. Since real materials respond to

electromagnetic waves by moving charges around, a process which is inherently lossy due to charge carrier collisions, the wave amplitude must attenuate as it travels in order to satisfy this energy dissipation requirement, $sgn(Im(\alpha)) = sgn(Re(\alpha))$.

The relations between α, β, and γ also give us information about the wave profile in the y direction.

$$k_{y,j} = \pm k_0 \frac{\epsilon_j}{\sqrt{\epsilon_1 + \epsilon_2}} \tag{2.27}$$

Here j is 1 or 2, describing the transverse field profile in material 1 or material 2. In other words, $k_{y,1} = \beta k$ and $k_{y,2} = -\gamma k$. As usual, the sign in equation 2.27 must again be chosen so that the fields attenuate or propagate away from the interface.

In order to describe an evanescent wave then k_y must have an imaginary part in both media. If we temporarily ignore material losses, then ϵ_1 and ϵ_2 are real. In this case, β, γ will be purely imaginary. There are two requirements for this to be true. First the denominator under the sqrt in 2.27 must be negative, implying that $sgn(\epsilon_1) = -sgn(\epsilon_2)$. This is a general result of this type of surface guided wave. It may only occur in the TM mode and at an interface where the real part of the dielectric function changes sign, e.g. an interface between a metal and a dielectric. Secondly, observing equation 2.26, we see that both the numerator and denominator under the square root are negative. Therefore α is real, as expected. In order for a wave to propagate, α must at least have a real component, but in the lossless approximation it is entirely real.

Now that the transverse field is known, the electric and magnetic field components can easily be calculated from this using Maxwell's equations. This leads to the familiar result for TM waveguide modes. The only field components which are nonzero are B_z, E_x, and E_y. The electric field thus has a longitudinal component in the same direction as its propagation. It is a longitudinal wave, just like the bulk plasmon resonance we discussed in section 2.1.2. This is because this type of wave is in fact a strong coupling between the electric fields and the charges in the plasma at the

metal's surface.

We therefore conclude the following. The interface guided wave at a simple planar interface between two materials with different dielectric functions may occur only in the TM configuration and only at an interface where the real part of the dielectric function changes sign. This interface typically is between an insulator and a metal. We know that the dielectric function of an insulator is real, positive, and greater than unity, tending to slow down the phase velocity of light moving through it, while we see in equation 2.19 that the dielectric function of metals in the lossless approximation is real and negative and much lower than -1 at low frequencies. To this end, ϵ_1 will be henceforth called ϵ_d (for dielectric), and ϵ_2 will be called ϵ_m (for metal).

2.2.3 Dispersion relation of surface plasmon polaritons

In this last subsection concerning the phenomenon of SPPs, I will discuss some of their properties, the dispersion relation they follow, and the matter of coupling in and out of the SPP mode. Consider the Drude plasma dielectric function from section 2.1.2. Equation (2.19) with (2.9) leads immediately to a dispersion relation for bulk plasmons.

$$\omega^2 = \omega_p^2 + c^2 k^2 \tag{2.28}$$

In a similar fashion, equation (2.26) leads to a dispersion relation for the surface plasmon. Substituting equation (2.19) for ϵ_m leads to

$$k_x = \frac{\omega}{c}\sqrt{\frac{(\omega^2 - \omega_p^2)\epsilon_d}{(1+\epsilon_d)\omega^2 - \omega_p^2}} \tag{2.29}$$

The dispersion becomes asymptotic at the surface plasmon frequency, determined by the pole of the right hand side, $\omega_{sp} = \omega_p/\sqrt{1+\epsilon_d}$. This is also where $\epsilon_d = -\epsilon_m$, and the propagation constant diverges. This frequency will in general be smaller than the bulk plasmon frequency ω_p. Between the two frequencies lies a forbidden region where no propagation occurs. See figure 2.3. In both the small ω limit of the SPP

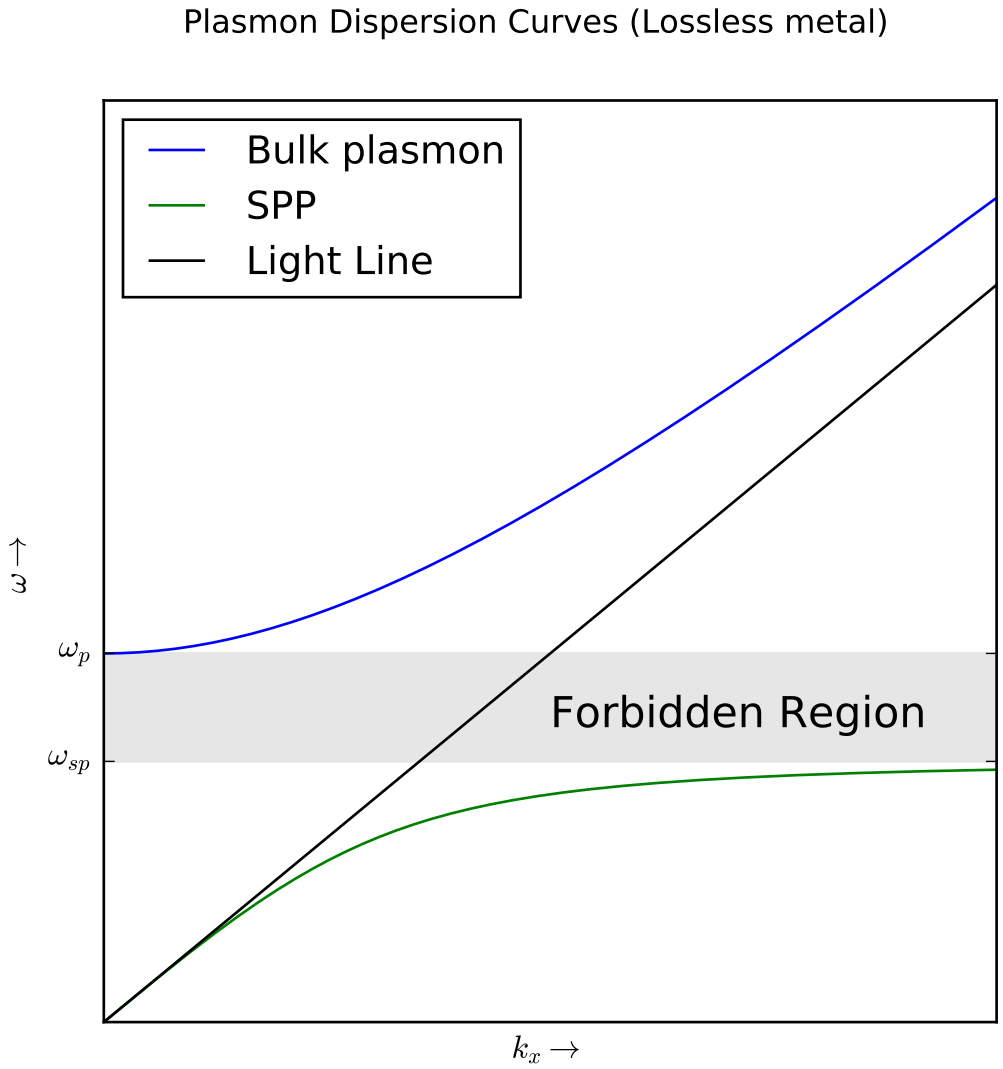

Figure 2.3 The dispersion curve for bulk plasmons and SPPs in the approximation of a lossless metal. There is a forbidden region due to the assumed lossless nature of the materials involved. In both the $\omega \to 0$ limit and the $\omega \to \infty$ limit the solution approaches the light line.

band and the large ω limit of the bulk plasmon band the solutions approach the light line.

Another interesting aspect of this type of wave is its propagation speed. The phase velocity, given by $v_p = \omega/k$, decreases compared to its free space value as k approaches the surface plasmon frequency. Also, the group velocity given by the slope of the curve, $\frac{d\omega}{dk}$, can be very small, so the wave propagates very slowly. Indeed in the lossless metal approximation both velocities will drop to zero as the wavelength collapses at the surface plasmon frequency.

In reality, the forbidden region occurs as a fiction resulting from the assumed lossless nature of the metal. In real materials there is instead a region of anomalous dispersion where two dispersion bands bend back towards each other and meet in the middle to form a single gapless band. However, at the surface plasmon frequency the propagation constant can still be quite large compared to the free space value. See figure 2.4. In the previously forbidden region, plasmonic modes are now available. Now that α is no longer strictly real, β and γ are not purely imaginary. The transverse wave profile is then no longer a simple exponential, but oscillations can extend away from the interface. This effect becomes appreciable when the negative dielectric function of the metal is no longer larger in absolute value than the positive dielectric of the insulator, and the propagation constant gains a large imaginary part. In this region the solution is only partially bound at the interface. Solutions between ω_{sp} and ω_p are sometimes called quasi-bound plasmons.

We have seen that the solution to the transverse component of the electric field at the metal-dielectric interface for the surface plasmon mode consists of (approximately) two exponential curves which decay in opposite directions and meet at a point on the interface. In contrast to typical dielectric waveguides whose modes are spread across the interior of its cavity, the surface plasmon propagates along an interface and its mode is very tightly confined there. This implies the light and therefore the

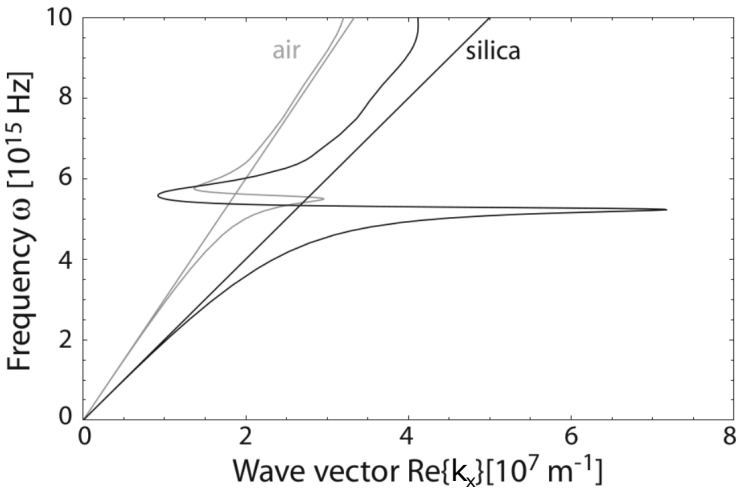

Figure 2.4 Dispersion curves and light lines for a silver/air interface and a silver/silica interface. Source: [71]. Quasi-boung plasmon modes now exist in the previously forbidden region. Note that the surface plasmon frequency is in the UV range, so plasmons launched at optical frequencies will be in the SPP band and therefore bound at the interface. Deviations from the light line in the bulk plasmon band at high energies are likely due to the effect of band transitions.

energy density of the electromagnetic field are highly concentrated. Furthermore we see that the wave propagation constant, i.e. the inverse wavelength, can be quite large as $\omega \rightarrow \omega_{sp}$. This implies a further concentration of light in the longitudinal propagation direction, so the light is tightly confined along two axes and the energy density is further enhanced. This crucial aspect of the SPP phenomenon allows the possibility of long range subwavelength optical propagation and plays a critical role in nanophotonics, bypassing the diffraction limited footprint of traditional photonic devices. Tightly confined light also leads to not only a large electric field enhancement in the neighborhood of the interface, but also large electric field gradients, leading to the potential for further interesting possibilities. For example, large electric fields can enhance nonlinear optical effects, which depend on higher orders of the electric field.

Since the SPP band does not cross the light line, light from free space will not enter or exit the SPP mode. To do so would violate conservation of energy and momentum. The SPP mode is therefore non-radiative at a perfectly flat planar interface. Efficient coupling of light into and out of the SPP mode will require some consideration for practical device design. In particular, efficient conversion will require altering the dispersion relation through the implementation of some kind of angular dispersion at or very near to the interface. The main methods for achieving this are traditionally through the use of a diffraction grating or some refractive material such as a prism. The phase matching condition for strong coupling is then most efficient at particular angles, where the added lateral momentum is just enough to reach the SPP band. Another approach, and the one used in the experiments presented in this thesis, is to exploit the resultant surface geometry itself, which will not be a perfectly flat surface, either the inherent surface roughness or in this case a sharp corner of a thin film, to provide the additional lateral momentum necessary to couple the free space and surface plasmon modes. A randomly rough surface can be considered as

a superposition of many gratings with many different spatial frequencies. This can be seen through Fourier analysis. This simplifies device fabrication at the cost of conversion efficiency. For a simple study of plasmonic influence on quantum emitters this will be sufficient. In the case of real device implementation, SPP conversion efficiency will likely have to be optimized, and the fabrication will be more complex.

This section concludes our discussion of the surface plasmon. In the previous subsections we have discovered the longitudinal surface plasmon wave, known as SPP, and discussed its properties how it can be excited. The wave propagates along the surface between a metal and dielectric, or between any two materials where the real part of the dielectric function changes sign, and is evanescent in its transverse profile. We have seen that it can only be excited by TM radiation and that additional angular dispersion is needed to get the light cone and SPP band to cross. The research in this thesis concerns the study of the interaction between these waves and excitons confined in quantum dots. The rest of this chapter is dedicated to discussing the theory of crystalline materials and quantum dots.

2.3 Review of crystalline materials

This section provides a brief overview of the theory of crystalline materials. I begin with a discussion of the Bravais lattice and the states which form in a periodic potential. Then I talk about semiconductor materials, their charge carrier dynamics, and the formation of excitons. This discussion will be relevant to the following section which gives details about the type of quantum dots studied in this research..

2.3.1 Wavefunctions in a periodic potential

A very common arrangement of matter in the solid state is the lattice structure, in which atoms form a periodic structure with predictable positions relative to each other. The principle object of study is the Bravais lattice, an idealized, defect-free,

infinite lattice described by a set of basis vectors $\vec{a}_1, \vec{a}_2, \vec{a}_3$ and the set of atoms occupying each lattice site position. The lattice sites are the set of vectors $\{n_1\vec{a}_1 + n_2\vec{a}_2 + n_3\vec{a}_3$: for all integers $n_1, n_2, n_3\}$. Each site may include a so-called basis of atoms, a group of atoms with fixed positional offsets from the lattice site. This basis forms the unit from which the lattice can be built by cloning the basis at every lattice site. The III-V semiconductors studied in this work consist of a lattice with a 2-atom basis in the zincblende structure.

While single crystalline materials are rare and difficult to fabricate, many materials are formed from large scale aggregations of small pieces of single crystals. Such polycrystalline materials suffer from carrier collisions at the boundaries between the single crystals. However the Bravais lattice idealization still gives a useful insight into how the periodic potential affects the distribution of electronic wavefunctions within real materials. In fact no crystalline material is perfect at real (i.e. nonzero) temperatures, as each lattice site's occupancy probability may be described by an Arrhenius term, giving a nonzero probability of lattice defects due to thermal fluctuations, even in a nominally perfect single crystal.

The Fourier transform of the Bravais lattice is another lattice of wavevectors called the reciprocal lattice. For any two vectors, $\vec{R}$ in a Bravais lattice and $\vec{K}$ in its reciprocal lattice the following holds.

$$e^{i\vec{K}\cdot\vec{R}} = 1 \tag{2.30}$$

In a simple model, ignoring electron-electron scattering, and using the idealizations of the Bravais lattice, the electronic behavior can be qualitatively modeled by means of a Schrodinger equation with a potential energy having the periodicity of the Bravais lattice. Effects due to defects can be added in perturbatively later. The base Hamiltonian is then symmetric under the action of a translation operator, defined by $T_{\vec{R}} : \psi(\vec{r}) \rightarrow \psi(\vec{r}+\vec{R})$ for any lattice vector $\vec{R}$. The Hamiltonian therefore commutes with these translation operators and there must be a shared basis of eigenstates for

both operators. These states are called Bloch waves, and it can be shown they can be described by a product of a plane wave and a function representing the underlying atomic contribution to the local potential.

$$\psi_{n\vec{k}}(\vec{r}) = \frac{1}{\sqrt{V}} e^{i\vec{k}\cdot\vec{r}} u_{n\vec{k}}(\vec{r}) \tag{2.31}$$

Such a state has has two quantum numbers. n is an integer called the band index and $\vec{k}$ is a quasi-continuous domain containing all vectors in a primitive unit cell of the reciprocal lattice, a region of reciprocal space containing all the possible values of $\vec{k}$. The allowable values of $\vec{k}$ do not span all of reciprocal space, as there is a degeneracy between them due to the periodic lattice structure which is lifted by the band index. Typically the first Brillouin zone is used as a convenient primitive unit cell. The first Brillouin zone contains all points in reciprocal space which are closer to the site at $\vec{k} = \vec{0}$, than to any other site in the reciprocal lattice.

It can be shown that the periodic potential implies that $u_{n\vec{k}}$ must have the same periodicity as the Bravais lattice.

$$u_{n\vec{k}}(\vec{r} + \vec{R}) = u_{n\vec{k}}(\vec{r}) \tag{2.32}$$

for any $\vec{R}$ in the Bravais lattice. As the reciprocal lattice has multiple periodicities itself, any vector $\vec{k}$ in a primitive cell of the reciprocal lattice is equivalent to any other vector $\vec{k} + \vec{K}$ for any $\vec{K}$ in the reciprocal lattice. This follows from (2.30) and is the reason for the reciprocal space degeneracy already discussed. Each vector in the first Brillouin zone therefore corresponds to an infinite number of states, delineated by the band index.

Energy bands occur as a result of exchange splitting due to wavefunction overlap among the electrons spread across the lattice. That is, as separate electron states are brought close together, significant overlap of their wavefunctions occurs, and it results in orbital hybridization, where new states form which extend over the entire spatial range of the previously separate states. This splitting occurs on a massive

scale as even microscopic samples contain huge numbers of atoms, N. The energy separation between the formerly degenerate states scales like $1/N$, leading to an essentially continuous $\vec{k}$ domain. Band gaps occur at regions between the bounds of two adjacent bands. Electrons do not occupy states in the band gaps, as they are energetically forbidden.

It is clear from (2.31) that the lattice orbitals are delocalized and spread across all of space due to the orbital hybridization, with the only spatial dependence in the probability density arising from the atomic contributions, $u_{n\vec{k}}(\vec{r})$. This is an approximate description of electrons in the higher energy bands, such as the valence and conduction bands, although in real materials defects and boundary conditions will restrict the extent of the real wavefunction to some degree. In these higher bands the electrons are the most weakly bound, leading to large wavefunction overlaps and strong exchange splitting. In other words the bands are the widest at higher energies. For more strongly bound electrons, such as those in lower atomic energy states or electrons producing permanent dipole moments, a more appropriate set of basis states are the Wannier states which are maximally localized around a lattice site.

$$\phi_{n\vec{R}}(\vec{r}) = \frac{N}{\Omega}\int_{BZ} d^3\vec{k}e^{-i\vec{k}\cdot\vec{r}}\psi_{n\vec{k}}(\vec{r}) \tag{2.33}$$

Here the domain of integration is the first Brillouin zone, and Ω is its volume.

Electrons fill the energy bands starting from the lowest energy state with occupancy probabilities given by the Fermi-Dirac distribution. Thus all lower energy core electrons are filled almost certainly, but at higher energies near the Fermi level there can be some electrons existing in higher energy states even though lower energy levels are available to them. This is the result of thermal fluctuations, and depends on the type of material. The highest energy band which is not filled at zero temperature is called the conduction band. The band below this is called the valence band. Materials which have a partially full conduction band, even at zero temperature, are called metals. In these materials, electrons occupy states at the Fermi level. A full

band cannot conduct an electric current under the influence of a weak external field since the Pauli exclusion principle prevents tunneling to adjacent states in the same band. Electrostatic breakdown can of course occur if the electric fields get very large. The partially empty conduction band is what gives metals their characteristic large electrical conductivities, even in response to weak fields.

Semiconductors and insulators have empty conduction bands in their electronic ground state at zero temperature. Here the Fermi level lies in the bandgap between the valence and conduction bands. At nonzero temperature, thermal fluctuations elevate electrons from the valence to the conduction band, leaving behind a hole in the valence band. The hole in the occupancy of the valence band states creates a positively charged quasiparticle also called a hole. Both conduction band electrons and valence band holes contribute to electrical conductivity. While the distinction between semiconductor and insulator can be somewhat arbitrary, a semiconductor generally has a small enough bandgap for a significant number of electrons to be thermally injected into the conduction band at typical operating temperatures.

A common technique in semiconductor manufacturing is the intentional introduction of dopant atoms into a crystal. This introduces new weak bonding sites with very low ionization energies. An n type donor dopant introduces a new atom with a very weakly bound electron near the Fermi level. This electron tends to detach from the atom and move freely throughout the material. Similarly, a p type acceptor dopant tends to capture an extra electron leaving an extra free hole behind. The increase in free carriers results is an increase in electrical conductivity. An n-doped (p-doped) semiconductor injects extra electrons (holes) and shifts the Fermi level towards the conduction (valence) band. Heterostructures can be formed by combining different types of crystals into a single device. The electrons reach thermal equilibrium and the bands bend to fix the Fermi level at a single energy across the device. The band bending effect leads to an excess of charges on one side of the interface, causing a

persistent internal electric field in the region near the interface and a so-called depletion zone where free charge carriers are driven away. The common p-n junction diode, for example, uses a junction of p-type and n-type semiconductor to produce an asymmetric conductivity which prefers to conduct current in only one direction due to its intrinsic electric field.

The interface between a metal and a semiconductor can produce another type of interface called a Schottky contact. A Schottky contact pins the Fermi level across the interface, bending the band structure of the semiconductor near the surface and adding an additional potential barrier and therefore intrinsic field that carriers must overcome to conduct a current through it. This is due to metal-induced gap states just inside the surface of the semiconductor, and it also causes a depletion zone and asymmetric conductivity. This is known as a Schottky diode.

2.3.2 Excitons

The energy of an electron near a band extremum can be expanded in a Taylor series.

$$\mathcal{E}(\vec{k}) = \mathcal{E}_{c,v} + \frac{\hbar^2}{2}\sum_{i,j} M_{ij}^{-1} k_i k_j + \mathcal{O}(\vec{k}^3) \tag{2.34}$$

In this example the expansion is around $\vec{k} = \vec{0}$ but the generalization is straightforward. The first order term is not written because it's coefficient is 0, since the expansion is around an extremum. The quantity $M_{ij}^{-1} = \frac{1}{\hbar^2}\frac{\partial^2 \mathcal{E}}{\partial k_i \partial k_j}$ is the inverse effective mass tensor which averages over the influence of the complex internal fields on the inertial response of the charge carriers. For the simple case of of an isotropic, symmetric extremum the effective mass can be described by a simple scalar m^*, which is positive (negative) for upward (downward) bending bands like the conduction (valence) band. The correspondence between band curvature and inverse mass follows from the classical mass-energy relation of a free particle, $E = \frac{\vec{p}^2}{2m}$, and the relation between wavenumber and momentum, $\vec{p} = \hbar\vec{k}$. Thus, near the extremum of an unfilled

band, crystal charge carriers act as nearly free particles with altered masses given by the inverse of the band curvature at that point.

In a semiconductor crystal there are just enough electrons to completely fill the valence band in the ground state. Excited states which increase conductivity are achieved through carrier injection by exciting electrons into higher bands, especially from the valence band to the conduction band. This can be achieved through a number of mechanisms, e.g. thermal fluctuations or photoexcitations. As particles tend to settle in states with the lowest available energy, electrons tend to settle at the bottom of the conduction band, and holes at the top of the valence band. The hole attracts other nearby electrons into its electric field via Coulomb interaction. When an electron and hole become trapped in each other's potential, they form another quasiparticle bound state called exciton.

Nanocrystals can also trap single charge carriers in their ground state. When an exciton is excited in this configuration it will have a net charge. See figure 2.3.2. Excitons with one net unit of fundamental charge are called trion. Higher charge species can also occur. It is also possible for carriers bound to a lattice site to attract other carriers. An exciton of this type is called Frenkel exciton. This research will focus on Wannier-Mott type excitons where both charges are delocalized.

Unlike silicon, III-V semiconductors like GaAs and InGaAs are direct bandgap materials, i.e. the valence band maximum and conduction band minimum occur at the same point in $\vec{k}$-space, in this case the origin $\vec{k} = \vec{0}$. As photons have negligible momentum, this allows a large quantum efficiency or conversion of photons to excitons. The coupling of vacuum electromagnetic modes to this interband transition produces large numbers of excitons under excitation by photons with sufficient energy. These materials therefore offer exceptional performance for optoelectronics and photonics applications.

The inverse consequence of this coupling is their large photoluminescence, the

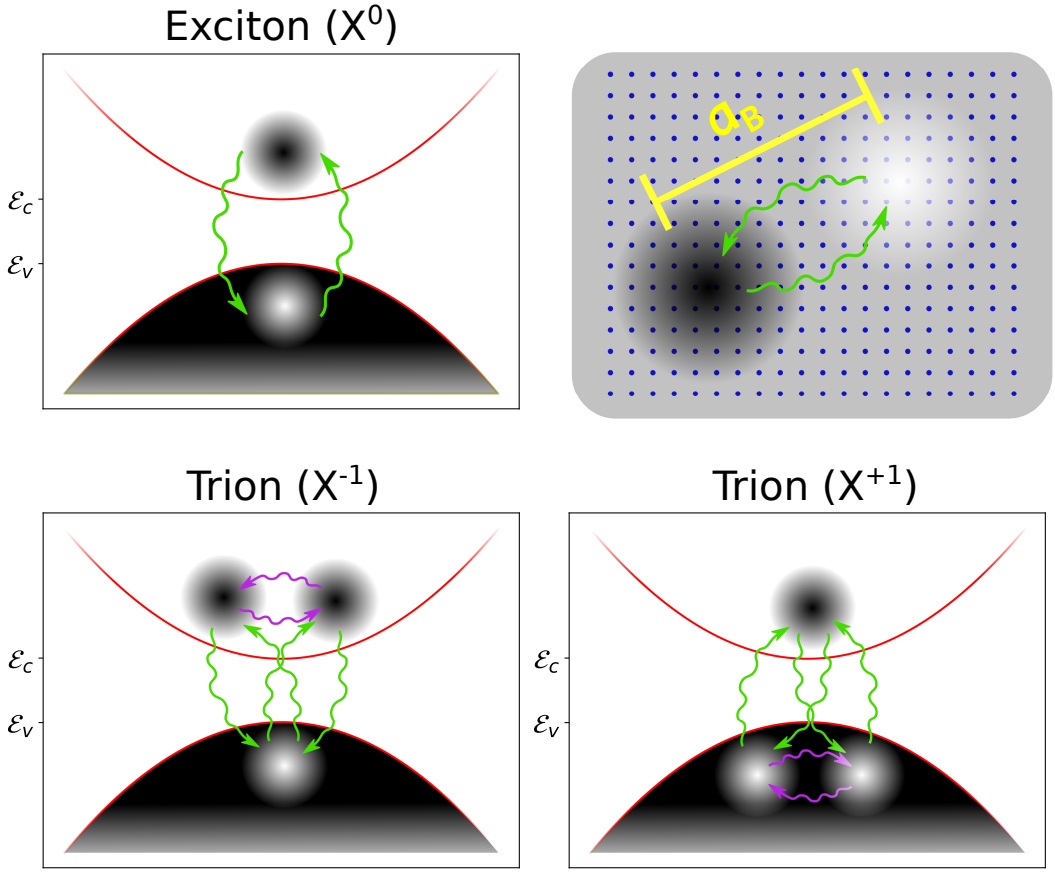

Figure 2.5 The bound state of electron and hole. The electron and hole extend over many lattice sites forming the Wannier-Mott type exciton, separated by the exciton Bohr radius, a_B. Besides the neutral exciton, other charge states are possible, including $\pm e$ trions and even higher multiples of the fundamental charge.

ability to re-emit light from energy stored as excitons. An electron bound in an exciton will eventually fall back into the valence band hole, a process called recombination, destroying the exciton and carrier occupancies and releasing the binding energy of the exciton as light, a process similar to photoproduction from positronium (electron and positron) annihilation. However, unlike positronium, excitons can emit single photons and use their atomic environment to balance any residual momentum. Positronium tends to emit photons in pairs when it decays in order to balance momentum.

2.4 Theory and characterization of InGaAs quantum dots

In this section I will discuss the properties of the types of structures used in this research. This builds upon the information discussed in the last section. After this section the reader should have enough background information to understand the types of quantum dots used in this research.

2.4.1 Quantum confinement

Quantum confinement occurs when a particle is contained in a region whose size is smaller than the length scale of the particle's wavefunction. For confinement of excitons the scale is the exciton Bohr radius.

$$a_B = \frac{4\pi\epsilon_d\epsilon_0\hbar^2}{\mu e^2} \tag{2.35}$$

The exciton Bohr radius is increased from the usual atomic Bohr radius by two factors. First is the factor ϵ_d, the dielectric response of the material which screens the electric fields and weakens the Coulomb interaction between the electron and hole. Second, the mass in the excitonic Bohr radius is different from the bare electron mass.

For QDs the excitons tend to be of the Wannier-Mott type, i.e. neither the electron nor hole are localized around a lattice site, and each must be described by their effective mass, m^*. The equation for the atomic Bohr radius contains the bare electron

mass, or more precisely the reduced mass in the problem of an electron orbiting a nucleus which, due to the huge disparity in the masses, gives essentially the same quantity as the bare electron mass. For excitons, this must be replaced with a much smaller reduced mass describing a delocalized electron and hole, $\mu = \frac{m_e^* m_h^*}{m_e^* + m_h^*}$. As a consequence of these factors and also the extended nature of the carrier wavefunctions themselves, the excitonic wavefunction is extended over a large number of lattice sites.

Single material nanocrystal QDs have long suffered from the problem of blinking, intermittent disruptions in the fluorescence, thought to be a result of carriers tunneling into interface states at the surface of the crystal, although alternative mechanisms have been proposed involving other non-radiative relaxation mechanisms [72]. One technique to achieve better confinement and prevent such leakage is to place a piece of semiconductor, of a scale below the critical size, inside a bulk piece of another semiconductor having a larger bandgap [73]. The QDs studied in this work are of this type.

Quantum confinement imposes restrictions on the available wavevector components for free carriers. For example, a quantum well confines the carrier wavefunctions in the direction of one spatial axis. A particle confined to the xy-plane must have $k_z = 0$. Every time the dimensionality of the system is reduced it causes abrupt changes to the available density of states for free carriers. See figure 2.6.

The quantum dot (QD) is a structure which confines its excitons in every spatial direction, making it an essentially point-like particle. The carriers are completely confined by the altered boundary conditions and cannot move. They are restricted to states where $\vec{k} = \vec{0}$. As a result the density of states becomes discretized and only a few energy levels in the valence and conduction bands are available. Quantum dots exhibit discrete emision spectra, similar to atomic transition spectra. They are commonly called artificial atoms for this reason.

One of the advantages of using quantum dots over atoms as light emitters is the

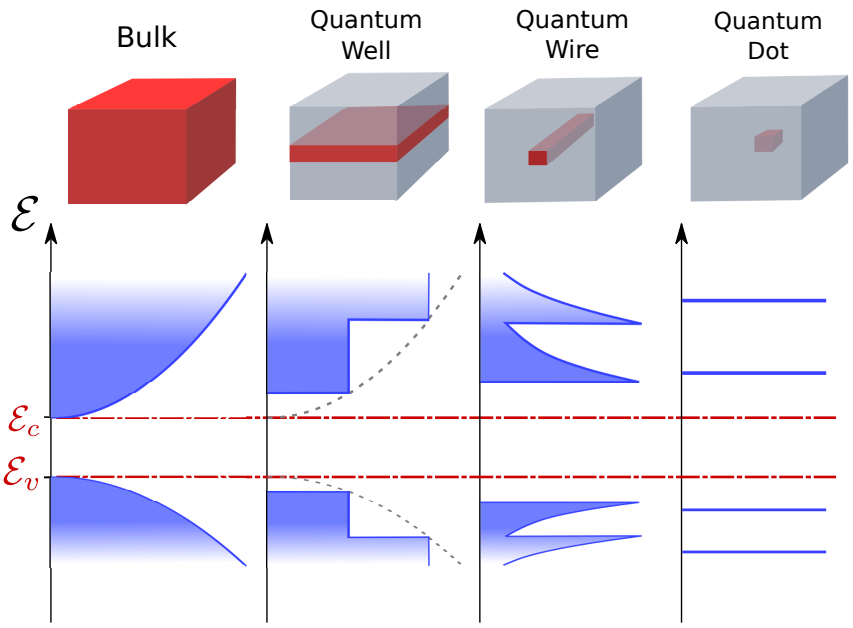

Figure 2.6 A qualitative picture of the available density of carrier states of a semiconductor system. As the dimensionality of the system is reduced the DoS changes abruptly. For 0-dimensional QDs the states are effectively discrete.

ability to exploit the distributed nature of the exciton wavefunction. A QD may contain between 10^3 and 10^6 atoms, a scale more easily addressable through modern nano-fabrication techniques than the manipulation of individual atoms. Furthermore, the fact that the boundary conditions can be finely tuned allows the energy of the states and therefore the wavelength of any luminescent emission to be tuned by changing the dimensions of the structure. By reducing the size of the nanocrystal, the electron and hole wavefunctions are forced closer together, increasing their binding energy, and vice versa. This is called the quantum size effect, and this tunability makes the QD very versatile as a single photon source.

2.4.2 Self assembled InGaAs quantum dots

The QDs studied in this research were grown at the Naval Research Laboratory by molecular beam epitaxy (MBE). The method for formation of the QDs is epitaxial growth of InGaAs atop a layer of GaAs, followed by a final capping layer of GaAs to fully encapsulate the dots. InAs grows on GaAs in the Stranski-Krastanov (SK) MBE mode forming a thin quantum well layer, called wetting layer, and small islands of self-assembled nucleated extrusions. SK growth occurs as a result of a lattice constant mismatch between the two materials. In general a Bravais lattice has three lattice parameters. However the zinceblende lattice structure of these III-V semiconductors is a face-centered cubic lattice with a 2-atom basis in which all three lattice parameters are equivalent, so the crystal can be described by a single lattice constant. The lattice constant of GaAs is 5.6533Å, and that of InAs is 6.0584Å, while $In_xGa_{1-x}As$ obeys Vegard's law, i.e. it's lattice constant varies between the two extremes linearly with the parameter x [74]. As a result of this mismatch there is an excess of strain in the epitaxially grown film. The film will grow monatomic films only to a certain critical thickness. Past this it is energetically favorable for the atoms to aggregate into nucleations rather than simply increase the film thickness with additional monolayers.

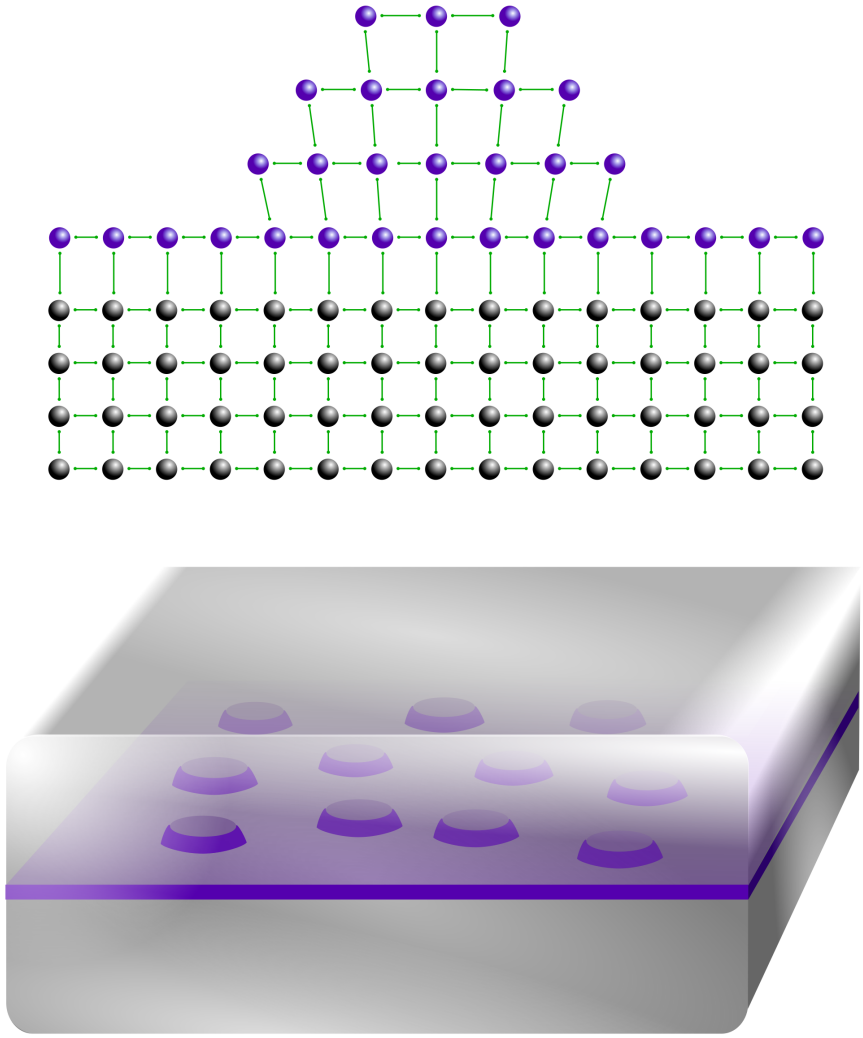

Figure 2.7 *Top* The Stranski-Krastanov mode of epitaxial growth creates a wetting layer film with nucleated islands. The upper atoms prefer to settle on top of the islands rather than in the film due to the strain of aligning with the lattice of the underlying substrate. *Bottom* The formation of self-assembled QDs by SK epitaxial growth of InGaAs atop GaAs. The dots are further encapsulated with an epitaxial capping layer of GaAs.

These nucleations form the core of the QD structure. Once the islands have been formed the sample is encapsulated with an additional layer of GaAs.

The particular sample used in these experiments was grown atop a 0.5mm N^+ doped GaAs wafer. The high level of doping provides a large conductivity and a quality Ohmic contact at the bottom of the sample. Atop this was grown a 40nm buffer layer of insulating GaAs, followed by InGaAs QDs with a nominal of thickness of 2.5nm, followed by a 280nm capping layer of insulating GaAs. The n-type GaAs pins the Fermi level near the conduction band. See figure 2.8. Its junction with the i-GaAs creates a depletion region across the upper layers of the sample.

Changes in the charge states of excitons forming in the QDs can be induced by exerting an external electrical bias across the sample. Forward biasing pushes the bands of the insulating parts of the sample downward on the energy axis, lowering the energy of the states. This increases the likelihood of the QD and therefore its excitons to be negatively charged. Reverse biasing lifts them upward, and reduces the likelihood that they are negatively charged.. The doped substrate, being more conductive, responds to external fields by reconfiguring its charge carriers until the field is completely screened out, canceling out the internal field, rather than bending the bands. Its energy bands therefore shows little effect under the influence of such a bias.

This mechanism gives an extra electrical mode of control over the PL dynamics of these types of QDs. For example, as the strength of a reverse bias increases, it lowers the lateral scale of the potential barrier which is confining any carriers inside the dots. This decreases the tunneling time for electrons to tunnel out of the dot into the GaAs conduction band, and holes out into the valence band. At a large enough bias the tunneling time is reduced below the exciton recombination lifetime. This mechanism acts as an electrical switch to effectively turn off the PL of the dots.

The buffer layer's thickness plays a crucial role in the internal charge dynamics

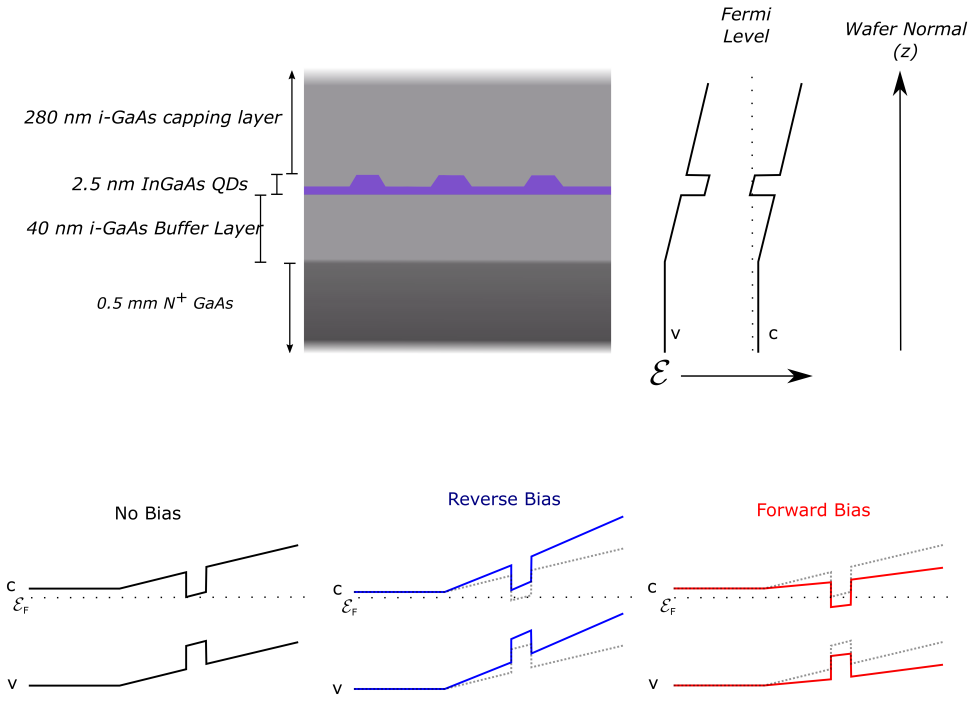

Figure 2.8 *Top Left* The structure of the QD sample used in this research. *Top Right* The associated band structure as a function of position along the axis normal to the wafer. The doped substrate pins the Fermi level close to the conduction band, encouraging the production of negatively charged dots. *Bottom* The effects of biasing the sample on the band structure.

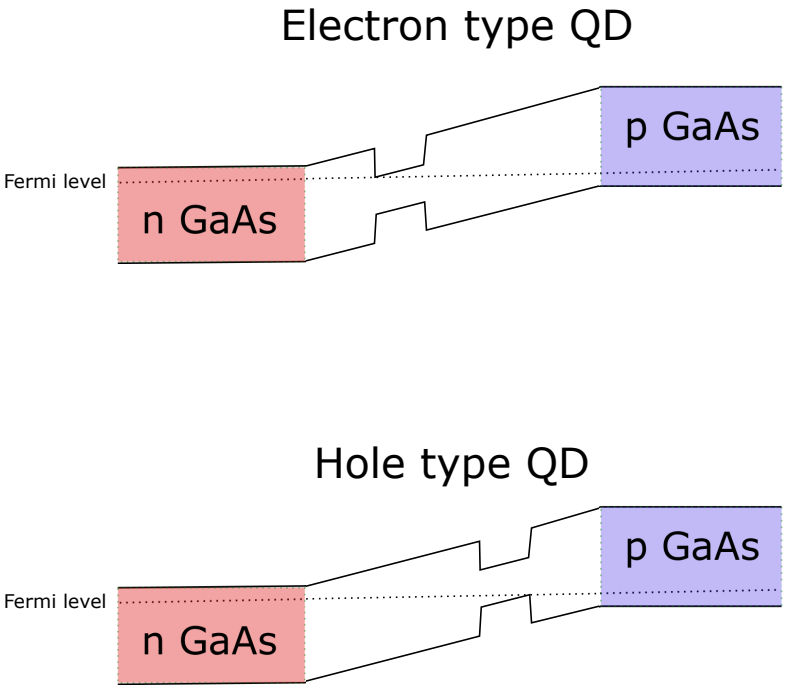

Figure 2.9 p-i-n type QDs use n-type, p-type and insulating GaAs layers to alter the charge dynamics. The types of exciton charge species which will be excited can be modified during MBE growth by altering the distance of the dot layer from the conducting layers. *Top* A quantum dot which will tend to capture electrons and emit photons from negatively charged excitons. *Bottom* A quantum dot which will tend to capture holes and emit from positively charged excitons.

of the QD. At a lesser thickness like the one in our sample, the bottom of the QD conduction band potential well dips into the Fermi sea, charging the dots with electrons. In this configuration the dots tend to form more negatively charged excitons. Increasing the thickness brings the valence band maximum at the dot layer closer to the Fermi level, reducing this effect. Note the buffer layer is the first section of the sloping bands and the N+ GaAs is the flat section. A thicker buffer layer would push the center of the QD energy closer to the Fermi level, reducing their tendency to form negatively charged excitons and increasing their tendency to form positively charged ones. By reducing the capping layer thickness and growing p-type GaAs on top, it is also possible to form QDs where the valence band touches the Fermi sea rather than conduction band, which would tend to produce positively charged excitons. See figure 2.9. Such p-i-n QDs can be tuned during fabrication to prefer certain charged species of excitons.

2.5 Chapter Summary

This chapter provided a brief review of some of the theoretical topics related to the research performed in this work. We started with a brief discussion of classical electrodynamics and simple polarization models. We then discussed the problem of plane wave scattering at a planar interface. The results of this solution were then generalized and applied to the problem of a surface guided wave. We found that such a propagating wave exists only in the TM polarization and only at the interface between two materials where the real part of the dielectric function changes sign. Such a wave is called a surface plasmon polariton. We then invoked some of the results of previous sections to discuss some of the properties of such a wave.

The discussion then pivoted to a review of the behavior of electrons in crystalline matter. We discussed the band theory of solids, and the idea of electrons and holes which carry charges in these bands. Then we reviewed the concept of excitons and

considered the effects of quantum confinement of excitons. We talked about the different possible dimensionalities of such a confinement and mentioned their effects on the density of electronic states. Finally we examined the self-assembly of quantum dot structures in the Stranski-Krastanov MBE growth mode. In the next chapter, we will discuss the fabrication of these types of QDs into a hybrid plasmonic device and the experimental techniques we used to probe and characterize this device.

Chapter 3

QD/plasmonic hybrid device

In this chapter I describe the setup for the experiments described in this work. The first section details the processes involved in the fabrication of the hybrid plasmonic/QD device which we have investigated. The fabrication strategy was to lithographically define the shape of the plasmonic features, etch into the capping layer to get closer to the dots, deposit a silver film into the etched pattern which would support plasmonic modes, lift off the resist, and coat the rest of the wafer with a semi-transparent layer of chromium to form a Schottky diode. The chromium provides an electrical gate while still being semi-transparent, giving us the ability to excite and study the dots optically while allowing some control over the internal field and therefore the exciton charge species which form. After affixing the sample to a chip carrier and connecting the top and bottom surfaces to electrodes, we then have a completed hybrid plasmonic/QD device with an electrical gate allowing the application of an external bias across the sample.

The last section details the setup of the micro photoluminescence experiment which was used to characterize the device. It describes the optical setup we used to both excite and collect the QD signal, and how we exerted control over the parameters of the laser excitation, such as incident polarization and incident power. After describing how we fabricated the sample and collected the data, the next chapter will begin detailing what we found.

3.1 Sample fabrication

3.1.1 Wafer preparation

The original sample came as 1/4 of a circular wafer, cut from a 2 inch wafer. From this I diced a small sample a few mm on each side. It is important when using the following method of dicing to be sure to start with a clean soft surface, such as lens paper, and clean microscope slides. The slides should be cleaned with methanol and dried before beginning. This will remove any residue or dust from the glass. Failure to do this may result in scratches on the surface of the sample.

Dicing was performed with a diamond scribe and some microscope slides. Using a microscope slide as a straight edge, I marked the area to be cut with the scribe. After this step, compressed air should always be used to blow away any dust to avoid scratching the sample. I then placed the marked sample between the large faces of two microscope slides, with their edges aligned with the scratched line of the sample, such that the bulk of the sample was firmly held in place between the slides, while the section to be cut protruded out from between them. A third microscope slide was placed over the protruding section in order to distribute the applied force over its surface. Lightly pressing down on the top of one of the slides to hold the sample in place, I used the blunt edge of a pair of tweezers to tap the other slide until the sample broke. It tends to break right along the line of the inscription.

After dicing, the sample went through a standard cleaning procedure, sonication in acetone, rinse in IPA or methanol, dry with compressed N_2, in that order. In order to remove any stubborn organic residue and to get an optimally clean top surface, the sample was dipped in a 3% mixture of HCl and water for a few seconds. This was followed by a rinse in distilled water and another drying with N_2.

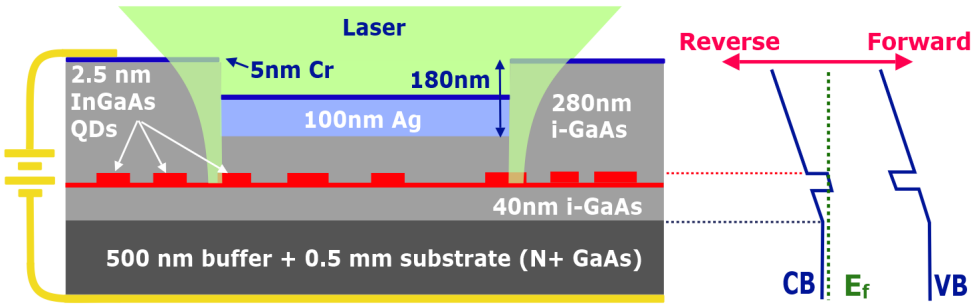

Figure 3.1 The ideal structure of the QD sample after completion of fabrication. (Not to scale) After lithographically defining the features, the capping layer was etched down to 100nm. Inside the pattern we deposited 100nm of silver. After liftoff of the PMMA mask we deposited 5nm of chromium to complete the Schottky diode. The Cr layer is semi-transparent while the silver is opaque. The electrical gate gives us some control over the charge states of the excitons which form in the dots. The experiment was performed by exciting the dots close to the silver structures as shown in the picture. We also collected control data by exciting far away from any silver.

3.1.2 Electron-beam lithography

As a mask for electron-beam lithography (EBL) we used poly-methyl-methacrylate (PMMA) with a molecular weight of 950k dissolved as 4% of an anisole solution. However, the sample I cut was too small to cover the O-ring on the spincoater, so I first used a thick layer of PMMA, spun at 1000rpm, as an adhesive to attach the sample to a one inch Si wafer. A 5 minute bake at $180°C$ is sufficient to harden the resist layer. After the sample was attached to its holder, I used the spincoater to apply a 200nm thick layer by spinning at 3500 rpm. The spin curve, which details the resultant film thickness as a function of angular velocity, can be found online at the manufacturer's website. The sample was then baked again to finalize the resist layer on top of the sample. When attaching the sample to the sample holder for the scanning electron microscope (SEM) it is important to ground the top surface of the sample to the metallic sample holder with conductive tape since the Si and PMMA layers will not allow excess charges to escape. Failure to do so will result in poor imaging as the beam imparts too much charge onto the surface of the sample. The charge cannot escape fast enough, and since the imaging is enabled through charge scattering off the surface of the sample, image quality suffers.

Our decision to use a single layer of 950K PMMA is not typical with many EBL processes. One often finds the use of double layers, with higher molecular weight PMMA deposited atop another layer of PMMA with a lower molecular weight, such as 495K. We chose our procedure for the following reasons. Higher molecular weight tends to produce less of an undercut, i.e. it forms more vertical sidewalls in the mask. Typically, if one is depositing thin films into a patterned mask atop a substrate, this can be undesirable because PMMA is very sticky. The deposited material can be pulled off of the sample along with the mask during the liftoff procedure if they are in contact with each other. To avoid the possibility of any deposited film touching the sidewall of the high molecular weight PMMA mask, it is advisable to put a low

molecular weight layer underneath it, which will form an undercut and leave a gap between the deposited film and the PMMA sidewall.

However, since we decided to first etch into the substrate before depositing any metal, and since our target film thickness was less than the target etch depth, the metal should be deep inside the etched groove and should not be able to contact the PMMA. Therefore liftoff should not cause any such issue. Furthermore, the lack of sidewalls is exactly what we want, especially since our etch procedure is isotropic. Etching under a mask with an undercut would significantly widen the features we were trying to create, lowering the resolution we could obtain. Since this is undesirable, we decided to use a single layer of high molecular weight PMMA for our mask. In this way, we achieved the higher resolution offered by the higher molecular weight PMMA, but with reliable patterning of deposited films. Despite this different approach, I still used the standard exposure and development procedure. This should also be optimized to take the thin single layer resist into account. It may improve the achievable resolution for future samples if using the PMMA and wet etch procedure.

We also acquired another e-beam resist, Zeon Chemicals ZEP520A, which is more suitable for dry etching. The process for exposure and development using ZEP520A resist should also be studied and optimized. In general ZEP requires less exposure dose than PMMA. I have also found it is quite common for cracks to form in the resist during development, although it doesn't appear to have much effect on the subsequent etch. This may be due to the fact that I was using the same developer for the ZEP instead of the official recommended developer. The ZEP resist in general was less easy to use compared to PMMA, and often the resist layer was just not as clean as PMMA consistently was. Part of this may be because I was depositing a much thicker layer than what I used for PMMA. For PMMA the layer thickness is irrelevant because the wet etch does not attack the resist, so using a very thin layer is acceptable. Using ZEP and dry etching this is not the case. Unless you use a very

hard mask, the dry etch procedure will attack the resist as well as the substrate, so it is necessary to use a thicker layer.

The microscope used for EBL was a Jeol JSM-840A. Lithography was performed with 30keV electrons at a working distance of 8mm. To achieve maximum resolution I used the lowest current setting which was measured at 3pA. After EBL was complete, the sample was removed from the SEM and the sample holder. The pattern was then developed in a mixtures of one part methyl isobutyl ketone (MIBK) to three parts isopropanol (IPA) for 30s, rinsed in IPA for 10 seconds, and dried with compressed N_2, completing the mask for etching.

3.1.3 Wet chemical etch

In order to get the plasmonic structures closer to the QDs we etched away part of the capping layer using the lithographically defined pattern as a mask to preserve the capping layer elsewhere. In this sample we etched 180nm of capping layer away leaving 100nm of capping layer. This is just inside the range of influence of the plasmonic fields [75], but should avoid significant weakening of dot confinement.

The etch was performed in a weak acid solution containing 495 parts distilled water, 1 part phosphoric acid (H_3PO_4), and 4 parts hydrogen peroxide (H_2O_2). The acid itself does not attack the substrate, but it will attack any oxides formed on the substrate. GaAs itself does not have a natural oxide, but the oxidizing agent does produce small regions of oxides of Ga and As separately, which the acid carries away. This solution achieved an etch rate of 0.5 nm/s. The etch was performed for 6 minutes, followed by a rinse in distilled water and quick dry with N_2.

An ideal fabrication procedure would be done with a dry etch procedure, e.g. reactive ion etching (RIE). RIE uses a gas which ionizes to form reactive compounds under the influence of an RF electromagnetic field. The field drives the reactant up and down repeatedly while mostly avoiding the sidewalls, achieving a highly anisotropic

etch. The etch procedure described in this section is more isotropic in nature, meaning it tends to etch laterally at the sidewall as well as downwards. This leads to the possibility of gaps between the silver structure and the GaAs sidewall, which would weaken the confinement of nearby dots if done too close to the dot layer. Furthermore, it limits the resolution of the lateral dimensions of our plasmonic structures, making it difficult if not impossible to fabricate certain types of interesting structures, e.g. metal-insulator-metal (MIM) type features which can couple plasmonic modes on two nearby metal surfaces. All attempts to do this resulted in the middle layer of GaAs being etched away.

The proper gas chemistry for RIE of GaAs however involves the use of chlorinated gases. These gases tend to be highly toxic and require special equipment. An alternative we found is the use of Freon-12, with chemical formula CCl_2F_2, a formerly common refrigerant which is not dangerous to human health. However production was banned due to its effects on the Earth's ozone layer. The absence of ready availability of these gases at our facilities constrained our ability to optimize the sample. Future studies seeking to improve on the design of a similar device should absolutely be done with samples fabricated at facilities with the proper equipment to optimize the etch profile.

PMMA provides a very poor mask for RIE due to insufficient selectivity against the substrate. RIE tends to etch the entire mask away before the desired etch depth is achieved on the substrate. We attempted RIE with a Zeon Chemicals' ZEP520A mask, which is another polymer. Several attempts at using fluorinated gases failed to etch deep enough, and appeared to saturate at around 100nm of etching. This may be due to polymerization of the capping layer with compounds from the plasma.

An attempt was made to use the proper gas chemistry at a facility at Clemson University, but this did not work out either, as we were already running low on samples. We brought several samples with larger features to test the etch first, with

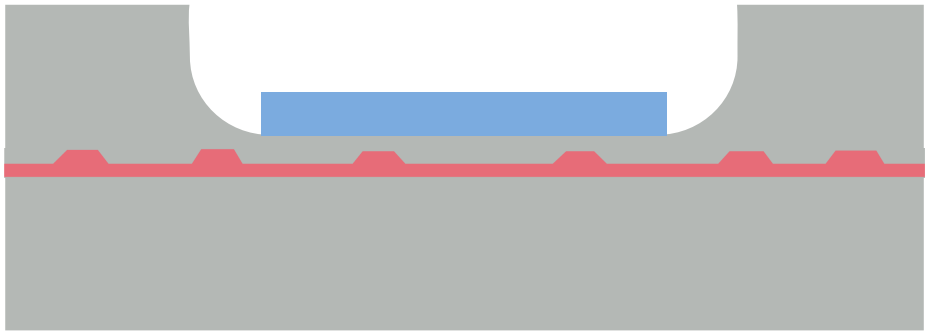

Figure 3.2 A perfectly isotropic etch profile leads to various problems with the device. The thinning of the capping layer above the dots just next to the silver can possibly weaken their confinement. The lack of proper sidewalls also severely limits the possible resolution of the etched features. To get a good etch profile with vertical sidewalls, anisotropic etching must be used.

the goal of quickly using their profilometer to measure the etch rate. However there is an effect called micro-loading, where the plasma can saturate depending on the dimensions of the feature being etched, resulting in an etch rate depending on feature size. Using the assumption of equal etch rates which we measured for larger features to etch the smaller pattern resulted in insufficient etch depth. Properly measuring the etch rate would require fabrication of a large number of identical patterns, and using proper topography techniques to accurately measure the etch rate. The profilometer needle is too big to fit the 1 micron sized features in our pattern. AFM is also tricky on polymer resists due to the stickiness.

3.1.4 Thin film deposition

Plasmonic structures were created by thermal deposition of silver at ultra high vacuum. The sample was loaded into a chamber which was pumped to approximately 2 μTorr. A tungsten boat loaded with silver pellets was fastened between two electrodes. A current of 130A ran through the boat by applying a 20 V potential across it. The Ag evaporated onto the sample at a rate of 15 Å/s until a thickness of 100 nm was achieved.

The sample was then removed from the deposition chamber for the liftoff procedure. Sonication in acetone, followed by another IPA rinse and N_2 dry removed the PMMA film with the silver still attached on top of it, leaving only the silver slabs in the trenches of the pattern formed by the previous etch.

To complete the gate we deposited another thin film of chromium. This layer must be very thin to remain semi-transparent in order to allow optical probing inside the sample. Deposition proceeded at 0.2 Å/s until a thickness of 5 nm was achieved. Cr makes a Schottky contact with GaAs with a barrier height of about 0.41 eV, thus completing the Schottky diode structure. In order to avoid excessive oxidation it is important that liftoff and deposition of the final Cr layer proceed immediately

following the silver deposition. The Cr forms a seal which should prevent further oxidation of the silver.

3.1.5 Bonding the sample

After the completion of the fabrication process, the sample must be attached to a chip carrier. Silver paste dissolved in toluene can form a quality Ohmic contact on the bottom surface, which is already conductive due to the excessive doping. Better contact can be formed by first melting Indium across the bottom surface of the sample. However I found this was not necessary. It's only effect seemed to be a compression of the range of bias voltages needed to span the space of emitting exciton states. Without the Indium however, the necessary range of voltages was not excessive. A reverse bias between 2-3 V was sufficient to stop PL emission.

Ideally, wire bonding to the Cr on the top surface will provide an electrode connected to the Schottky contact on the top surface of the sample. I found it is often very difficult to get the thin gold wires which I used to stick to such a thin Cr layer. Sometimes I had to resort to placing a small spot of silver paste on the top surface and then manually insert the wire into the paste with tweezers. In this case, it is very important that the paste does not spill into the etched pattern, or it can short out the diode, ruining any bias control.

In either case, both electrodes should be tested for contact before proceeding. Sometimes wires that looked perfectly connected to their pads showed infinite resistance, so the bond was broken somewhere even though it was not visible. Testing the bottom contact is straightforward. The bottom surface of the chip carrier and the chosen electrode to which it is bonded should be easily measurable with a standard multimeter. The top surface is trickier, but it should have a measurable finite resistance also.

At room temperature, thermal noise in the PL spectrum can wash out the signal

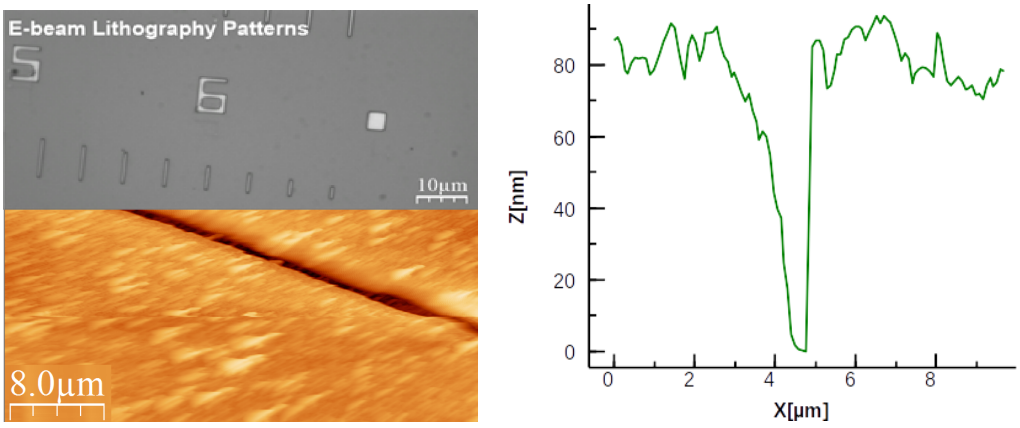

Figure 3.3 *Top Left* An optical micrograph of the completed sample showing the embedded silver structures. *Bottom Left* An AFM scan of the topography of one of the trenches. *Right* A cross section of the topography verifying an approximate depth of 80nm.

from the QDs making characterization very difficult. To ameliorate this effect, we cooled the sample in a Montana Instruments Cryostation closed-loop cold finger cryostat to a temperature of 4K. This cryostat has transparent windows allowing optical probing of the sample. The electrodes gating the sample were attached to one of the internal voltage sources of a Stanford SR830 lock-in amplifier.

3.2 Confocal micro PL experimental setup

In this section I will describe the optical setup of our experiment. We performed photoluminescence characterizations of the sample with two different energies, one above and one below the low temperature band gap of GaAs. The results of these experiments will be discussed in the following two chapters.

3.2.1 Optical setup

Our source for both experiments was a fiber coupled CW laser. The laser first passed through a filter to remove extraneous noise and ensure excitation under a narrow frequency band. Especially important is the elimination of any frequency components in the range of the QD emission, which may be mistaken for signal. A short pass filter is therefore sufficient as well.

Downstream, a pair of linear polarizing films allowed us to adjust the polarization of the incident beam. Between them we placed a half waveplate ($\lambda/2$) which rotates the beam polarization. This setup gave us control of the beam intensity by aligning or separating the beam's polarization from the orientation of the second polarization filter. This trio of optical devices gave us, in addition to the electrical gate bias, two additional degrees of freedom in the experiment, the laser probe's incident power and polarization.

The laser was focused onto the sample with a Mitutoyo infinity corrected NIR 50x microscope objective with a numerical aperture of 0.42 and a working distance

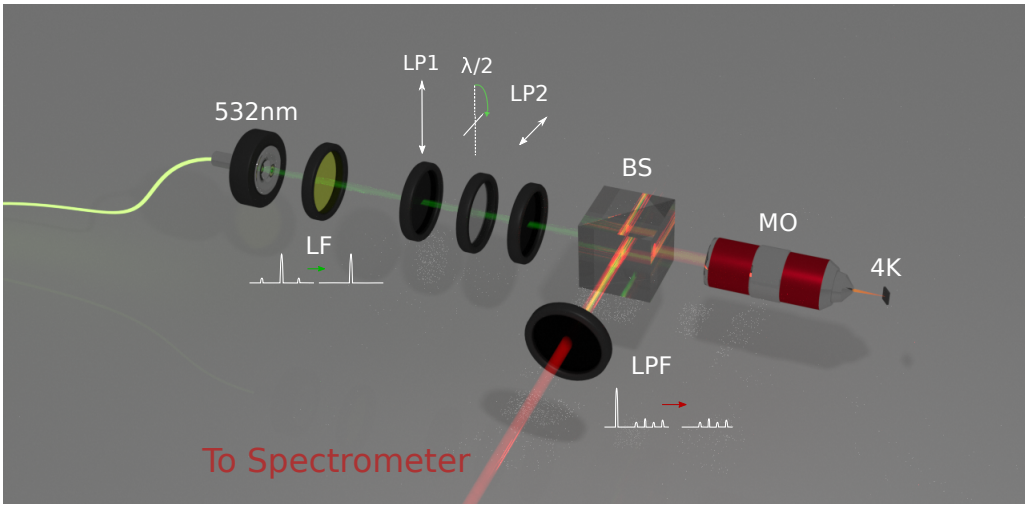

Figure 3.4 A 3D model of the confocal photoluminescence microscopy setup. The fiber coupled laser beam passes through a collimator, line filter, linear polarizer 1, half waveplate, linear polarizer 2, beam splitter, and finally through a microscope objective focusing onto the sample inside the cryostat which is cooled to a temperature of 4K. The signal is collected by the same objective and split off by the beam splitter before filtering out the incident beam. The remaining signal is passed to a spectrometer and CCD for analysis (not shown).

of 17mm. The objective is mounted on an assembly consisting of three linear stages with a set of three 0.5" metallic mirrors all set at 45 degrees to the direction of the beam's incidence upon them, redirecting it at right angles. This assembly gives us the ability to pan the beam spot across the surface of the sample while maintaining focus and normal incidence.

The beam was focused to a spot on the order of a micron. The resolving power of the objective is quoted at 0.7 microns. Photons incident on the QD layer excite electrons out of the QD valence band. Their destination depends on the energy of the incident photons. For photons with energies below the band gap of GaAs, the electron can only be excited into the QD conduction band, and excitons will form. For photons with energies above the band gap of GaAs, the situation is more complex. Electrons can be excited well into the continuum where they are no longer confined by the dot. In this case, there is also an absorption of the beam by the encapsulating GaAs, which injects large numbers of carriers there as well. This leads to the formation of electron and hole plasmas inside the wafer, with complex interactions. However electrons do still relax to lower energy states becoming trapped inside the dot. Again they form excitons with the other holes trapped there.

As the density of QDs in the sample is such that even a small spot of this size tends to excite multiple dots, the detailed analysis of the energy landscape of individual dots presents an arduous undertaking. A PL spectrum taken at one location with a micron sized beam spot can show a large number of peaks corresponding to all the dots being excited during the same time period over which the signal is integrated. Nevertheless we were able to distinguish charge state transitions within single dots with this configuration. We were able to do this because of the sharp transition in PL energy which occurs when the applied bias changes enough to alter the exciton charge species forming there. Comparing this shift in PL energy, corresponding to a change in the binding energy of the carriers in the exciton, to previous work mapping

out the states in these kinds of dots gave us strong evidence that we were seeing a single dot change its charge state, and not two separate dots.

The NIR signal emitted by the QDs was collected by the same objective and split off with a non-polarizing beamsplitter. A 900nm long pass filter eliminated any remaining laser light and other higher frequency noise from the sample. See figure 3.4. The signal was passed to a 1m spectrometer where it was spectrally resolved with a 1200 grooves/mm grating onto a CCD. The signal was integrated over each column of pixels in full vertical binning mode. This setup was able to achieve an approximate spectral resolution of 0.1meV.

All data presented in this thesis were taken under the following conditions. The width of the slit on the spectrometer opening was set to 0.1 (angular units). The signal was spectrally resolved with the 1200 grooves/mm grating in the spectrometer. The Andor Newton CCD which converted the PL signal to electrical data was cooled to -70°C. Full vertical binning mode was used. The integration time was always 5 seconds, which is much longer than the recombination lifetime of these types of QDs, on the order of 1ns.

3.2.2 Polarization dependence

In order to define the two polarizations, TE and TM, we must first set the plane of reference. The silver structures are most extended along one particular axis. The plane of reference is the cross-sectional plane defined by its normal vector which points along this direction. With this definition, TE will mean light polarized with the electric field oscillating along the length of the structures, and TM will be light polarized such that its electric field oscillates perpendicular to this, parallel to the structure's shorter top surface axis. See figure 3.5. The laser spot, being of a size on the order of the width of the silver structures, will extend slightly past the sides of the silver structures. It will thus be able to couple to SPP modes running down this

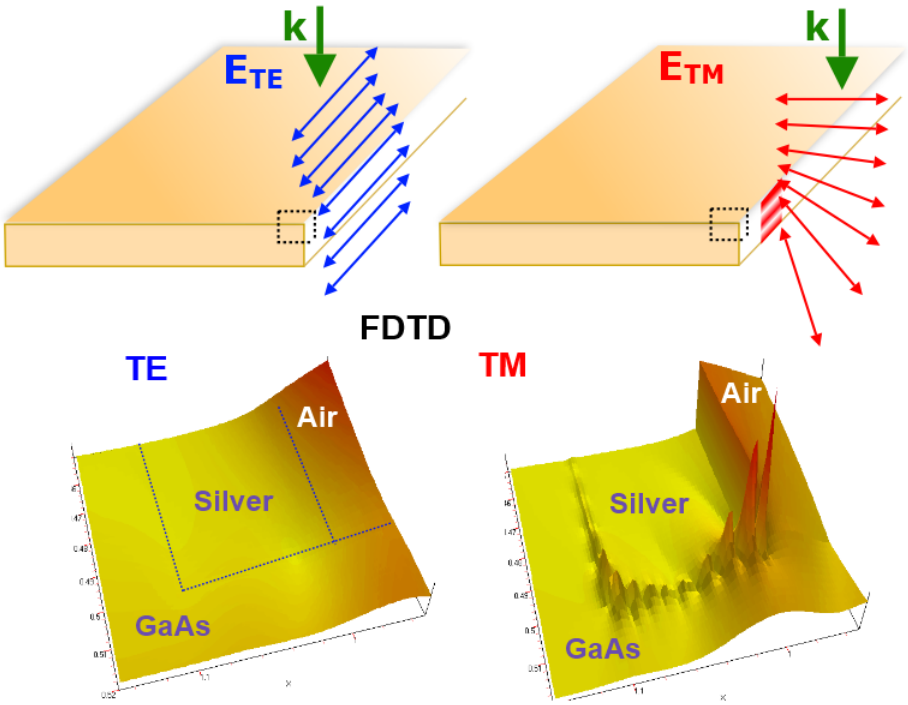

Figure 3.5 *Top* Sketch of the effects of incident polarization. We expected TM polarized excitation, when done on the silver, to also launch SPPs down the side of the silver structures. The corner of the film causes some dispersion and allows the phase matching condition necessary to launch SPPs. *Bottom* FDTD simulations confirm that large electric fields near the surface of the silver are expected for TM polarization, but not TE.

edge, but if and only if the light is polarized in the TM configuration.

Figure 3.5 shows the anticipated effect of the silver slabs upon beam incidence. When the laser beam is in the TE polarization, the electric field lines run parallel to the long axis of the metal surface, transverse to the cross-sectional plane of symmetry. In this case the electric field tends to simply diffract around the edge of the silver with little effect. Any SPPs launched in this configuration due to the coupling of the incident light to the inherent surface roughness of the top surface of the silver must launch along that surface, so the SPP field would point away from the dots and should not effect the QD PL emission.

On the other hand, when the laser shines upon the silver in the TM configuration the electric field lines run perpendicular to the shorter length of the top surface of the silver, and diffraction tends to rotate the field lines as the light passes around the top corner of the silver. This allows the phase matching condition necessary for the launching of SPP waves along the side of the silver film. The bottom of figure 3.5 shows an FDTD simulation confirming this hypothesis. The SPP modes greatly enhance the electric fields at the surface of the silver, with the wave bending around and under the silver structure as well. These strong fields, extending in the direction of the QD layer, and having large gradients, can couple to the dots. The carriers forming the exciton inside the quantum dot will respond to ambient fields by reconfiguring the electron and hole wavefunctions. This can alter the dipole moment and binding energy of the exciton, which would alter their PL emission characteristics.

The effects of the coupling between the SPP waves and the excitons in the QDs should manifest as a polarization dependence in the PL signal collected from dots near the silver, as only one polarization produces these extra ambient fields. This idea is the main topic of this thesis. Since the QDs are axially symmetric we do not expect other polarization dependent effects due to their shape. A QD which is oblong would have different dipole moment magnitudes when oriented along different

axes due to the anisotropic confinement. This would cause different exciton binding energies, and thus a doublet splitting in the PL emission spectrum of a single dot. The symmetry of these dots is such that any such splitting is well below the spectral resolution we are capable of observing, and such an effect will not be observed. There may be a difference in the diffracted field intensity due to the polarization dependence of diffracted beam intensities around the silver. This will be discussed in the following chapters.

3.3 Chapter Review

In this chapter I detailed the fabrication process from the point which I started, which is the MBE grown self-assembled QDs given to us by workers at NRL. The process I embarked on included lithographically defining microscopic features, etching those features to reduce the QD capping layer, implanting silver structures to support SPP modes, liftoff of the PMMA mask, and finally deposition of a semi-transparent chromium layer to supply a Schottky contact for internal field manipulation. I tried to provide additional details for future students to explain why we made the choices we did, and point out any pitfalls which they should be aware of in case they run into similar issues.

After this I detailed the experimental setup for collecting photoluminescence data from this hybrid device. This included cooling the sample in the cryostat and optically addressing it with a microscope objective. Signal was collected back through the same objective and sent through a beam splitter before being filtered and spectrally resolved. Additional polarizers and a half waveplate offer control over two tunable experimental factors, incident polarization and power. This setup is relatively straightforward. Future studies in this work involving time domain resolution will involve more detailed setups.

Chapter 4

Above band gap PL characterization

In this chapter I will discuss the results of characterization of the sample with a green 532nm fiber coupled CW laser using the PL experimental setup described in the previous chapter. The choice of excitation wavelength so far below the wavelength of the near-infrared (NIR) emitting QDs allows us to easily filter the incident beam from the signal and isolate the QD signal from any background coming from the incident beam.

The energy of 532nm photons is about 2.33 eV. This is well above the low temperature GaAs bandgap, which is about 1.52 eV. The light therefore tends to be absorbed into the GaAs capping layer, exciting a large numbers of carriers up into the continuum of the GaAs conduction band. This introduces additional complexity in the microscopic exciton formation and recombination dynamics. Essentially we are dealing with a many body problem involving multiple scattering processes.

The carrier dynamics in the photoluminescence process can already be quite complex. In cases where the excitation frequency is far above the resonance of the QD exciton, it is not as simple as electrons jumping up to the conduction band of the QD and falling back down to the valence band. The excited electrons are pushed well into the continuum and must first relax non-radiatively to be trapped by the InGaAs dot, before relaxing to its lowest unoccupied state, where it can then enter the bound state of other trapped carriers. With above band gap excitation there are large numbers of excited carriers, so at the microscopic level the problem quickly becomes intractable.

Even when excitation is on-resonance, there can be multiple relaxation pathways,

some of which may be and some may not be radiative, so the picture of simple photon absorption and re-emission is deceptively simplistic. On-resonance excitation also requires more complex time-domain spectroscopy experiments, since a CW laser source operating at the same energy as the QD transitions would completely drown out any signal. In this experiment, however, this was not a problem, and we were able to resolve individual exciton states and observe bias dependent transitions between charge species when exciting on the silver.

4.1 532nm CW laser micro PL spectrum

We first began by collecting simple PL spectra from the quantum dots, both on and away from the silver structures, changing only the polarization, while holding other parameters like incident power and applied bias fixed. The goal was to observe any change in the PL spectrum due to the presence of the silver slabs, and we found these changes to be significant. We collected PL spectra for both TE and TM polarizations to observe what effects may arise due to the launching of SPPs along the sides of the silver structures, an effect which is polarization dependent. This was repeated away from the silver to confirm that indeed the dots exhibit no polarization dependence of their own due to their axial symmetry.

As mentioned, above band gap excitation injects large numbers of carriers into the conduction band of the surrounding material, altering the conductivity and carrier interactions inside the wafer. Dense electron and hole plasmas have complex interactions, so we are not able to model the microscopic dynamics leading to exciton formation in the InGaAs cores with this setup. Due to the thick capping layer, the situation is the worst away from the silver structures where the QD signal is significantly broadened and washed out, almost completely lost in the background. However, when exciting on the silver structures the PL signal is much improved, and we were able to isolate single exciton charge states.

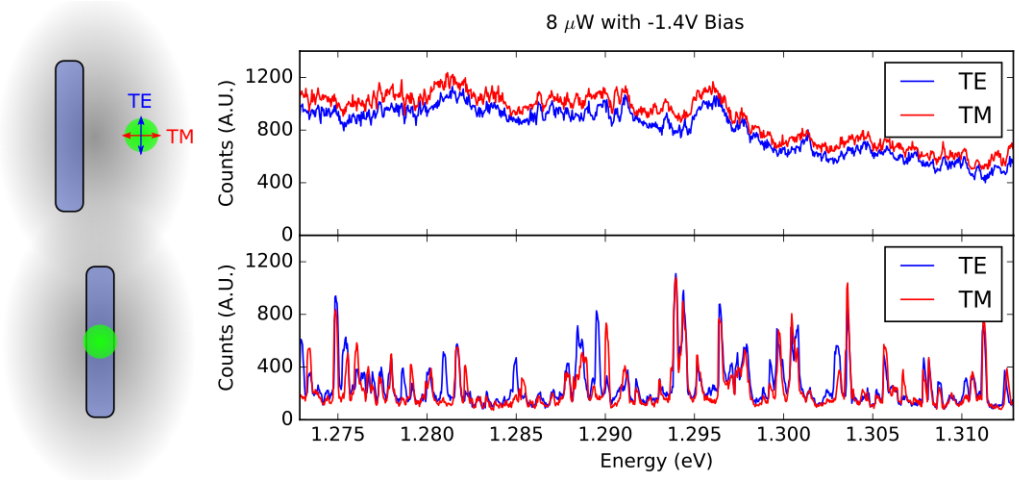

Figure 4.1 The effect of the metal structure on the PL signal of the QDs. *(Top)* Away from the silver. The QD signal is washed out and barely visible when exciting through the entire capping layer. The difference between the polarization is due to a slight power mismatch from unstable laser operation. The shapes are nearly identical. *(Bottom)* Exciting on the silver. This produces clear bright peaks exhibiting the discrete nature of QD states. There is also a clear polarization difference in some of these peaks due to launching of SPPs along the side of the silver film.

Figure 4.1 shows how different the typical QD spectra look when the dots are excited away from (top) and on (bottom) the silver structures with the green laser. When shining away from the silver, it is difficult to discern any QD signal at all. In contrast, the signal from the excitation on the silver shows clear discrete emitting states, typical of exciton recombination in QDs, although still slightly broadened when compared to the below bandgap excitation which will be discussed in the next chapter. This dramatic difference in PL response arising from the choice of excitation location is likely due to the difference in thickness of the capping layer. Away from the silver, the light must pass through the full 280nm i-GaAs capping layer, which absorbs more light there and injects more carriers into the plasmas before light can even reach the dot layer. Beneath the silver, only 100nm of GaAs remains before the light reaches the QD layer, and therefore fewer carriers are expected to be present overall.

Another effect which, under proper conditions, can cause an increase in QD PL signal is an enhanced radiative recombination rate due to the alteration of the local density of states arising from the introduction of nearby plasmonic modes, which provide additional relaxation mechanisms. However, the type of PL enhancement typically occurs when the dots are deep in the range of the SPP fields. At a distance of 100nm from the silver to the QDs this is unlikely to be the case [75]. The peak number of counts are not drastically different in either case. The most noticeable difference between the two graphs is the extreme narrowing of the QD peaks when exciting on the silver. Since this happens under excitation with both TE and TM polarization, this effect cannot be due to the launching of local SPPs on the silver film.

We also see, when exciting on the silver, there is also a distinct polarization dependence, which is not observed when exciting away from the silver. As previously mentioned, the dots are largely axially symmetric and any splitting due to the break-

ing of this symmetry is expected to be well beneath our spectral resolution. The symmetry breaking factors must arise from the etch profile and the silver, specifically from the excitation of local plasmonic fields upon excitation by light in the TM polarization. There is a small polarization dependence in the upper graph (away from the silver), but this is a result of slightly unstable operation of the laser running at a power which is lower than what it was designed for, and possibly sub-optimal coupling of the laser into the single mode fiber we used. The overall shapes are almost exactly the same. This is not the case with the signal collected from excitation directly on the silver. In that case, there are clearly peaks with dramatically more signal in one polarization than the other and some which appear to have shifted in their emission energy. In reality, this is not due to an energy shift of the same state, but the same dot has changed its emitting exciton charge species, as we will see. The different charge species have different binding energies, as extra local carriers affect the local binding potential. This causes the light to emit at different wavelengths when the exciton recombines.

We also wanted to investigate other polarization dependent effects to have more control data for comparison. The PL data which we had already taken away from the etched features (figure 4.1 top) provided us with an idea of how the dots behave without altering the capping layer, and without the effects of nearby plasmonic modes. However, it does not tell us about the effects induced by the change in the wafer geometry due to the introduction of the etched groove structure itself. Diffraction tends to be polarization dependent, so the possibility arises for polarization dependent photon injection into the sample, which would of course lead to polarization dependent signal.

In order to investigate this, we fabricated another sample in which some of the grooves were not filled with silver. While the grooves did not have the silver film, the sample was still coated with a few nm of Cr to produce a Schottky contact. The

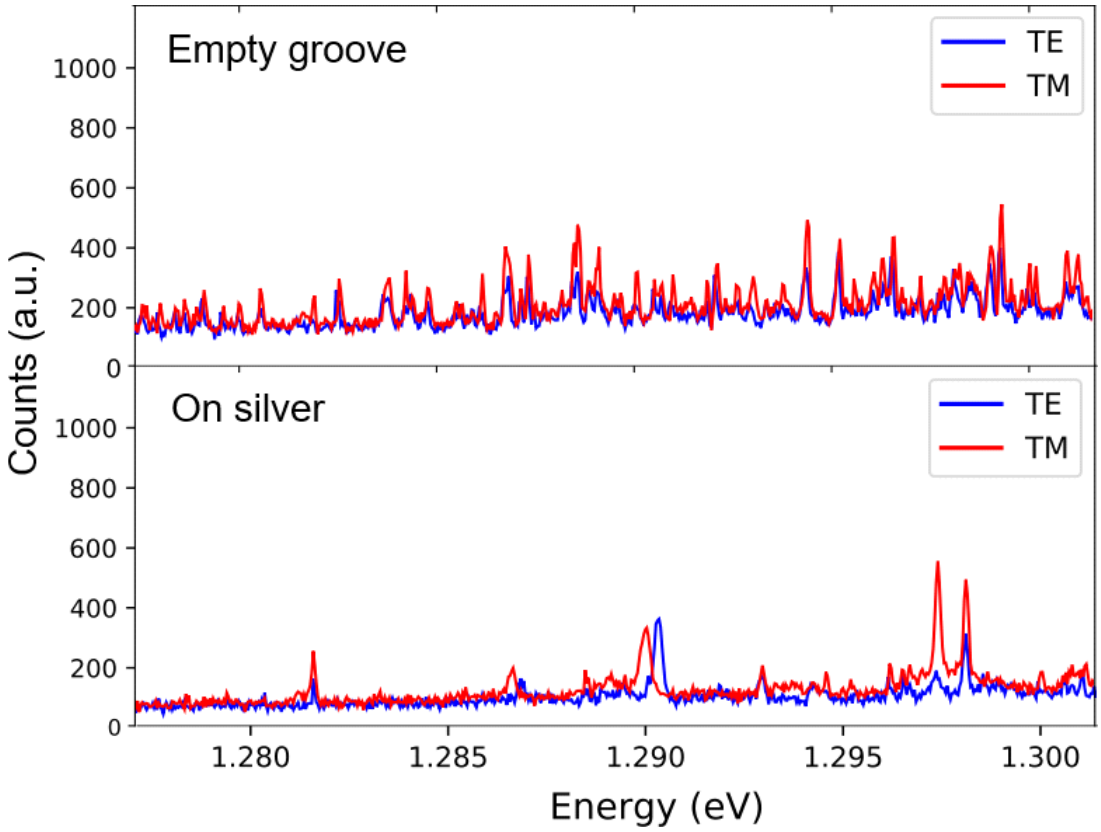

Figure 4.2 PL taken from another sample with empty grooves. The nominally empty grooves do still contain a thin Cr layer. Although they exhibit some degree of polarization dependence, only the silver structures create the drastic polarization dependent shifts in the energy of the emitting states, which we therefore attribute to the launching of local SPPs in the vicinity of the QDs.

alternative was to lithographically define the structures, etch the capping layer, and then produce a 2nd mask, aligned with the already defined structures, to block the evaporation of Cr into the them. We decided this would prove too formidable a task to accomplish in a reasonable time period, especially with the equipment which was readily available for our use. The grooves thus were fabricated with no silver, but did contain a small amount of chromium embedded in them. Even with the absence of the 100nm of Ag, it may be possible that this thin Cr layer could also lead to local launching of SPPs in the chromium, which might have effects on the PL spectrum, so this sample was not ideal for our intended purposes. Nevertheless we found a clear difference between the grooves with silver and those without, as shown in figure 4.2.

The results show a slight dependence on polarization when exciting on the nominally empty grooves, with TM polarization tending to produce slightly more signal. Note that there do not appear to be any peaks which have shifted their energy. The only difference is in the intensity of the emitted signal. This effect may be due to plasmonic modes in the Cr, or diffraction related effects may prefer to transmit one type of polarization more than the other due to the shape of the groove. However, given the consistent background level between the two polarizations this seems unlikely. Surface roughness induced during the etch procedure could also be a contributing factor to both diffraction and plasmonic effects. In any case, the difference between the signal from the empty grooves and the silver filled grooves is unmistakable. Only the Ag filled structures show the dramatic shift in PL energy for some particular states.

We therefore must conclude that the energy shifts, which we see when exciting the sample over the silver structures, are primarily due to the launching of SPPs in the silver films, and do not arise from any other symmetry breaking factor. Furthermore the reduction in signal which we observe appears to arise from the reduced thickness in the GaAs capping layer, which tends to absorb the incident light and inject carriers

into its continuum of states. The next step in the investigation of this sample was to observe the effects of changing the other parameters of the experiment on the PL signal.

4.2 PL dependence on applied bias

To further investigate the PL emission characteristics, and the effect of the local SPP fields, we obtained PL data as a function of the external bias applied across the sample. The electrical gate across the wafer, comprising the silver paste Ohmic contact with the N+ GaAs base on the bottom and the semi-transparent chromium/i-GaAs Schottky contact on the top of the wafer, gives us this method of control, allowing us to apply an electric field through the sample and change the exciton charge species which are confined in the QD. This effect occurs due to band bending of the conduction band towards (or away from) the Fermi level, resulting in confinement of extra (or fewer) electrons in the dots. These types of MBE QDs can be engineered to favor certain charge configurations by careful placement of the dot layer in the diffusion region. A thicker buffer layer places the InGaAs further along the sloping bands and brings the Fermi level closer to the valence band than the conduction band, producing more positively charged excitons. This particular sample used only a 40nm buffer. It therefore tends to produce more negatively charged excitons. See section 2.4.2 for more details.

The PL data is now presented as a function of two variables, emitted photon energy and applied bias. Each data set was also collected at different incident powers and of course for both TE and TM polarizations, to infer SPP induced effects. Data are represented as color maps with emitted photon energy on the horizontal axis and applied bias along the vertical axis. The picture can be thought of as a collection of rows of pixels, where each row is a single PL spectrum at a fixed voltage, e.g. what we saw in figure 4.1. The height of each pixel is mapped to a particular color. In general,

the brighter the pixel, the more counts present. Thus bright lines represent the path of a particular emitting peak over a range of voltages, and dark areas represent background areas with little signal. The peaks are not perfectly aligned with the vertical axis. They tend to drift as the voltage progresses. This is due to a linear Stark shift, changing the exciton dipole charge separation, and therefore the exciton binding energy and emission energy, as the field strength changes.

The range of voltages over which each individual species tends to form in a particular dot are largely disjointed. In other words, given a particular dot, each individual charge species tends to emit from only its own range of applied voltages, where no other species will form for that particular dot. However, this transition will occur at different voltages for different dots and charge states, as it depends on the shape and size of the dot and the confining potential. There are small regions of overlap as the binding energy shifts over to the new state, but the distinction between the different states is clear.

Figure 4.3 shows the PL spectrum at a particular excitation location on the silver as a function of applied bias, for both TE and TM polarization, and for two different beam powers, $3\mu W$ and $15\mu W$. We see in this data the characteristic signal of a transition between two different exciton species, probably X^{-1} and X^{-2}. A more detailed study would have to be performed to confirm the exact charge states, so we will simply call them $X1$ and $X2$. However the exact details are not relevant in this case. The important point is that the uniformity in the signal intensity between the two states and the characteristic transitional behavior is strong evidence that they are in fact two different charge states emitting from the same dot.

Of particular note is the polarization dependence of the magnitude of the necessary applied bias to force the exciton charge species transition to occur. At $3\mu W$ this transition happens at an approximate bias of -0.3V for the TE polarization, while for TM polarized excitation a -0.5V applied bias is needed. Note that the lines appear

to have shifted downward when the polarization is changed.

We attribute this shift to the effects of the local plasmonic fields generated by the incident TM wave on the silver-GaAs interface, producing large local electric field gradients in the region by launching SPPs down the interface. The plasmonic effect on the system is an induced electrical screening of equivalent to a field which would be produced by an additional 200mV of reverse bias. A similar effect is the power tuning which causes a similar shift downward in the exciton transition voltage. This can be observed in figure 4.3 in the shift downward of the same transition between the two different powers with polarization fixed. It occurs for both polarizations. This is due to the injection of a larger number of carriers which act to screen the field coming from the applied bias.

Nearby we see many other excitons with much dimmer signals. These are likely coming from dots further away from the silver structure, as the laser spot has a Gaussian profile and its intensity falls off rapidly from the center. The fact that many of these dots do not share the same polarization dependent features and are likely outside of the range of influence of the plasmonic fields gives further evidence that the effects we are seeing on dots nearer to the silver are indeed due to the SPP field. They do however exhibit the power tuning effect as expected.

This effect is perhaps unexpected. The SPP consists of oscillating charges fields. The electric field will change directions over time, and intuition may suggest that the average over time should be 0. Yet what we observe seems to imply a DC field produced by the SPPs. It is possible for materials to produce DC fields as a second order nonlinearity, through the self mixing of a single frequency component. We believe however that what we observe is simply an effect from increased screening of the carrier plasmas by the strong SPP field gradients. We will see in the next chapter that no such DC shift occurs when excitation is performed below the band gap of GaAs.

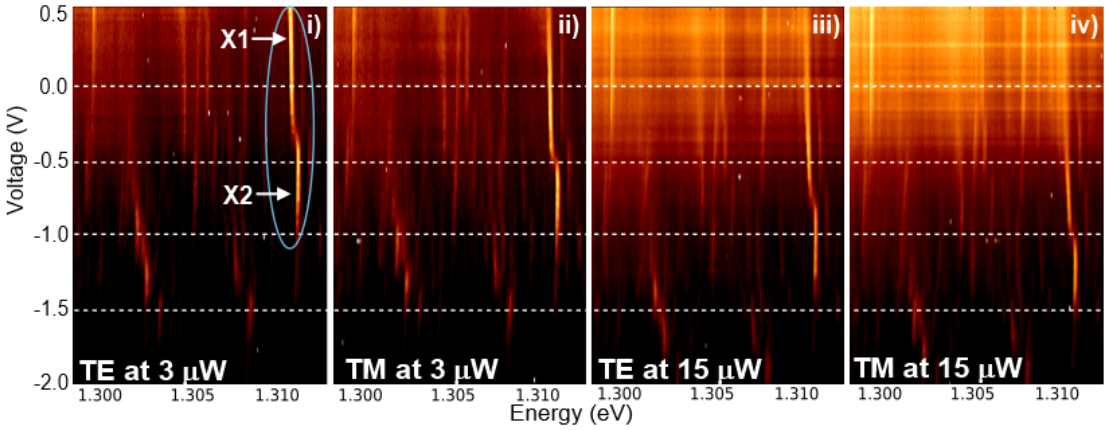

Figure 4.3 Bias dependent PL maps with 532nm excitation. The two states in the blue oval exhibit the characteristic signal of a transition between two charge species within a single dot. This transition occurs at a deeper reverse bias for TM than for TE under the same incident power. This effect is similar to the power tuning effect where a larger reverse bias is required at higher incident powers. This can be seen in the downward shift of the same transition as incident power is changed while holding polarization fixed.

4.3 PL dependence on incident power

We next investigated the PL response of the sample as a function of incident power. As mentioned in the last section, there is an effect dependent on the incident power which is similar to the SPP induced tuning of the applied bias at which the exciton charge state transition occurs. This power tuning effect also causes a similar shift downward in the exciton transition voltage. Intuitively this makes sense, since larger incident powers of high energy photons inject more carriers into the continuum causing a screening effect on the electric field due to the applied bias, thereby requiring a larger externally applied bias to achieve the same internal field and exciton dynamics.

This effect can be seen in figure 4.3 in the difference between the 1st and 3rd plots which both use the same polarization at the same location with different powers. Similarly the 2nd and 4th plot show the same effect with the other polarization. We investigated this effect in more detail at the same location to better understand the power dependence of this transition for each polarization by collecting a PL map as a function of power at a fixed bias of -1V. The results are shown in figure 4.4.

The same exciton species are indicated in the figure. This is an interesting result. Not only does the polarization affect the required bias to effect this transition at a fixed power, but it also affects the required power to cause the same transition at a fixed voltage. Moreover the range of powers over which this transition occurs is stretched out in the case of TE polarization. For TM this transition occurs near 20 μW of incident power, whereas for TE the transition begins around 40 μW but is not fully complete until about 60 μW.

At low powers, the same X2 state is emitting from both polarizations. At high powers, both polarizations emit from the X1 state. The power is high enough to inject carriers that screen out the internal field and drive photo currents through the wafer as the plasmas try to reach equilibrium. However there is an intermediate range of powers, around 30 μW, where the emission is entirely confined to the X2 state for

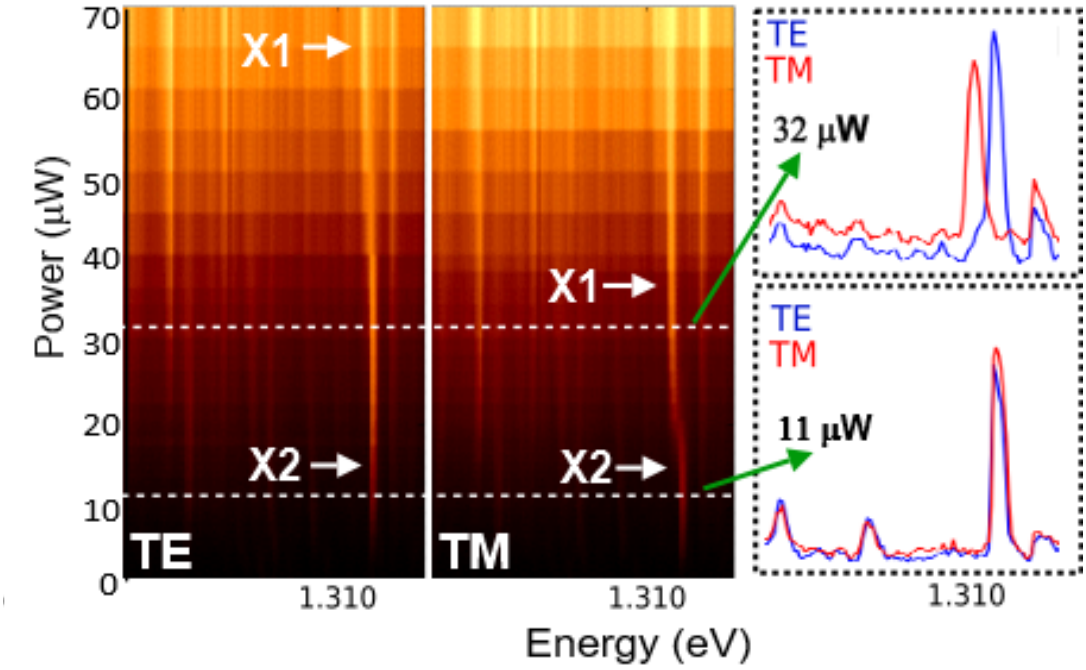

Figure 4.4 The same charge state transition shown in the previous section. The sample is now held at a fixed voltage of -1V as the power is changed. *Left* The same transition is induced via power tuning only. The dependence on polarization is apparent. The transition occurs much sooner for TM polarized excitation than TE. *Right* Two slices show the individual spectra at fixed powers of 11μW and 32μW. At low power, both polarizations produce the X2 type exciton. As power is increased, TM excitation screens out the field first switching the state over to the X1 type exciton, while TE is still emitting the X2 type exciton at the same power. Changes in the emitting state can thus be induced all optically, by changing the polarization.

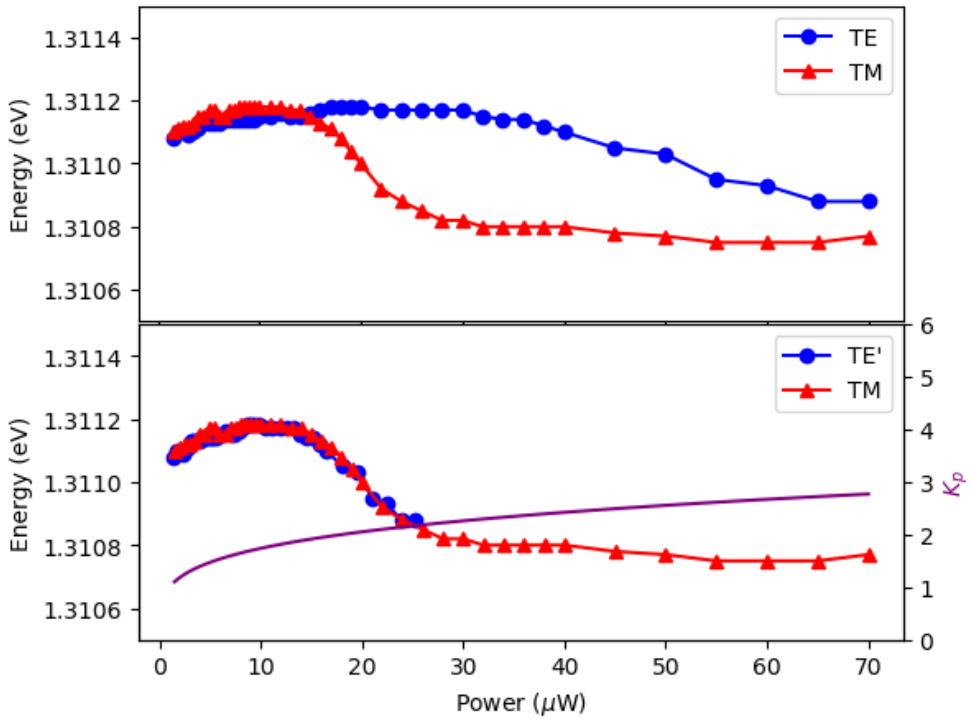

Figure 4.5 *Top* The energy of the X1 and X2 peaks of emission vs. incident power. *Bottom* The same plot with the TE power reduced by a factor of K_p (the purple curve), which is a power function of the abscissa values with exponent 0.76. This shows the apparent power law behavior of these states under the influence of the SPP field.

TE polarization and the X1 state for TM polarization, as shown in the inset in figure 4.4.

This suggests a new switching mechanism for photon sources utilizing these types of emitters, a mechanism which is all optical and might not be constrained by the slow switching speed of electronics. However, we should stress that it is not necessarily the case that this mechanism offers switching on an ultrafast timescale typical with traditional photonic devices, as the diffusion of charge carriers in the material still plays a significant role in the process. Further studies are required in the time domain to investigate this question.

We have also found that the effect of this SPP induced power dependent shift in the emission of these two states appears to follow a power law. In figure 4.5 we plot the central energy of this particular dot vs. incident power for both TE and TM polarizations. When the power of TE is rescaled according to a power law with exponent 0.76, the data appear to overlap. This shows that the power tuning effect is nonlinear, as eventually the level of carriers will be sufficient to completely screen the internal fields. The wafer is essentially metallic at this point. The presence of the local SPP fields allows us to get the same screening effect as power tuning but at much lower powers.

4.4 Summary of results

In this chapter we studied the PL characteristics of the hybrid plasmonic/QD sample, the fabrication of which was thoroughly discussed in the preceding chapter. This chapter focused on excitation with photon energy above the band gap of the encapsulating GaAs. We first noticed the dramatic tightening of the QD peak signal when exciting on the silver vs. away from the silver. This is likely due to the decreased thickness in the capping layer, resulting in fewer carriers being injected into the sample. Away from the silver the thick capping layer injects in too many free charges,

resulting in too many carrier collisions washing out the QD signal.

We then performed PL studies as functions of incident power and applied bias. We found an effect due to the launching of SPPs which acts to screen the internal field. This effect manifests itself in the PL bias maps as a shift in the voltage at which a transitions occurs between different charge states in a single dot. A similar power tuning effect occurs due to the increase in incident power. By combining the two effects, we found it possible to control the exciton charge state optically in a single dot simply by controlling the incident polarization, as the fields are screened at much lower powers in the presence of the SPP field. In the next chapter we will discuss PL characterization of the sample with energy below the GaAs bandgap.

Chapter 5

Below band gap PL characterization

This chapter will focus on the results of the PL characterization of the same hybrid plasmonic/QD device discussed in the previous two chapters, only now with photons of energy less than the GaAs band gap energy, but still of sufficient energy to excite excitons in the InGaAs cores. The experimental setup is identical to the previous chapter except for the change in the excitation source and the replacement of any wavelength dependent optical components, the 532nm laser line filter, the half wave-plate, and linear polarizers. The laser used was an 880nm fiber coupled NIR diode laser, which produced a slightly larger laser spot when focused, but still on the order of a micron.

5.1 880nm PL results

Exciting below the band gap introduces some important differences in the exciton dynamics compared with the 532nm excitation. It allows direct excitation of the QDs without inducing extraneous interband transitions and the resultant injection of large numbers of charge carriers into the surrounding medium. This should and did eliminate the power tuning effect on the charge state transition which we discussed in the previous chapter on above band gap excitation. As this effect was a result of carrier screening, it did not appear in the absence of extra carriers, as expected. Another result of fewer carriers is a much cleaner signal with more narrowly defined peaks. Without such dense electron and hole plasmas causing complex many body scattering interactions, the broadening of the signal which we observed in the last

chapter did not occur. We were able to excite and observe the QD signal through the entire capping layer, with fine peaks observable even outside the range of the plasmonic silver structures.

Although we freed ourselves of the influence of the GaAs carrier background, this did not come without a cost. Photons at a wavelength of 880nm have sufficient energy to excite the QDs. They are also able to excite the wetting layer underneath the dots (see section 2.4.2), which is essentially just an InGaAs quantum well (QW). The signal is therefore sitting atop a large background from the influence of this layer. However, the QW PL is very broadband and thus easily separable from the very narrow QD transitions. We observed only the tail end of this background and estimated it by fitting a simple exponential curve underneath the peaks, as shown in figure 5.1

Again we compared the PL signal when exciting on the regular substrate far away from any silver and when exciting directly onto the silver structures. As in the previous case, we observe almost no difference between the signal when excitation is performed in either the TE or TM configuration, as expected due to the symmetrical shape of the QDs. When we excite on the silver however, we do note a difference between the two polarizations. Here the effect is different than before.

Again, as before, we collected bias dependent PL maps for each polarization. The results are consistent but different than in the case of above band gap excitation. There is a clear dependence on polarization that emerges when we excite on the silver slabs, as expected. However with below band gap excitation, this manifests instead as a reduction in PL intensity in the TM configuration compared to the TE configuration. Note that this is the opposite of the effect we saw when exciting above band on the empty grooves. In that case we also noted a similar effect where one polarization produced consistently brighter peaks, but in that case it was TM producing more signal. Now TE polarized excitation is producing more signal. Also,

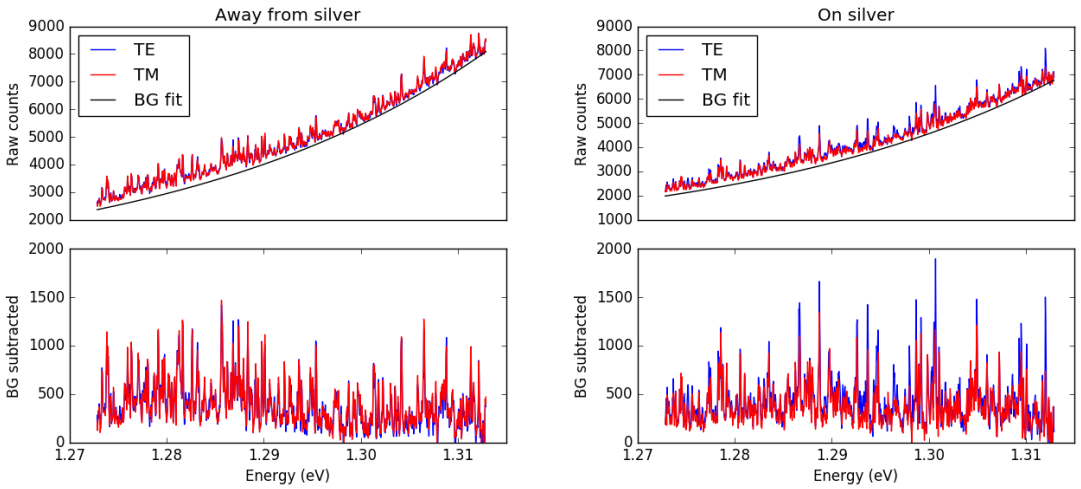

Figure 5.1 *Top left* The typical 880nm PL signal away from the silver structures. *Top Right* The typical 880 PL signal when exciting on the silver *Bottom row* The results after subtracting a simple exponential fit representing the tail end of the quantum well background from the InGaAs wetting layer under the dots.

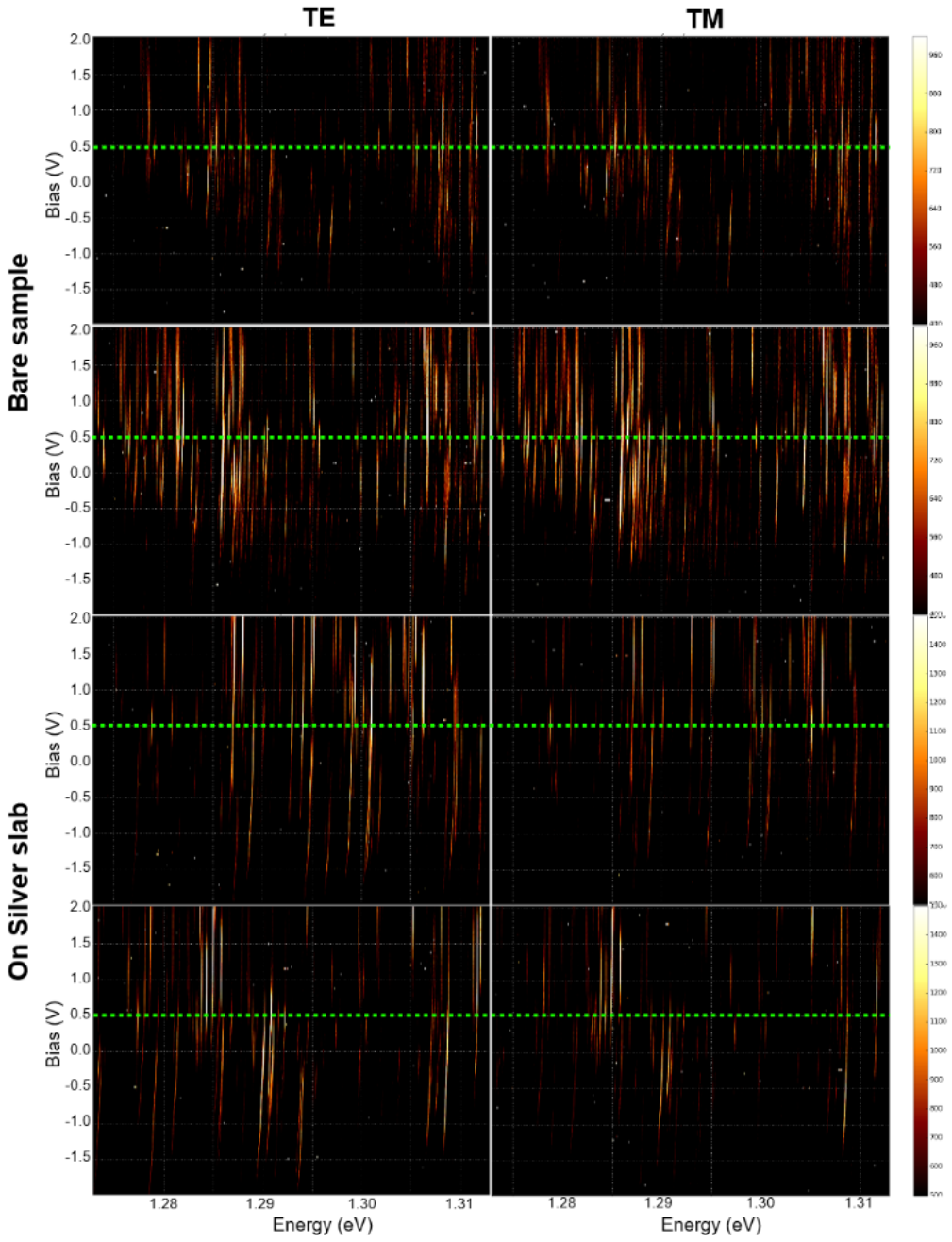

Figure 5.2 A selection of bias dependence PL maps for 880nm excitation, two on the silver, and two away from the silver. The results show the lack of polarization dependence absent the silver, and a reduction in PL signal intensity on the silver for TM compared to TE excitation.

as expected, without the large number of carriers to screen the internal field, there are no noticeable shifts in the transition voltages between exciton charge species. More in depth studies are needed to probe what exactly is going on here, and why TM is producing less signal than TE, but we will discuss this polarization dependence in some depth in the next section.

5.2 Discussion of polarization dependence

We note a marked decrease in the intensity of emitted PL when excited in the TM configuration on the silver structures. When SPPs are also launched in the vicinity of the dots with below band gap excitation, something we did not previously observe happens. We appear to lose signal. This decrease is consistent across the majority of the emitting states. Furthermore, we see from figure 5.1 that the level of background due to the wetting layer excitation is equivalent between the two polarizations.

This polarization dependence is further quantified in figure 5.3. We find that, when exciting the bare sample, the asymmetry between the PL intensities from the two polarizations are centered around 0, with a standard deviation of 0.056, 71.9% of states lying within 1σ and 97.9% of states lying within 2σ (represented by the gray bars). In contrast, when exciting on the silver, there is a clear and significant skew towards TE, an average of 0.141, and a standard deviation of 0.063. Now, using the gray bars we find only 38% of states within 1σ and 59.5% of states within 2σ, where σ is the standard deviation of the data collected away from the silver. Furthermore, we observe that the only states which tend to emit stronger in the TM configuration, i.e. those below the grey bars in the bottom right plot of figure 5.3, also tend to emit weaker, i.e. they are towards the left when plotted against the maximum intensity.

With above band gap excitation we were able to observe the effects of SPP fields on the local carrier environment in the bulk GaAs. Now all carriers are confined to the InGaAs layer, burying deeper in the sample. In this case, the SPP fields are

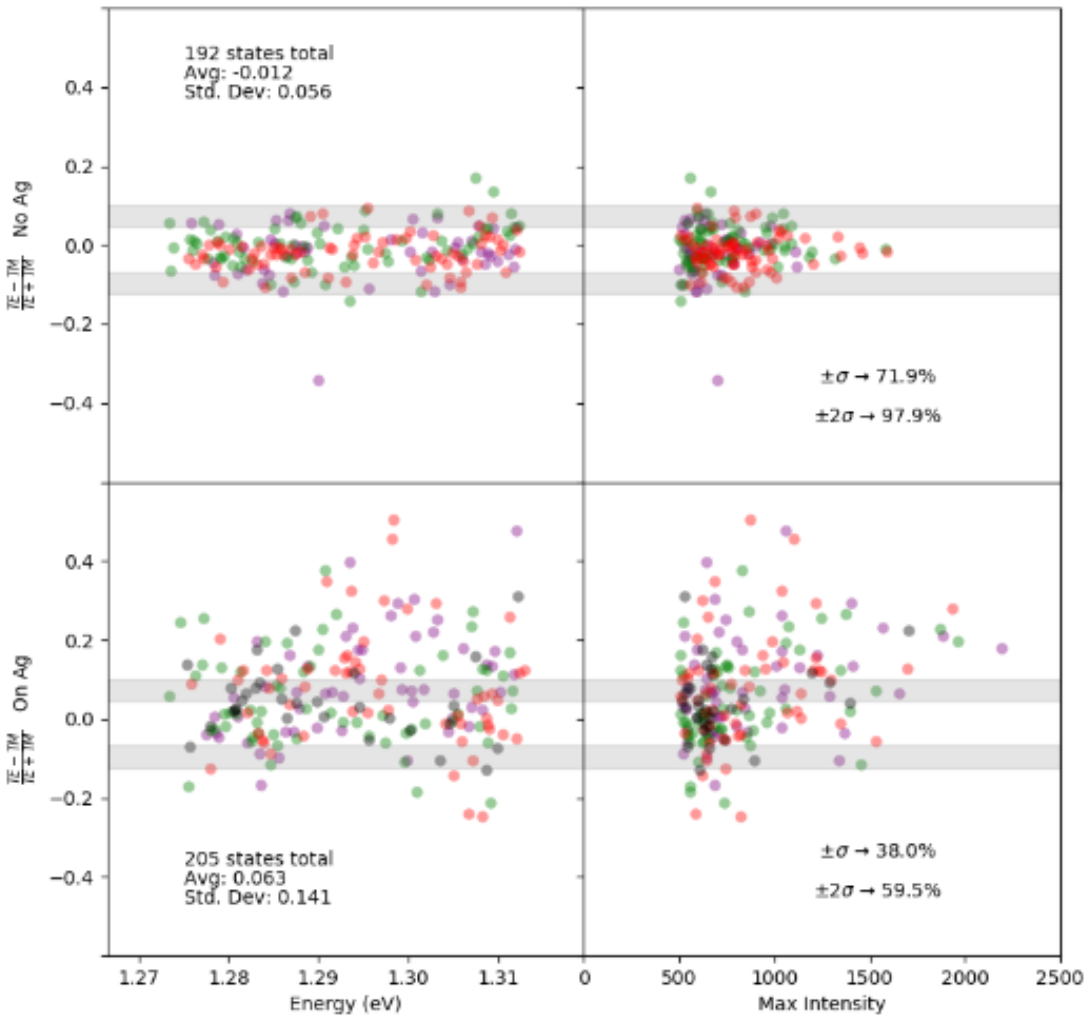

Figure 5.3 The polarization asymmetry of the PL intensity from a large number of states excited both on (*bottom*) and away from (*top*) the silver, shown vs the energy of the peaks (*left*) and the larger value of the two intensities (*right*).

more remote and the effects may be more subtle and difficult to discern. In order to further investigate the polarization dependent effects we are seeing we obtained FDTD simulations of this experiment.

Figure 5.4 shows an FDTD simulation of the diffracted field intensity after a plane wave makes contact with a geometry approximating the silver structures in our sample. In the TM simulation the SPP wave can be seen propagating along the side of the silver slabs and going around the corner underneath the silver as well. The exact shape of the GaAs capping layer etch profile can affect the resulting field intensities somewhat, so there is some uncertainty here. The bottom part of the figure shows cross sections of the field intensity going down from the corner of the silver, and also out away from the silver at a depth which should be coincident with the InGaAs layer. These domains are shown by the white dotted line, which start from the corner of the silver. Of particular note is the large increase in TE intensity in the range 150nm to 400nm away from the edge of the silver structure. This difference peaks at about a 50% increase for TE over TM near 300nm from the edge.

It may be tempting to write off the decreased signal for TM polarization as an effect due to the diffraction of the beam profile around the edges of the silver structure and the resulting larger incident intensity for TE polarized light. It is likely this difference in field intensity plays some effect locally. However, one would expect the wetting layer background to be proportional to the integration of the local field intensities across the beam spot area. Let's consider two possibilities.

In the first case, the TE signal is simply brighter because of higher local intensities across the majority of the beam spot, and this is the only factor. Then we would expect, perhaps certain areas show more intense signal for TM than TE, but overall most of the emitting peaks are taller for TE excitation. This is consistent with figure 5.3. However, once we integrate the local field intensities over the laser spot, this consistently higher TE local field intensity should result in an overall larger wetting

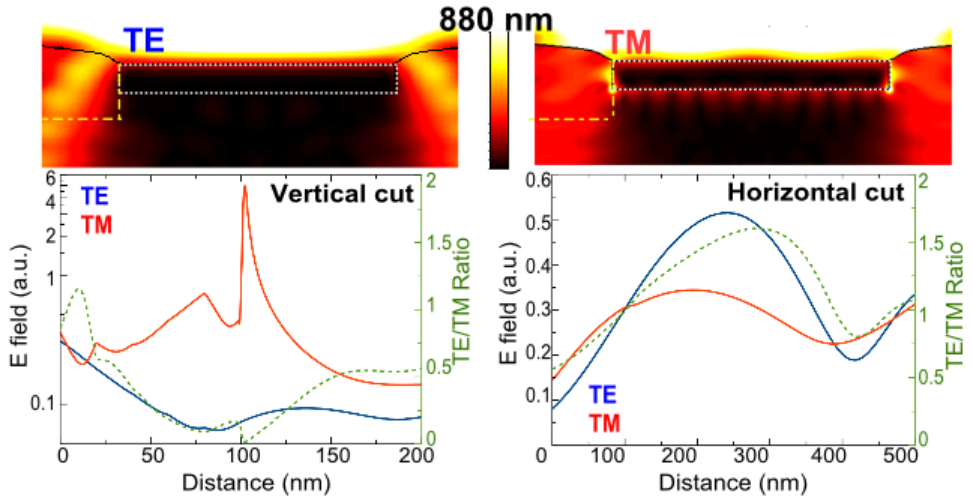

Figure 5.4 *Top* FDTD simulations for the field intensity of TE and TM plane waves diffracting around a rectangular silver slab. The corners of the GaAs have been slightly rounded off. *Bottom* Horizontal and vertical cross sections of the above plots starting from the corner of the silver. The sliced area is shown by the dotted lines in the top graph.

layer background under excitation by TE light. This is not observed in figure 5.1.

In the second case, the TE signal is brighter in some areas and the TM signal is brighter in some areas, but the average integration over the beam spot leads to nearly equal background levels. In this case, then we would expect to see some TE peaks brighter than TM, but also the opposite in roughly equal amounts for those dots in regions where TM field intensities are higher. Thus we should see a spread in the data of figure 5.3, but not a systemic shift overall. But this also is not what we observe.

Since we do see a systemic shift, without a commensurate increase in the wetting layer background, then it casts doubt on the notion that this can be entirely explained by diffraction related effects. What we see is a near universal decrease in the emitted PL intensity for the vast majority of exciton states when excited in the TM configuration, but with a nearly equal wetting layer background. We are led to conclude the following; the decrease in signal under excitation in the TM polarization cannot be entirely explained by a difference in local intensity of the incident field impinging upon the dots due to a polarization dependent change in the diffracted beam profile, but must be in some part due to some other symmetry breaking factor. That symmetry breaking factor is the presence of the SPP field.

The FDTD simulations also make the assumption of an incident plane wave, which may affect the resulting beam intensity profiles. In reality the laser beam spot is approximately Gaussian leading to a sharp attenuation of the intensity away from the edge of the silver. Given that the beam was focused to a spot size on the order of a micron, only slightly larger than the silver structures, it is unclear how a more realistic simulation of the incident light source would affect the field intensity profile at the dot layer.

As one final piece of evidence, we observed a very subtle shift in many of the peaks when exciting on the silver structures. The shift was typically only a single pixel on

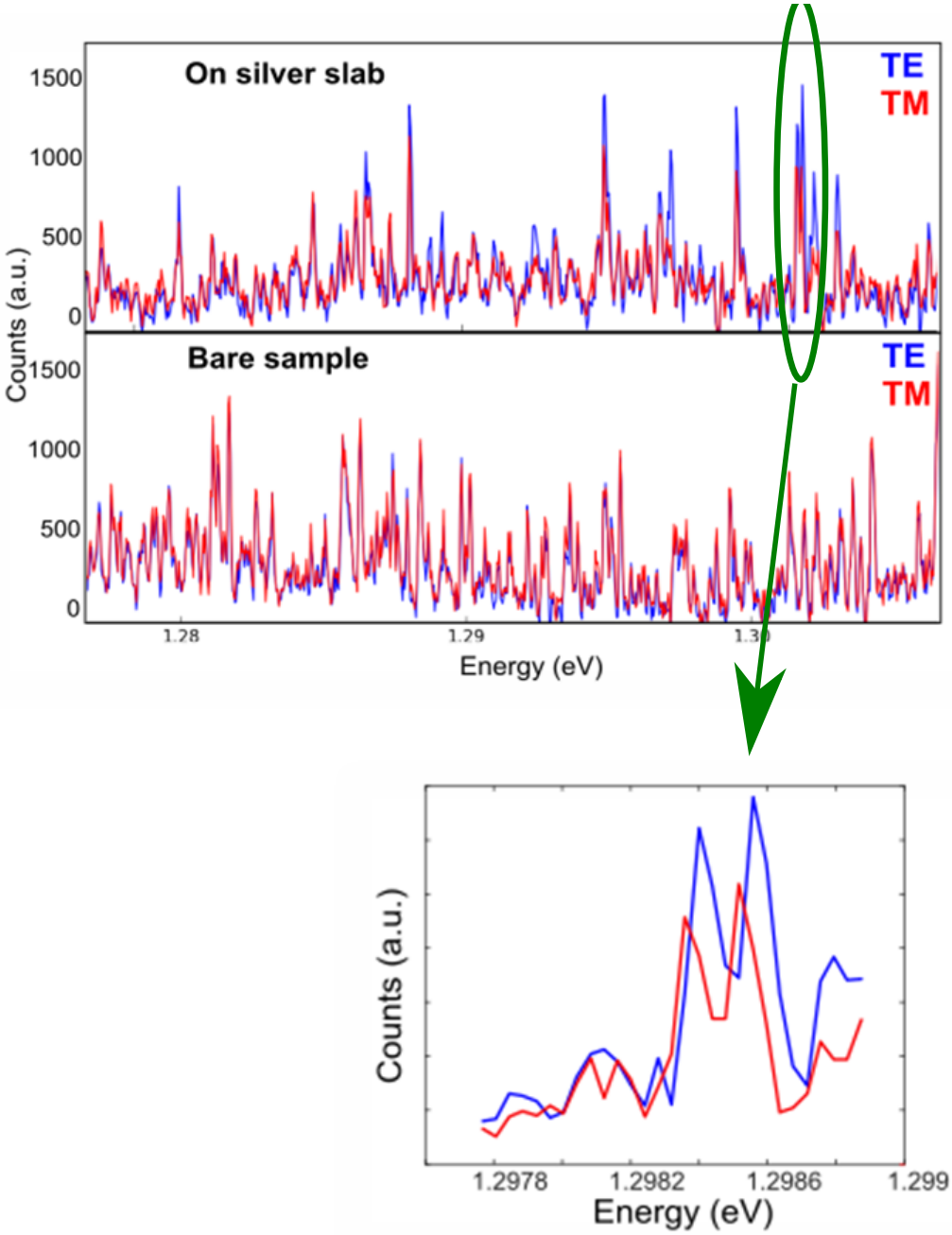

Figure 5.5 Samples of typical PL spectra taken on and away from the silver. *Inset* Zoomed in plot of a couple of the peaks from the excitation on silver. We observed several peaks which appear to have shifted very slightly in their emission energy. Such an effect cannot be explained by a difference in field intensity. Only a change in the internal charge configuration of the dot can cause such a shift.

the CCD, barely within the resolution of our experiment, on the order of 0.1meV. The effect was typically a blueshift in the TE excitation data. These shifts did not appear as often when exciting away from the silver. This effect, if real and not a noisy artifact of our limited resolution, simply cannot be explained by a slight difference in incident beam intensity. A larger intensity simply excites the dot faster, generating more recombination events. It does not change the internal energy of the exciton dipole. Only an effect which alters the charge configuration inside the dot, such as coupling to SPP gradient fields, can explain such a shift. Given our limited spectral resolution, further studies are warranted to investigate this effect more thoroughly for better confirmation. By moving the plasmonic fields closer to the dot layer, this effect may be amplified.

However we do think overall there is strong evidence that the consistently weaker PL signal of the QDs in the TM configuration is due to an effect of the SPP field on the carriers forming the exciton. One possibility is the interaction of the local SPP field with their electric mesoscopic moment. On the atomic scale, QD nanocrystals are not really point-like particles. Due to their extended nature, the point dipole approximation can break down in the presence of strong field gradients [75]. Calculations must consider the coupling between the SPP field and the QD's mesoscopic dipole moment. Phase differences between the dipole coupling terms and terms coupling to higher pole moments can lead to constructive or destructive interferences, changing the outgoing signal intensity.

5.3 Summary of results

We performed similar experiments on the same sample from the last two chapters, changing the excitation source to have energy below the band gap of GaAs. By using a wavelength of 880nm, we avoided the problem of carrier injection and signal broadening which we saw in the last chapter. This also eliminated effects due to the

presence of free carriers which we observed last chapter, such as the power tuning effect and the SPP-induced screening effect. The effects of the SPP fields in this case are more subtle. This is not unexpected since these effects now arise from the direct coupling of charges inside the QDs themselves to the SPP field which is relatively far away. In the previous chapter the SPP field was coupling to much closer carriers in its local dielectric environment, and the effect was more pronounced.

PL data from below band excitation show consistently lower signal when exciting on the silver in the TM configuration compared to the TE configuration. While FDTD simulations appear to explain this effect as a difference in transmitted intensity at first glance, we believe there is good evidence that we are seeing another SPP induced effect on the PL signal. First the wetting layer background is consistent across both polarizations, which would not be expected if the incident intensities were actually different. This error may be due to plane wave assumptions in the simulation. Second we observed tiny shifts in energy, just at the resolution of our experiment, in the emitted PL signal energy. Such an effect cannot be explained by a difference in intensity, but can be explained by charge reconfiguration from coupling to SPP fields.

Chapter 6

Summary and future directions

In this work, we investigated two different types of nanoscale optically active systems, self-assembled semi-conductor quantum dots and SPP supporting plasmonic structures. Specifically we looked at the interactions between the two systems and what happens when they are brought close enough together to influence each other. We found interesting new effects arising from the electromagnetic fields of the SPPs which alter the distribution of carriers inside the QD wafer.

When exciting above the band gap of the encapsulating GaAs, we found a new screening effect induced by the SPP fields. The action of this effect was to reduce the influence of applied fields, requiring larger external biases with SPPs than without them to achieve a similar internal environment. A potential application was suggested, an all optical method of exciton charge state switching, which may or may not be faster than directly appliying fields with electronics.

We also investigated the interaction in the case of below band gap excitation. In this case we found that the effect of the local SPP fields was to reduce the emitting PL signal from the dots. Furthermore, we saw hints of slight energy shifts in the exciton recombination energy, just at the limit of our spectral resolution, which would provide further confirmation that the effects we see arise directly from the SPP fields and not from a polarization dependent diffracted beam field profile. In the future, the coupling between these two types of systems must be well understood for precision engineering of nanophotonic devices utilizing them.

6.1 The future of the technology

This work represents a small step towards a large undertaking, the thorough understanding of the various complex interactions between nanophotonic components, with the aim towards future complex integrated devices. A thorough and deep knowledge must precede any attempts at building practical device prototypes. As technology continues to progress in performance and functionality, so too advances its complexity and the requirement of technical proficiency, and ultimately its cost of fabrication. Even with a valid working prototype design, the economics of mass production may ultimately decide the fate of any new technology. At this point in time, the field is simply too young to precisely predict what its future will look like with any confidence. Ultimately the aim of scientific academic scientific research is to simply gain a better understanding of the structure of nature, and leave the concerns of practicality to the next generation of engineers. But with so much work going into creating fascinating technological devices of the future, like optical cloaking devices, clearly nanophotonics and plasmonics will have a bright future in some capacity.

6.2 Future research directions

The work presented in this thesis can be immediately extended and further verified. Further studies should focus on implanting similar structures closer to the dot layer. We strove to do this but complications due to the lack of proper equipment for dry etching of GaAs have delayed this goal. Future samples will likely have to be taken to specialized facilities for this purpose, although we are awaiting a new sample from NRL with a 100nm capping layer that may permit a similar experiment with the simpler wet etching procedure. The isotropic nature of wet etching prevented us from etching deeper into the thick capping layer without sacrificing the confinement in the immediate area around the silver. With a thinner capping layer, this problem may

be avoided, although at very close proximities to the QDs, even small anisotropies may prove too much.

If we can get closer we expect to verify similar but stronger effects. Verification of the exciton energy shift which we observed with below band gap excitation should be a priority. At very close distances we may see quenching of the PL signal due to tunneling of the carrier out of the dot. There has also been a theoretical prediction of a strong coupling regime at extremely close proximity between the dot and plasmon [76], where the exciton dipole interacts with it's image charge in the plasmonic structure. Verification of this phenomenon would be a major result. One of the ultimate goals is to attempt to couple photons from the plasmonic state back into a QD. If this is possible then perhaps it could allow plasmonic structures to act as waveguides coupling two QDs, or the QDs may act as a gain medium to overcome the inherent lossy plasmonic propagation. Ultimately, a long term goal would be coupling two QDs such that one dot may be excited and transfer it's exciton over to another dot with the SPP acting as a mediator of this exchange.

In order to verify other expected effects which cannot be resolved by relatively simple PL experiments, the time domain should be investigated. Exciton recombination lifetime enhancement immediately comes to mind, as it has been observed in related systems previously [59, 60, 61]. Experimental setup will be more complicated in this case and may involve single photon correlation measurements, wave pulse shaping techniques, and/or pump-probe spectroscopy. These techniques were not used and therefore not discussed in this work, but I'm sure Yanwen would be happy to explain them.

Alternative silver structure shapes can also reshape the plasmonic fields possibly leading to new interesting effects. Sharp corners, e.g. in the bowtie geometry, can lead to very intense near fields. Metal-insulator-metal structures can change the direction of the field lines and also split the plasmonic modes due to the symmetric degeneracy,

possibly affecting the exciton dipole in different ways. It would also be interesting to make small silver nanoparticles whose resonance overlaps with that of the QD.

Another technique for growing similar QDs has been demonstrated which does not self-assemble on top of a wetting layer, but involves fabricating small pits which capture the dot material into nanoparticles [77]. In this method the fabrication can be planned in advance to put emitters in precise locations rather than the randomly distributed the SAQDs we used. The implantation of silver structures in this sample will be much more involved, and extreme care must be taken in order to align the pattern with the pre-existing distribution of dots. Isotropic wet etching simply is not going to cut it here. The fabrication is ultimately the most difficult part of this entire process.

Bibliography

[1] Gordon E. Moore. "Cramming more components onto integrated circuits, Reprinted from Electronics, volume 38, number 8, April 19, 1965, pp.114 ff." In: *IEEE Solid-State Circuits Society Newsletter* 11.3 (Sept. 2006), pp. 33–35. ISSN: 1098-4232. DOI: 10.1109/N-SSC.2006.4785860. URL: http://ieeexplore.ieee.org/document/4785860/.

[2] Laszlo B Kish. "End of Moore's law: thermal (noise) death of integration in micro and nano electronics". In: *Physics Letters A* 305.3-4 (Dec. 2002), pp. 144–149. ISSN: 0375-9601. DOI: 10.1016/S0375-9601(02)01365-8. URL: https://www.sciencedirect.com/science/article/pii/S0375960102013658.

[3] Krishna Palem and Avinash Lingamneni. "What to do about the end of Moore's law, probably!" In: *Proceedings of the 49th Annual Design Automation Conference on - DAC '12*. New York, New York, USA: ACM Press, 2012, p. 924. ISBN: 9781450311991. DOI: 10.1145/2228360.2228525. URL: http://dl.acm.org/citation.cfm?doid=2228360.2228525.

[4] Burn J. Lin. "Lithography till the end of Moore's law". In: *Proceedings of the 2012 ACM international symposium on International Symposium on Physical Design - ISPD '12*. New York, New York, USA: ACM Press, 2012, p. 1. ISBN: 9781450311670. DOI: 10.1145/2160916.2160918. URL: http://dl.acm.org/citation.cfm?doid=2160916.2160918.

[5] M. Mitchell Waldrop. "The chips are down for Moore's law". In: *Nature* 530.7589 (Feb. 2016), pp. 144–147. ISSN: 0028-0836. DOI: 10.1038/530144a. URL: http://www.nature.com/doifinder/10.1038/530144a.

[6] Robert Colwell. "The chip design game at the end of Moore's law". In: *2013 IEEE Hot Chips 25 Symposium (HCS)*. IEEE, Aug. 2013, pp. 1–16. ISBN: 978-1-4673-8881-8. DOI: 10.1109/HOTCHIPS.2013.7478302. URL: http://ieeexplore.ieee.org/document/7478302/.

[7] Thomas N. Theis and H.-S. Philip Wong. "The End of Moore's Law: A New Beginning for Information Technology". In: *Computing in Science & Engineering* 19.2 (Mar. 2017), pp. 41–50. ISSN: 1521-9615. DOI: 10.1109/MCSE.2017.29. URL: http://ieeexplore.ieee.org/document/7878935/.

[8] Eitan N. Shauly. "CMOS Leakage and Power Reduction in Transistors and Circuits: Process and Layout Considerations". In: *Journal of Low Power Electronics and Applications* 2.1 (Jan. 2012), pp. 1–29. ISSN: 2079-9268. DOI: 10.3390/jlpea2010001. URL: http://www.mdpi.com/2079-9268/2/1/1.

[9] Peter W. Shor. "Polynomial-Time Algorithms for Prime Factorization and Discrete Logarithms on a Quantum Computer". In: *SIAM Journal of Computing* 26 (Aug. 1997), pp. 1484–1509. DOI: 10.1137/S0097539795293172. arXiv: 9508027 [quant-ph]. URL: http://arxiv.org/abs/quant-ph/9508027%20http://dx.doi.org/10.1137/S0097539795293172.

[10] Yuri Ozhigov. "Quantum Computers Speed Up Classical with Probability Zero". In: *Chaos, Solitons & Fractals* 1 (Mar. 1999), pp. 1707–1714. arXiv: 9803064 [quant-ph]. URL: http://arxiv.org/abs/quant-ph/9803064.

[11] K. Jain and G. W. Pratt. "Optical transistor". In: *Applied Physics Letters* 28.12 (June 1976), pp. 719–721. ISSN: 0003-6951. DOI: 10.1063/1.88627. URL: http://aip.scitation.org/doi/10.1063/1.88627.

[12] Mehmet Fatih Yanik et al. "All-optical transistor action with bistable switching in a photonic crystal cross-waveguide geometry". In: *Optics Letters* 28.24 (Dec. 2003), p. 2506. ISSN: 0146-9592. DOI: 10.1364/OL.28.002506. URL: https://www.osapublishing.org/abstract.cfm?URI=ol-28-24-2506.

[13] J. Hwang et al. "A single-molecule optical transistor". In: *Nature* 460.7251 (July 2009), pp. 76–80. ISSN: 0028-0836. DOI: 10.1038/nature08134. URL: http://www.nature.com/articles/nature08134.

[14] Wenlan Chen et al. "All-optical switch and transistor gated by one stored photon." In: *Science (New York, N.Y.)* 341.6147 (Aug. 2013), pp. 768–70. ISSN: 1095-9203. DOI: 10.1126/science.1238169. URL: http://www.ncbi.nlm.nih.gov/pubmed/23828886.

[15] A. Barthelemy and L. Lefort. "All-optical transistor action by polarisation rotation during type-II phase-matched second harmonic generation". In: *Electronics Letters* 31.11 (May 1995), pp. 910–911. ISSN: 0013-5194. DOI: 10.1049/el:19950592. URL: http://digital-library.theiet.org/content/journals/10.1049/el%7B%5C_%7D19950592.

[16] M. N. Islam. "Ultrafast all-optical logic gates based on soliton trapping in fibers". In: *Optics Letters* 14.22 (Nov. 1989), p. 1257. ISSN: 0146-9592. DOI: 10.1364/OL.14.001257. URL: https://www.osapublishing.org/abstract.cfm?URI=ol-14-22-1257.

[17] A. Bogoni et al. “Regenerative and reconfigurable all-optical logic gates for ultra-fast applications”. In: *Electronics Letters* 41.7 (2005), p. 435. ISSN: 00135194. DOI: 10.1049/el:20058010. URL: http://digital-library.theiet.org/content/journals/10.1049/el%7B%5C_%7D20058010.

[18] Zhihong Li and Guifang Li. “Ultrahigh-speed reconfigurable logic gates based on four-wave mixing in a semiconductor optical amplifier”. In: *IEEE Photonics Technology Letters* 18.12 (June 2006), pp. 1341–1343. ISSN: 1041-1135. DOI: 10.1109/LPT.2006.877008. URL: http://ieeexplore.ieee.org/document/1638503/.

[19] R W Wood. “On a Remarkable Case of Uneven Distribution of Light in a Diffraction Grating Spectrum”. In: *Proceedings of the Physical Society of London* 18.1 (June 1902), pp. 269–275. ISSN: 1478-7814. DOI: 10.1088/1478-7814/18/1/325. URL: http://stacks.iop.org/1478-7814/18/i=1/a=325?key=crossref.7ebbe1383fb00dffe4b52e1569cdd953.

[20] Alexandra Boltasseva and Harry A Atwater. “Materials science. Low-loss plasmonic metamaterials.” In: *Science (New York, N.Y.)* 331.6015 (Jan. 2011), pp. 290–1. ISSN: 1095-9203. DOI: 10.1126/science.1198258. URL: http://www.ncbi.nlm.nih.gov/pubmed/21252335.

[21] F J Garcia-Vidal, L Martín-Moreno, and J B Pendry. “Surfaces with holes in them: new plasmonic metamaterials”. In: *Journal of Optics A: Pure and Applied Optics* 7.2 (Feb. 2005), S97–S101. ISSN: 1464-4258. DOI: 10.1088/1464-4258/7/2/013. URL: http://stacks.iop.org/1464-4258/7/i=2/a=013?key=crossref.ce1c4188525b68b6cfa7c840b91a5e34.

[22] Juergen Biener et al. “Nanoporous Plasmonic Metamaterials”. In: *Advanced Materials* 20.6 (Mar. 2008), pp. 1211–1217. ISSN: 09359648. DOI: 10.1002/adma.200701899. URL: http://doi.wiley.com/10.1002/adma.200701899.

[23] Yoav Avitzour, Yaroslav A. Urzhumov, and Gennady Shvets. “Wide-angle infrared absorber based on a negative-index plasmonic metamaterial”. In: *Physical Review B* 79.4 (Jan. 2009), p. 045131. ISSN: 1098-0121. DOI: 10.1103/PhysRevB.79.045131. URL: https://link.aps.org/doi/10.1103/PhysRevB.79.045131.

[24] Hyeon-Ho Jeong et al. “Dispersion and shape engineered plasmonic nanosensors”. In: *Nature Communications* 7 (Apr. 2016), p. 11331. ISSN: 2041-1723. DOI: 10.1038/ncomms11331. URL: http://www.nature.com/doifinder/10.1038/ncomms11331.

[25] Jagmeet Singh Sekhon and S. S. Verma. “Optimal Dimensions of Gold Nanorod for Plasmonic Nanosensors”. In: *Plasmonics* 6.1 (Mar. 2011), pp. 163–169. ISSN:

1557-1955. DOI: 10.1007/s11468-010-9182-3. URL: http://link.springer.com/10.1007/s11468-010-9182-3.

[26] Inhee Choi and Yeonho Choi. "Plasmonic Nanosensors: Review and Prospect". In: *IEEE Journal of Selected Topics in Quantum Electronics* 18.3 (May 2012), pp. 1110–1121. ISSN: 1077-260X. DOI: 10.1109/JSTQE.2011.2163386. URL: http://ieeexplore.ieee.org/document/5970075/.

[27] Ji Homola, Sinclair S. Yee, and Günter Gauglitz. "Surface plasmon resonance sensors: review". In: *Sensors and Actuators B: Chemical* 54.1-2 (Jan. 1999), pp. 3–15. ISSN: 09254005. DOI: 10.1016/S0925-4005(98)00321-9. URL: http://linkinghub.elsevier.com/retrieve/pii/S0925400598003219.

[28] William L. Barnes, Alain Dereux, and Thomas W. Ebbesen. "Surface plasmon subwavelength optics". In: *Nature* 424.6950 (Aug. 2003), pp. 824–830. ISSN: 0028-0836. DOI: 10.1038/nature01937. URL: http://www.nature.com/articles/nature01937.

[29] D. F.P. Pile and D. K. Gramotnev. "Plasmonic subwavelength waveguides: next to zero losses at sharp bends". In: *Optics Letters* 30.10 (May 2005), p. 1186. ISSN: 0146-9592. DOI: 10.1364/OL.30.001186. URL: https://www.osapublishing.org/abstract.cfm?URI=ol-30-10-1186.

[30] Georgios Veronis and Shanhui Fan. "Bends and splitters in metal-dielectric-metal subwavelength plasmonic waveguides". In: *Applied Physics Letters* 87.13 (Sept. 2005), p. 131102. ISSN: 0003-6951. DOI: 10.1063/1.2056594. URL: http://aip.scitation.org/doi/10.1063/1.2056594.

[31] Harry A. Atwater and Albert Polman. "Plasmonics for improved photovoltaic devices". In: *Nature Materials* 9.3 (Mar. 2010), pp. 205–213. ISSN: 1476-1122. DOI: 10.1038/nmat2629. URL: http://www.nature.com/articles/nmat2629.

[32] Alexandre Aubry et al. "Plasmonic Light-Harvesting Devices over the Whole Visible Spectrum". In: *Nano Letters* 10.7 (July 2010), pp. 2574–2579. ISSN: 1530-6984. DOI: 10.1021/nl101235d. URL: http://pubs.acs.org/doi/abs/10.1021/nl101235d.

[33] Peng Wang et al. "Plasmonic photocatalysts: harvesting visible light with noble metal nanoparticles". In: *Physical Chemistry Chemical Physics* 14.28 (June 2012), p. 9813. ISSN: 1463-9076. DOI: 10.1039/c2cp40823f. URL: http://xlink.rsc.org/?DOI=c2cp40823f.

[34] Qiuqun Liang et al. "Metamaterial-Based Two Dimensional Plasmonic Subwavelength Structures Offer the Broadest Waveband Light Harvesting". In: *Advanced Optical Materials* 1.1 (Jan. 2013), pp. 43–49. ISSN: 21951071. DOI:

10.1002/adom.201200009. URL: http://doi.wiley.com/10.1002/adom.201200009.

[35] Rounak A. Naphade et al. "Plasmonic light harvesting of dye sensitized solar cells by Au-nanoparticle loaded TiO ₂ nanofibers". In: *J. Mater. Chem. A* 2.4 (Dec. 2014), pp. 975–984. ISSN: 2050-7488. DOI: 10.1039/C3TA13246C. URL: http://xlink.rsc.org/?DOI=C3TA13246C.

[36] Mingzhu Long et al. "Ultrathin efficient perovskite solar cells employing a periodic structure of a composite hole conductor for elevated plasmonic light harvesting and hole collection". In: *Nanoscale* 8.12 (Mar. 2016), pp. 6290–6299. ISSN: 2040-3364. DOI: 10.1039/C5NR05042A. URL: http://xlink.rsc.org/?DOI=C5NR05042A.

[37] Koray Aydin et al. "Broadband polarization-independent resonant light absorption using ultrathin plasmonic super absorbers". In: *Nature Communications* 2.1 (Sept. 2011), p. 517. ISSN: 2041-1723. DOI: 10.1038/ncomms1528. URL: http://www.nature.com/articles/ncomms1528.

[38] Feng Wang et al. "Plasmonic Harvesting of Light Energy for Suzuki Coupling Reactions". In: *Journal of the American Chemical Society* 135.15 (Apr. 2013), pp. 5588–5601. ISSN: 0002-7863. DOI: 10.1021/ja310501y. URL: http://pubs.acs.org/doi/10.1021/ja310501y.

[39] Roxana Jijie et al. "Particle-based photodynamic therapy based on indocyanine green modified plasmonic nanostructures for inactivation of a Crohn's disease-associated Escherichia coli strain". In: *Journal of Materials Chemistry B* 4.15 (Apr. 2016), pp. 2598–2605. ISSN: 2050-750X. DOI: 10.1039/C5TB02697K. URL: http://xlink.rsc.org/?DOI=C5TB02697K.

[40] Onur Tokel et al. "Portable Microfluidic Integrated Plasmonic Platform for Pathogen Detection". In: *Scientific Reports* 5.1 (Aug. 2015), p. 9152. ISSN: 2045-2322. DOI: 10.1038/srep09152. URL: http://www.nature.com/articles/srep09152.

[41] Bo Zhang et al. "A plasmonic chip for biomarker discovery and diagnosis of type 1 diabetes". In: *Nature Medicine* 20.8 (Aug. 2014), pp. 948–953. ISSN: 1078-8956. DOI: 10.1038/nm.3619. URL: http://www.nature.com/articles/nm.3619.

[42] Xiaohua Huang et al. "Plasmonic photothermal therapy (PPTT) using gold nanoparticles". In: *Lasers in Medical Science* 23.3 (July 2008), pp. 217–228. ISSN: 0268-8921. DOI: 10.1007/s10103-007-0470-x. URL: http://link.springer.com/10.1007/s10103-007-0470-x.

[43] Andreas V. Kuhlmann et al. “Transform-limited single photons from a single quantum dot”. In: *Nature Communications* 6.1 (Dec. 2015), p. 8204. ISSN: 2041-1723. DOI: 10.1038/ncomms9204. URL: http://www.nature.com/articles/ncomms9204.

[44] Xing Ding et al. “On-Demand Single Photons with High Extraction Efficiency and Near-Unity Indistinguishability from a Resonantly Driven Quantum Dot in a Micropillar”. In: *Physical Review Letters* 116.2 (Jan. 2016), p. 020401. ISSN: 0031-9007. DOI: 10.1103/PhysRevLett.116.020401. URL: https://link.aps.org/doi/10.1103/PhysRevLett.116.020401.

[45] Dirk Heinze et al. “A quantum dot single-photon source with on-the-fly all-optical polarization control and timed emission”. In: *Nature Communications* 6.1 (Dec. 2015), p. 8473. ISSN: 2041-1723. DOI: 10.1038/ncomms9473. URL: http://www.nature.com/articles/ncomms9473.

[46] M. Müller et al. “On-demand generation of indistinguishable polarization-entangled photon pairs”. In: *Nature Photonics* 8.3 (Mar. 2014), pp. 224–228. ISSN: 1749-4885. DOI: 10.1038/nphoton.2013.377. URL: http://www.nature.com/articles/nphoton.2013.377.

[47] Charles Santori et al. “Triggered Single Photons from a Quantum Dot”. In: *Physical Review Letters* 86.8 (Feb. 2001), pp. 1502–1505. ISSN: 0031-9007. DOI: 10.1103/PhysRevLett.86.1502. URL: https://link.aps.org/doi/10.1103/PhysRevLett.86.1502.

[48] Yanwen Wu et al. “Population Inversion in a Single InGaAs Quantum Dot Using the Method of Adiabatic Rapid Passage”. In: *Physical Review Letters* 106.6 (Feb. 2011), p. 067401. ISSN: 0031-9007. DOI: 10.1103/PhysRevLett.106.067401. URL: https://link.aps.org/doi/10.1103/PhysRevLett.106.067401.

[49] Xiaodong Xu et al. “Fast Spin State Initialization in a Singly Charged InAs-GaAs Quantum Dot by Optical Cooling”. In: *Physical Review Letters* 99.9 (Aug. 2007), p. 097401. ISSN: 0031-9007. DOI: 10.1103/PhysRevLett.99.097401. URL: https://link.aps.org/doi/10.1103/PhysRevLett.99.097401.

[50] Yanwen Wu et al. “Density Matrix Tomography through Sequential Coherent Optical Rotations of an Exciton Qubit in a Single Quantum Dot”. In: *Physical Review Letters* 96.8 (Feb. 2006), p. 087402. ISSN: 0031-9007. DOI: 10.1103/PhysRevLett.96.087402. URL: https://link.aps.org/doi/10.1103/PhysRevLett.96.087402.

[51] Yanwen Wu et al. “Selective Optical Control of Electron Spin Coherence in Singly Charged GaAs Al 0.3 Ga 0.7 As Quantum Dots”. In: *Physical Re-*

view Letters 99.9 (Aug. 2007), p. 097402. ISSN: 0031-9007. DOI: 10.1103/PhysRevLett.99.097402. URL: https://link.aps.org/doi/10.1103/PhysRevLett.99.097402.

[52] Sophia E. Economou et al. "Proposal for optical U(1) rotations of electron spin trapped in a quantum dot". In: *Physical Review B* 74.20 (Nov. 2006), p. 205415. ISSN: 1098-0121. DOI: 10.1103/PhysRevB.74.205415. URL: https://link.aps.org/doi/10.1103/PhysRevB.74.205415.

[53] Xiaoqin Li et al. "An all-optical quantum gate in a semiconductor quantum dot." In: *Science (New York, N.Y.)* 301.5634 (Aug. 2003), pp. 809–11. ISSN: 1095-9203. DOI: 10.1126/science.1083800. URL: http://www.ncbi.nlm.nih.gov/pubmed/12907794.

[54] Danny Kim et al. "Ultrafast optical control of entanglement between two quantum-dot spins". In: *Nature Physics* 7.3 (Mar. 2011), pp. 223–229. ISSN: 1745-2473. DOI: 10.1038/nphys1863. URL: http://www.nature.com/articles/nphys1863.

[55] M. V. Gurudev Dutt et al. "Ultrafast optical control of electron spin coherence in charged GaAs quantum dots". In: *Physical Review B* 74.12 (Sept. 2006), p. 125306. ISSN: 1098-0121. DOI: 10.1103/PhysRevB.74.125306. URL: https://link.aps.org/doi/10.1103/PhysRevB.74.125306.

[56] Susan J. Angus et al. "Gate-Defined Quantum Dots in Intrinsic Silicon". In: *Nano Lett.* 7 (2007), pp. 2051–2055. DOI: 10.1021/NL070949K. URL: https://pubs.acs.org/doi/abs/10.1021/nl070949k.

[57] M. J. Biercuk et al. "Gate-Defined Quantum Dots on Carbon Nanotubes". In: *Nano Lett.* 5 (2005), pp. 1267–1271. DOI: 10.1021/NL050364V. URL: https://pubs.acs.org/doi/abs/10.1021/nl050364v.

[58] A. Pfund et al. "Top-gate defined double quantum dots in InAs nanowires". In: *Applied Physics Letters* 89.25 (Dec. 2006), p. 252106. ISSN: 0003-6951. DOI: 10.1063/1.2409625. URL: http://aip.scitation.org/doi/10.1063/1.2409625.

[59] Gleb M. Akselrod et al. "Probing the mechanisms of large Purcell enhancement in plasmonic nanoantennas". In: *Nature Photonics* 8.11 (Nov. 2014), pp. 835–840. ISSN: 1749-4885. DOI: 10.1038/nphoton.2014.228. URL: http://www.nature.com/articles/nphoton.2014.228.

[60] Koichi Okamoto, Saurabh Vyawahare, and Axel Scherer. "Surface-plasmon enhanced bright emission from CdSe quantum-dot nanocrystals". In: *Journal of the Optical Society of America B* 23.8 (Aug. 2006), p. 1674. ISSN: 0740-3224.

DOI: 10.1364/JOSAB.23.001674. URL: https://www.osapublishing.org/abstract.cfm?URI=josab-23-8-1674.

[61] K. Tanaka et al. "Multifold Enhancement of Quantum Dot Luminescence in Plasmonic Metamaterials". In: *Physical Review Letters* 105.22 (Nov. 2010), p. 227403. DOI: 10.1103/PhysRevLett.105.227403. URL: https://link.aps.org/doi/10.1103/PhysRevLett.105.227403.

[62] Kosuke Sugawa et al. "Metal-Enhanced Fluorescence Platforms Based on Plasmonic Ordered Copper Arrays: Wavelength Dependence of Quenching and Enhancement Effects". In: *ACS Nano* 7.11 (Nov. 2013), pp. 9997–10010. ISSN: 1936-0851. DOI: 10.1021/nn403925d. URL: http://pubs.acs.org/doi/10.1021/nn403925d.

[63] M. Haridas, L. N. Tripathi, and J. K. Basu. "Photoluminescence enhancement and quenching in metal-semiconductor quantum dot hybrid arrays". In: *Applied Physics Letters* 98.6 (Feb. 2011), p. 063305. ISSN: 0003-6951. DOI: 10.1063/1.3553766. URL: http://aip.scitation.org/doi/10.1063/1.3553766.

[64] Xianxiang Zeng et al. "Using Graphene-Based Plasmonic Nanocomposites to Quench Energy from Quantum Dots for Signal-On Photoelectrochemical Aptasensing". In: *Analytical Chemistry* 85.24 (Dec. 2013), pp. 11720–11724. ISSN: 0003-2700. DOI: 10.1021/ac403408y. URL: http://pubs.acs.org/doi/10.1021/ac403408y.

[65] Alberto G Curto et al. "Unidirectional emission of a quantum dot coupled to a nanoantenna." In: *Science (New York, N.Y.)* 329.5994 (Aug. 2010), pp. 930–3. ISSN: 1095-9203. DOI: 10.1126/science.1191922. URL: http://www.ncbi.nlm.nih.gov/pubmed/20724630.

[66] Terukazu Kosako, Yutaka Kadoya, and Holger F. Hofmann. "Directional control of light by a nano-optical YagiUda antenna". In: *Nature Photonics* 4.5 (May 2010), pp. 312–315. ISSN: 1749-4885. DOI: 10.1038/nphoton.2010.34. URL: http://www.nature.com/articles/nphoton.2010.34.

[67] Heykel Aouani et al. "Plasmonic Antennas for Directional Sorting of Fluorescence Emission". In: *Nano Letters* 11.6 (June 2011), pp. 2400–2406. ISSN: 1530-6984. DOI: 10.1021/nl200772d. URL: http://pubs.acs.org/doi/abs/10.1021/nl200772d.

[68] R. Ruppin. "Surface polaritons of a left-handed medium". In: *Physics Letters A* 277.1 (Nov. 2000), pp. 61–64. ISSN: 0375-9601. DOI: 10.1016/S0375-9601(00)00694-0. URL: https://www.sciencedirect.com/science/article/pii/S0375960100006940.

[69] Benjamin Reinhard et al. "Experimental and numerical studies of terahertz surface waves on a thin metamaterial film". In: *Optics Letters* 35.9 (May 2010), p. 1320. ISSN: 0146-9592. DOI: 10.1364/OL.35.001320. URL: https://www.osapublishing.org/abstract.cfm?URI=ol-35-9-1320.

[70] Zhijun Sun et al. "Artificial TE-mode surface waves at metal surfaces mimicking surface plasmons". In: *Optics Express* 22.4 (Feb. 2014), p. 4714. ISSN: 1094-4087. DOI: 10.1364/OE.22.004714. URL: https://www.osapublishing.org/oe/abstract.cfm?uri=oe-22-4-4714.

[71] Stefan Maier. "Surface Plasmon Polaritons at Metal / Insulator Interfaces". In: *Plasmonics: Fundamentals and Applications*. Boston, MA: Springer US, 2007. Chap. 2, pp. 21–37. DOI: 10.1007/0-387-37825-1_2. URL: http://link.springer.com/10.1007/0-387-37825-1%7B%5C_%7D2.

[72] Pavel A. Frantsuzov and R. A. Marcus. "Explanation of quantum dot blinking without the long-lived trap hypothesis". In: *Physical Review B* 72.15 (Oct. 2005), p. 155321. ISSN: 1098-0121. DOI: 10.1103/PhysRevB.72.155321. URL: https://link.aps.org/doi/10.1103/PhysRevB.72.155321.

[73] Andrew M Smith and Shuming Nie. "Next-generation quantum dots." In: *Nature biotechnology* 27.8 (Aug. 2009), pp. 732–3. ISSN: 1546-1696. DOI: 10.1038/nbt0809-732. URL: http://www.ncbi.nlm.nih.gov/pubmed/19668181%20http://www.pubmedcentral.nih.gov/articlerender.fcgi?artid=PMC2854554.

[74] Sadao Adachi. "Structural Properties". In: *Physical Properties of III-V Semiconductor Compounds*. Weinheim, FRG: Wiley-VCH Verlag GmbH & Co. KGaA, Jan. 2005, pp. 4–16. DOI: 10.1002/352760281X.ch2. URL: http://doi.wiley.com/10.1002/352760281X.ch2.

[75] Mads Lykke Andersen et al. "Strongly modified plasmonmatter interaction with mesoscopic quantum emitters". In: *Nature Physics* 7.3 (Mar. 2011), pp. 215–218. ISSN: 1745-2473. DOI: 10.1038/nphys1870. URL: http://www.nature.com/articles/nphys1870.

[76] A. González-Tudela et al. "Theory of Strong Coupling between Quantum Emitters and Propagating Surface Plasmons". In: *Physical Review Letters* 110.12 (Mar. 2013), p. 126801. ISSN: 0031-9007. DOI: 10.1103/PhysRevLett.110.126801. URL: http://link.aps.org/doi/10.1103/PhysRevLett.110.126801.

[77] J Tommila et al. "Size-dependent properties of single InAs quantum dots grown in nanoimprint lithography patterned GaAs pits". In: *Nanotechnology* 24.23 (June 2013), p. 235204. ISSN: 0957-4484. DOI: 10.1088/0957-4484/24/23/

235204. URL: http://stacks.iop.org/0957-4484/24/i=23/a=235204?key=crossref.362dd0e04adc48e1103198966a0e73d5.